

UCSF

UC San Francisco Electronic Theses and Dissertations

Title

Regulation of Flagellar Length by Intraflagellar Transport

Permalink

<https://escholarship.org/uc/item/4929p0qd>

Author

Engel, Benjamin David

Publication Date

2011

Peer reviewed|Thesis/dissertation

Regulation of Flagellar Length by Intraflagellar Transport

by

Benjamin D. Engel

DISSERTATION

Submitted in partial satisfaction of the requirements for the degree of

DOCTOR OF PHILOSOPHY

in

Cell Biology

in the

GRADUATE DIVISION

of the

for Mom, Dad, Jesse, and Karin

*Special thanks to my mentors Wallace Marshall, Orion Weiner,
Bruce Alberts, Kurt Thorn, Ritsu Kamiya, and Carolyn Larabell.*

*In distinct fashions, you have each imprinted upon me a love for science,
and for that I will always be grateful.*

Abstract

Eukaryotic flagella (also referred to as cilia) are microtubule-based organelles that protrude from the cell body into the extracellular environment. In addition to powering cell motility and fluid flow, flagella mediate the reception of numerous signaling processes that direct developmental programs. Because flagella serve such diverse roles, defects in flagellar morphology produce a pleiotropic array of human diseases.

The assembly and maintenance of flagella relies on intraflagellar transport (IFT), the molecular motor driven traffic of large protein complexes (called trains) carrying flagellar proteins between the cell body and the flagellar tip. To better understand the relationship between flagellar length and IFT, we developed a method to quantify IFT in the flagella of *Chlamydomonas reinhardtii* using total internal reflection fluorescence microscopy (TIRF, described in detail in chapter 2). In chapter 1, we measured changes in anterograde (base to tip) IFT during flagellar regeneration and found that IFT train size is inversely proportional to flagellar length, and may thus determine the steady state length of flagella. In chapter 3, we performed a pharmacological screen for impaired cell motility in *Chlamydomonas* and identified a small molecule that reduces flagellar length in several organisms, while affecting both IFT and actin dynamics. In chapter 4, we performed a genetic screen for impaired *Chlamydomonas* cell motility and isolated a temperature-sensitive mutant in the heavy chain of IFT dynein, the retrograde motor that returns IFT trains from the flagellar tip to the cell body. Unlike mutations in the anterograde kinesin motor, which impede both flagellar

assembly and maintenance, the dynein mutant (named *dhc1b-3*) experiences defects in assembly but not maintenance despite significant reductions in both dynein protein and IFT activity. This surprising observation has forced us to rethink the relationship between IFT and the control of flagellar length.

Table of Contents

Abstract	iv
List of Tables	vii
List of Figures	viii
Forward	1
Perspectives on Flagellar Length Control	
Chapter 1	5
Intraflagellar Transport Particle Size Scales Inversely with Flagellar Length: Revisiting the Balance-Point Length Control Model	
Chapter 2	44
Total Internal Reflection Fluorescence (TIRF) Microscopy of <i>Chlamydomonas</i> Flagella	
Chapter 3	82
A Cell-based Screen for Inhibitors of Flagella-driven Motility in <i>Chlamydomonas</i> Reveals a Novel Modulator of Ciliary Length and Retrograde Actin Flow	
Chapter 4	138
Dissecting the Roles of Retrograde Intraflagellar Transport in Flagellar Assembly and Maintenance	
Appendix	190
Contributions to “The Intraflagellar Transport Particle Sub-complex 25/27 Regulates IFT Particle Stability and Composition”	

List of Tables

Table 3.1	115
Dose response for candidate compounds	
Table 3.2	116
Swimming speed versus concentration of compounds E and F	
Table 4.1	164
Proteins identified by 2D-DIGE, clustered by accumulation profile (accompanies Figure 4.8)	
Table 4.S1	176
Primers used for quantitative PCR	
Table 4.S2	177
Primers used for sequencing Dhc1b cDNA, including UTRs	

List of Figures

Figure1.1	37
During flagellar regeneration, there is an inverse relationship between IFT train size and flagellar length	
Figure1.2	38
Quantitative photobleaching confirms that IFT trains in short flagella contain more KAP protein	
Figure1.3	39
During long-zero regeneration, there is a linear correlation between IFT train size and flagellar length	
Figure1.4	40
The original and revised balance-point models of flagellar length control, and possible mechanisms of IFT train size modulation	
Figure1.S1	41
Imaging and photobleaching controls	
Figure1.S2	42
Speed, frequency, and intensity correlations from the live-cell pH shock experiment (Figure 1.1)	
Figure1.S3	43
Complete raw and normalized data sets from the long-zero experiment (Figure 1.3), corrected for camera noise	

Figure2.1	80
Chlamy TIRF imaging setup and the effect of axoneme geometry on GFP fluorescence	
Figure2.2	80
Comparison of DIC, spinning disk confocal, and TIRF microscopy and summary of current IFT observations via TIRF	
Figure2.3	81
Protein abundance in the flagella of wild-type and GFP-tagged strains	
Figure2.4	81
Simultaneous two-color TIRF of IFT20-mCherry and BBS4-GFP	
Figure3.1	131
Screen characterization and results	
Figure3.2	132
Structures of candidate compounds obtained in the initial screen and validated in secondary assays	
Figure3.3	133
Effects of ciliabrevin (compound B) on <i>Chlamydomonas</i> flagellar length and intraflagellar transport	
Figure3.4	134
Effect of ciliabrevin (compound B) on mammalian cell ciliary length	
Figure3.5	135
Effects of ciliabrevin (compound B) on tubulin dynamics in <i>Drosophila</i> S2 cells	

Figure3.6	136
	Effects of ciliabrevin (compound B) on actin dynamics in <i>Drosophila</i> S2 cells	
Figure3.S1	137
	Effects of known actin-inhibiting drugs on actin dynamics in <i>Drosophila</i> S2 cells	
Figure4.1	180
	Genetic screening strategy and temperature-sensitive “retrograde IFT” phenotype of isolated mutant strain	
Figure4.2	181
	mRNA and flagellar protein accumulation and depletion in the <i>ts</i> -flagellar assembly mutant	
Figure4.3	182
	Linkage mapping of <i>ts</i> -flagellar assembly mutant and sequencing of a single base-pair mutation in Dhc1b	
Figure4.4	183
	Kinetics of <i>dhc1b-3</i> flagellar loss in vegetative cells, synchronized dividing cells, during gametogenesis and in <i>fla10/dhc1b-3</i> double mutants	
Figure4.5	184
	Kinetics of flagellar regeneration following pH shock in wild-type and <i>dhc1b-3</i> at 21C and 34C	
Figure4.6	185
	Intraflagellar transport in wild-type and <i>dhc1b-3</i> at 21C and 34C	

Figure4.7	186
Phototaxis, swimming speed, and flagellar beat frequency in wild-type and <i>dhc1b-3</i> at 21C and 34C.	
Figure4.8	187
2D-DIGE proteomic analysis of flagellar protein accumulation and depletion in wild-type 21C vs. mutant 21C vs. mutant 34C (accompanies Table 4.1)	
Figure4.S1	188
Accumulation of IFT and axonemal proteins in <i>dhc1b-3</i> cell bodies	
Figure4.S2	188
PCR scheme for rapid verification of <i>dhc1b-3</i> point mutation	
Figure4.S3	189
Kinetics of flagellar regeneration in <i>dhc1b-3</i> at 21C following increasing pre-incubation times at 34C	
FigureA.8	197
Two classes of IFT particles enter flagella and undergo bi-directional IFT	
FigureA.9	198
Hypothetical model of 25/27-regulated IFT particle assembly in <i>C. reinhardtii</i> .	

Forward

Perspectives on Flagellar Length Control

The structure and function of flagella will be outlined in great detail in the introductions of the following chapters. Rather than retread the same information yet again, I would like to instead provide a slightly broader context for the studies undertaken in this thesis.

One consistent theme throughout this thesis is that we evaluated changes in flagellar length using the balance-point model (Figure 1.1 C), which asserts that flagellar length is the sum of the assembly rate and disassembly rate at the flagellar tip, the only site where tubulin is added or removed from the axoneme (Marshall et al., 2001, 2005). The balance-point model further asserts that at least the assembly rate is dependent upon intraflagellar transport (IFT) to carry axonemal precursors such as tubulin from the cell body to the flagellar tip, a hypothesis that is supported by the disassembly of flagella that occurs when IFT is switched off using *Chlamydomonas* mutant strains (Kozminski et al., 1995).

The chapters in this thesis are presented in the chronological order in which the work was performed. The initial question we addressed in chapter 1 was whether changes in IFT during flagellar regeneration could explain the decelerating flagellar growth rate to a steady-state length, as proof of concept for the balance-point model. In order to accurately quantify IFT in live cells, we measured GFP-tagged IFT proteins in *Chlamydomonas* flagella by total internal reflection fluorescence (TIRF) microscopy. This method is thoroughly detailed in chapter 2. In chapters 3 and 4, we performed screens for chemical and genetic

modulators of flagellar length, respectively. In both of these studies, we measured changes in IFT using the TIRF technique and attempted to correlate these changes with flagellar length, in keeping with the balance-point model. Thus, while the studies in this thesis may differ in their approaches, they present a unified vision of flagellar length control as a simple readout of protein transport between the cell body and the flagellar tip. However, as we observed in chapter 4, the regulation of flagellar length may be more convoluted than this elegant solution.

It is important to put our IFT observations into context with several other biological processes that affect flagellar length. In addition to IFT-mediated assembly, the rate of flagellar disassembly is also likely subject to regulation, as microtubule stabilizing (EB1; Pedersen et al., 2003; Schroder et al., 2007) and destabilizing (kinesin-13; Blaineau et al., 2007; Piao et al., 2009) proteins are both localized to the flagellar tip. Several kinases in the flagellum have been shown alter flagellar length (Wilson and Lefebvre, 2004; Berman et al., 2003; Bradley and Quarmby, 2005), perhaps through a yet to be elucidated “length sensor” mechanism. There are modifications in the protein composition of the proximal and distal halves of the flagellum (Piperno and Ramanis, 1991; Yagi et al., 2009), differences that could serve as a ruler for flagellar length.

Furthermore, the proximal half of the flagellum appears to be more resistant than the distal half to microtubule destabilization (Dentler and Adams, 1992). Flagella also change their length in response to fluctuations in calcium and cyclic AMP levels and physical stimulation by fluid flow, in a process known as flow-mediated

adaptation (Besschetnova, 2010). In addition to sensing and signaling within the flagellum, flagellar assembly is also subject to intracellular trafficking of vesicles and proteins from the golgi to the flagellar base (Follit et al., 2006; Nachury et al., 2007; Yoshimura et al., 2007) and gating the entry of these proteins into the flagellum at the transition zone (Craig et al., 2010). Finally, the expression of many flagellar genes is under the direct control of master regulator gene *Foxj1*, the downregulation of which induces flagella to shorten (Neugebauer et al., 2009; Cruz et al., 2010).

The relationship between IFT and flagellar length described by the balance-point model is but one piece of the puzzle. Perhaps it serves as a basal mechanism that is always in place, but may be modulated by additional layers of signaling, intracellular trafficking, and transcriptional control. Understanding the interplay between these different processes will be the key to building an integrated model of flagellar length control.

References

- Berman, S. A., N. F. Wilson, N. A. Haas, and P. A. Lefebvre. 2003. A novel MAP kinase regulates flagellar length in *Chlamydomonas*. *Curr. Biol.* 13:1145-1149.
- Besschetnova TY, Kolpakova-Hart E, Guan Y, Zhou J, Olsen BR, Shah JV. 2010. Identification of signaling pathways regulating primary cilium length and flow-mediated adaptation. *Curr. Biol.* 20, 182-187.
- Bradley, B. A. and L. M. Quarmby. 2005. A NIMA-related kinase, *Cnk2p*, regulates both flagellar length and cell size in *Chlamydomonas*. *J. Cell Sci.* 118:3317-3326.
- Blaineau C, Tessier M, Dubessay P, Tasse L, Crobu L, Pagès M, Bastien P. 2007. A novel microtubule-depolymerizing kinesin involved in length control of a eukaryotic flagellum. *Curr. Biol.* 17:778-782.
- Craig, B, Tsao, C.C., Diener, D.R., Hou, Y., Lechtreck, K.F., Rosenbaum, J.L., and Witman, G.B. 2010. CEP290 tethers flagellar transition zone microtubules to the membrane and regulates flagellar protein content. *J. Cell Biol.* 190:927-40.

- Cruz C, Ribes V, Kutejova E, Cayuso J, Lawson V, Norris D, Stevens J, Davey M, Blight K, Bangs F, Mynett A, Hirst E, Chung R, Balaskas N, Brody SL, Marti E, Briscoe J. 2010. Foxj1 regulates floor plate cilia architecture and modifies the response of cells to sonic hedgehog signalling. *Development*. 137:4271-4282.
- Dentler WL, Adams C. 1992. Flagellar microtubule dynamics in *Chlamydomonas*: cytochalasin D induces periods of microtubule shortening and elongation; and colchicine induces disassembly of the distal, but not proximal, half of the flagellum. *J. Cell Biol.* 117, 1289-1298.
- Follit, J. A., Tuft, R. A., Fogarty, K. E., and Pazour, G. J. 2006. The intraflagellar transport protein IFT20 is associated with the Golgi complex and is required for cilia assembly. *Mol. Biol. Cell.* 17:3781-3792.
- Kozminski, K. G., P. L. Beech, and J. L. Rosenbaum. 1995. The *Chlamydomonas* kinesin-like protein FLA10 is involved in motility associated with the flagellar membrane. *J. Cell Biol.* 131:1517-1527.
- Marshall, W. F. and J. L. Rosenbaum. 2001. Intraflagellar transport balances continuous turnover of outer doublet microtubules: implications for flagellar length control. *J. Cell Biol.* 155:405-414.
- Marshall, W. F., H. Qin, M. Rodrigo Brenni, and J. L. Rosenbaum. 2005. Flagellar length control system: testing a simple model based on intraflagellar transport and turnover. *Mol. Biol. Cell.* 16:270-278.
- Nachury, M. V., Loktev, A. V., Zhang, Q., Westlake, C. J., Peränen, J., Merdes, A., Slusarski, D. C., Scheller, R. H., Bazan, J. F., Sheffield, V. C., et al. 2007. A core complex of BBS proteins cooperates with the GTPase Rab8 to promote ciliary membrane biogenesis. *Cell.* 129:1201-1213.
- Neugebauer JM, Amack JD, Peterson AG, Bisgrove BW, Yost HJ. 2009. FGF signalling during embryo development regulates cilia length in diverse epithelia. *Nature*. 458:651-654.
- Pedersen, L.B., Geimer, S., Sloboda, R. D., and J. L. Rosenbaum. 2003. The Microtubule plus end-tracking protein EB1 is localized to the flagellar tip and basal bodies in *Chlamydomonas reinhardtii*. *Curr. Biol.* 13:1969-1974.
- Piao T, Luo M, Wang L, Guo Y, Li D, Li P, Snell WJ, Pan J. 2009. A microtubule depolymerizing kinesin functions during both flagellar disassembly and flagellar assembly in *Chlamydomonas*. *Proc. Natl. Acad. Sci. USA*. 106:4713-4718.
- Piperno G, Ramanis Z. 1991. The proximal portion of *Chlamydomonas* flagella contains a distinct set of inner dynein arms. *J. Cell Biol.* 112, 701-9.
- Schrøder JM, Schneider L, Christensen ST, Pedersen LB. 2007. EB1 is required for primary cilia assembly in fibroblasts. *Curr. Biol.* 13:1134-1139.
- Wilson, N. F. and P. A. Lefebvre. 2004. Regulation of flagellar assembly by glycogen synthase kinase 3 in *Chlamydomonas reinhardtii*. *Eukaryot. Cell.* 3:1307-1319.
- Yagi T, Uematsu K, Liu Z, Kamiya R. 2009. Identification of dyneins that localize exclusively to the proximal portion of *Chlamydomonas* flagella. *J. Cell Sci.* 122, 1306-1314.
- Yoshimura, S., Egerer, J., Fuchs, E., Haas, A. K., and Barr, F. A. 2007. Functional dissection of Rab GTPases involved in primary cilium formation. *J. Cell Biol.* 178:363-369.

Chapter 1

Intraflagellar Transport Particle Size Scales Inversely with Flagellar Length: Revisiting the Balance-Point Length Control Model

Benjamin D. Engel¹, William B. Ludington¹, & Wallace F. Marshall¹

1. Dept. of Biochemistry & Biophysics, UCSF

Originally published in *The Journal of Cell Biology*, 187: 81-89, October 2009.

Abstract

The assembly and maintenance of eukaryotic flagella is regulated by intraflagellar transport (IFT), the bidirectional traffic of IFT particles (recently renamed IFT trains) within the flagellum. We previously proposed the balance-point length control model, which predicted that the frequency of train transport should decrease as a function of flagellar length, thus modulating the length-dependent flagellar assembly rate. However, this model was challenged by the differential interference contrast (DIC) microscopy observation that IFT frequency is length-independent. Using total internal reflection fluorescence (TIRF) microscopy to quantify protein traffic during the regeneration of *Chlamydomonas reinhardtii* flagella, we determined that anterograde IFT trains in short flagella are composed of more KAP (kinesin-associated protein) and IFT27 proteins than trains in long flagella. This length-dependent remodeling of train size is consistent with the kinetics of flagellar regeneration and supports a revised balance-point model of flagellar length control, where the size of anterograde IFT trains tunes the rate of flagellar assembly.

Introduction

How cells regulate organelle size is a fundamental question in cell biology. The eukaryotic flagellum (a term used interchangeably with cilium), with its easily measured linear geometry, provides an ideal model for studying organelle size control. Furthermore, ciliary length control has become increasingly medically

relevant, with recent studies linking ciliary defects to a wide range of human disorders (Pazour and Rosenbaum, 2002; Bisgrove and Yost, 2006).

The unicellular biflagellate green alga *Chlamydomonas reinhardtii* is a powerful tool for studying flagellar biology (Randall, 1969; Silflow and Lefebvre, 2001). Following abscission, flagella regenerate to their original length with reproducible kinetics (Fig. 1A). Short flagella undergo a period of rapid growth, then transition to a slow elongation phase as they near their steady-state length (Fig. 1B). Though this phenomenon was first observed forty years ago (Rosenbaum et al., 1969), the mechanisms that control the kinetics of flagellar regeneration are not well understood. Studies in *Chlamydomonas* have revealed that the assembly and maintenance of flagella depend on intraflagellar transport (IFT), the molecular motor-driven process of bidirectional protein traffic within the flagellum (Kozminski et al., 1993). IFT describes the movement of IFT trains (previously referred to as “particles” but renamed “trains” based on electron-tomography; Pigino et al., 2009), heterogeneous linear protein arrays composed of heterotrimeric kinesin-2, cytoplasmic dynein-1b, axonemal cargo, and two varieties of IFT complexes (A and B) (Piperno and Mead, 1997; Cole et al., 1998; Cole, 2003; Ou et al., 2007). Kinesin powers anterograde transport to the distal tip of the flagellum, where the trains are remodeled and subsequently undergo dynein-driven retrograde return to the base. IFT has been shown to be directly responsible for the transport of axonemal precursors to the site of flagellar assembly at the tip (Qin et al., 2004; Hou et al., 2007). Defects in kinesin, dynein, and most of the IFT proteins all lead to short or absent flagella (Huang et

al., 1977; Pazour et al., 1999, 2000; Porter et al., 1999; Piperno et al., 1998; Deane et al., 2001; Pedersen et al., 2005). Additionally, reducing the speed and frequency of IFT leads to flagellar shortening (Kozminski et al., 1995; Iomini et al., 2001). Thus, IFT appears to play a central role in mediating flagellar length.

The balance-point model of flagellar length control (Fig. 1C) (Marshall et al., 2001, 2005) proposes that flagellar length is the resultant of two opposing rates: a length-independent disassembly rate and an assembly rate that decreases as the flagellum elongates. The length-independent disassembly rate is supported by the observation that when IFT is stopped in the *fla10* conditional kinesin-2 mutant, disassembly occurs at a constant basal rate regardless of flagellar length (Kozminski et al., 1995; Parker and Quarmby, 2003; Marshall et al., 2001, 2005). Furthermore, during drug or mitosis-induced active flagellar disassembly, a process that requires retrograde IFT, flagella also shorten at a length-independent rate (Pan and Snell, 2005; Marshall et al., 2005). The balance-point model predicts that the flagellar assembly rate decreases as a function of length until the flagellum reaches a unique steady-state length where the assembly and disassembly rates are in equilibrium. Driven by the observation that short and long flagella contain roughly the same quantity of IFT protein (Marshall et al., 2005), the original balance-point model proposed that the number of IFT trains in a flagellum is constant. Thus, the length-dependent assembly rate would arise from the variable frequency of anterograde trafficking events. As the flagellum lengthens, trains would become spaced further apart,

new cargo would arrive at the tip less frequently, and the assembly rate would decrease (Fig. 4A).

However, studies using DIC microscopy revealed that long flagella actually contain more IFT trains than short flagella (Dentler, 2005). This observation appears to invalidate a key prediction of the balance-point model, and seems to be inconsistent with the finding that all flagella contain the same amount of IFT protein. However, this conflict is based on the assumption that all trains are equivalently sized. In fact, IFT trains have been demonstrated to be modular. When viewed by transmission electron microscopy, trains range from 100nm to over 600nm in length (Pedersen et al., 2006), and are composed of a variable number of smaller, linearly-arranged particle substructures (Kozminski et al., 1993, 1995; Pigino et al., 2009). Furthermore, immunogold localization studies suggest that the number of IFT proteins in a train can vary by several-fold (Sloboda and Howard, 2007). Thus, changes in IFT train size, rather than frequency, could theoretically mediate the length-dependent assembly rate predicted by the balance-point model.

Results and Discussion

To test the predictions of the revised balance-point model, we needed an accurate method to assay IFT train size in live cells undergoing flagellar regeneration. Previous attempts to visualize IFT in *Chlamydomonas* have primarily relied on DIC microscopy. While this technique can measure the speed and frequency of IFT (Kozminski et al., 1993; Iomini et al., 2001; Dentler, 2005),

it is insufficient for quantifying train size. The apparent size of trains seen by DIC is not a good measure of protein content, as it is affected by the angle of DIC shear and the train's refractive index. We decided instead to use fluorescence microscopy to quantify the amount of GFP-labeled IFT protein found in each train. GFP tagging of IFT proteins has been extensively employed in *C. elegans* (Orozco et al., 1999; Ou et al., 2007), but *Chlamydomonas* provides a significant advantage for visualizing IFT. Because wildtype *Chlamydomonas* cells adhere both their flagella to the coverglass (Bloodgood, 1995), we were able to achieve high fidelity measurements with adjusted TIRF (Axelrod, 2001; Mattheyses and Axelrod, 2006), where the angle of incident light is decreased to close to the critical angle, providing a deeper field of illumination near the coverglass (250-350nm, see materials and methods). Using this setup (Fig. 1D), we imaged completely through adhered flagella (Fig. S1A) at ~30 frames per second, while the autofluorescent cell bodies remained outside the field of illumination.

We analyzed two key members of anterograde trains: KAP (Mueller et al., 2005), the nonmotor subunit of kinesin-2, and IFT27 (Qin et al., 2007), a small rab-like GTPase that is a core component of IFT complex B. IFT complex B is required for anterograde transport and is thought to be present in every anterograde train. By making kymographs from movies of KAP-GFP and IFT27-GFP strains (Figs. 1E and 1F, Videos 1 and 2), we extracted information about the speed, frequency, and GFP intensity of IFT trains (for methods see Fig. S1B). We restricted our analysis to anterograde IFT because it is these trains that contribute to the length-dependent rate of axoneme assembly. Retrograde IFT

may contribute to disassembly, but it appears to do so in a length-independent manner (Pan and Snell, 2005), which cannot explain the kinetics of flagellar regeneration and the steady-state length.

To observe how IFT is affected by flagellar regeneration, we exposed cells to an acidic pH shock, which induces flagellar abscission (Lefebvre, 1995). During the subsequent regeneration phase, we measured the speed, frequency, and GFP intensity of anterograde transport and correlated these measurements with flagellar length. Consistent with previous observations (Dentler, 2005), we found that anterograde IFT frequency is relatively length-independent and varies between ~ 1 train/s in short flagella to ~ 1.25 trains/s in long flagella (Fig. 1G). Short flagella exhibited more variable and reduced anterograde IFT speeds, averaging $\sim 1.6\mu\text{m/s}$, while trains in long flagella had a consistent top speed of $\sim 2.3\mu\text{m/s}$ (Fig. 1H). However, reduced anterograde speeds in short flagella cannot explain the increased assembly rate predicted by the balance-point model. Correlating the GFP intensity of anterograde traces with flagellar length revealed an intriguing relationship: IFT trains in short flagella ($2\text{-}6\mu\text{m}$) were over twice as intense as those in long flagella ($8+\mu\text{m}$) (Fig 1I). Furthermore, trains in flagella that were too short to distinguish individual trafficking events ($<2\mu\text{m}$) were 3-4 times as bright as trains in long flagella. Because GFP intensity serves as a proxy for GFP number, we concluded that IFT trains in short flagella contained several-fold more KAP-GFP and IFT27-GFP proteins. Thus, trains in short flagella are functionally larger, with a greater cargo-carrying capacity. While IFT27-GFP had a very low flagellar background signal that was

comparable to the camera noise (Fig. 1F), KAP-GFP had significantly higher background intensity that was brightest in short regenerating flagella (Fig. 1E). However, even when normalized by this background signal, trains in short flagella were over twice as intense as trains in long flagella (Fig. 1I, light blue bars). Because train traffic could not be distinguished in very short flagella ($<2\mu\text{m}$), the flagellar background was not measurable.

Although IFT frequency and particularly IFT speed were reduced in regenerating short flagella, both parameters were uncorrelated with train intensity (Figs. S2A and S2B). This means that while slow trains and large trains are both found in short flagella, large trains are not predisposed to being slow. However, we did uncover a moderate length-independent correlation between IFT speed and frequency, which was strongest within the KAP-GFP data set (Fig. S2C).

To confirm that trains in short flagella contained more KAP protein, we fixed KAP-GFP cells at various timepoints following pH shock and quantified the number of GFP molecules in each train by counting stepwise photobleaching events under TIRF illumination (Fig. 2) (Leake et al., 2006). We chose to focus on the KAP-GFP strain for this experiment because it was created in a *fla3* (KAP point mutant) background, in which only exogenously expressed KAP protein enters the flagella (Fig. S1C) (Mueller et al., 2005). Thus, every KAP protein in the trains is GFP labeled. The IFT27-GFP strain, on the other hand, has a mixture of endogenous and labeled protein in its flagella (Qin et al., 2007). Throughout the timecourse of the bleach, the average fluorescence was measured in regions of interest (ROIs) corresponding to spots of peak intensity

(IFT trains) along the flagella (Fig. 2A). Fluorescence in each ROI was lost in an exponential and stepwise manner, and many steps fit a relatively uniform size (25-60 counts, depending on the imaging session), consistent with single GFP bleaching events (Fig. 2B). Before quantification, the steps were enhanced with an edge-preserving Chung-Kennedy filter (blue line in Fig. 2B) (Chung and Kennedy, 1991; Smith, 1998; Leake et al., 2006). Much like the live-cell experiments, we found that trains in short flagella were enriched with several-fold more KAP-GFP proteins. Trains in long flagella contained an average of 6 KAP-GFP proteins, trains in half-length flagella possessed an average of 10 KAP-GFP, and trains in short flagella held an average of 16 KAP-GFP (Fig. 2C). ROIs in very short flagella ($<2\mu\text{m}$) routinely had over 20 KAP-GFP proteins. Strikingly, this length-dependent 2-4 fold difference in KAP-GFP protein number mirrors the 2-4 fold difference in train intensity seen in Figure 1. Step totals counted by eye were confirmed by dividing the total bleached intensity by the average GFP step size determined for each trace. The tight correlation between the number of GFP steps and the total bleached intensity for each ROI (Fig. S1D) suggests not only that GFP number was accurately quantified, but also that GFP intensity (as reported in Fig. 1) is indeed a strong proxy for GFP protein content.

While these initial studies revealed the relationship between train size and flagellar length, both experiments were susceptible to variability due to comparing data from different images (variability in laser intensity and alignment) of different cells within a population (intrinsic cell-to-cell variability in IFT pool size and GFP expression levels). Fortunately, we were able to address these

concerns thanks to a unique *Chlamydomonas* behavior known as the long-zero response, which occurs when only one of the flagella is severed. During the ~30 minutes following abscission, the two flagella equilibrate in length by shortening the long flagellum as the severed flagellum grows (Rosenbaum et al., 1969). This experiment provides an elegant internally-controlled opportunity to use a single image to compare the IFT dynamics between a long flagellum and short flagellum, both of which are sharing the same limited pool of IFT proteins. When we began our long-zero observations, it was immediately apparent that the shorter flagellum contained trains with higher GFP intensity. Furthermore, greater differences in length between the flagella were accompanied by greater differences in train intensity (Figs. 3A and 3B, Videos 3-6). Quantification revealed a 1:1 linear correlation between train intensity and flagellar length. For example, a flagellum that was half the length of its counterpart would have trains that were twice as bright. (Fig. 3C: a subset of the data, length ratio <4, corrected for flagellar background. Fig. S3: the complete data set, corrected for camera noise). By contrast, the speed and frequency of IFT were similar in both flagella, regardless of the difference in lengths (Figs. 3D and 3E). Based on the pH shock experiment, we expected long flagella to have slightly faster IFT than short flagella, but surprisingly the speeds in long flagella were often reduced (below $2\mu\text{m/s}$). This could be a unique feature of long-zeros, or more generally, a feature of all rapidly shortening flagella.

We also found that, with the exception of long-zeros with one very short flagellum (length ratio >4), both flagella contained roughly the same amount of

total integrated fluorescence (intensity ratio ~ 1 , Fig. S3A). This supports the claim that short and long flagella contain the same quantity of IFT protein (Marshall et al., 2005), and along with the constant frequency of IFT and the linear relationship between train size and flagellar length, suggests a “conservation of mass” in the IFT system. As flagella regenerate, a fixed length-independent quantity of IFT protein is redistributed from fewer large trains to a greater number of small trains (Fig. 4A). Though the mechanism is different than what was originally proposed in the balance-point model, the model’s central dogma remains unchanged. Lengthening of the flagellum results in a lower local concentration of IFT material and axonemal precursors at the flagellar tip, and thus, a lower assembly rate.

It will be of great interest to see if all IFT proteins scale stoichiometrically with KAP and IFT27, or if certain proteins demonstrate a fixed quantity per train, regardless of length. Initial studies of IFT20-GFP (from K. Lechtreck and G. Witman), a peripheral IFT complex B subunit believed to link kinesin with complex B (Baker et al., 2003), indicate that IFT20 train content also scales inversely with flagellar length (data not shown). Our current balance-point model makes the key assumption that all IFT trains carry a proportionate quantity of cargo. This is hard to test directly because the GFP signal of a labeled cargo would be lost in the signal from cargo that has already been incorporated into the axoneme. Nevertheless, a “regulated cargo loading” model has been proposed, where some IFT trains are incapable of binding cargo (Snell et al., 2004). Another assumption in the balance-point model is that IFT train speed is length-

independent. Our data shows that this is not strictly true, as short flagella in the pH shock experiment have reduced IFT speeds (Fig. 1H). However, a modified mathematical model that incorporates this speed variation shows that the measured speeds do not affect the ability of the balance-point system to maintain a defined length (data not shown).

The mechanisms that cause train size to scale inversely with flagellar length remain to be determined. Two distinct models could theoretically explain this behavior: a closed self-rectifying system, or an open system with a length-sensor (Fig. 4B). In a self-rectifying system, flagellar length control is independent of an additional signaling mechanism. Under this regime, the amount of IFT protein available for anterograde train assembly is dependent on the amount of material returned to the base of the flagellum by retrograde transport. As the flagellum lengthens, less IFT components are available at the base of the flagellum and anterograde train size decreases. This model relies on the flagellum being a relatively closed system (no cytoplasmic exchange) for at least one key component of the IFT machinery. In a completely open system, the flagellum would require a length-sensor to modulate the input size of IFT trains. Length-sensors could detect a signal from the flagellar tip, react to changes in ion concentration from channels in the flagellar membrane (Rosenbaum, 2003), or act via a “time of flight” mechanism that would translate the transport time of a trafficking signaling protein (such as a GTPase or kinase) into length measurements (Sloboda and Rosenbaum, 2007). Though several proteins have been shown to play a role in length regulation, including the

flagellar-localized kinases GSK3, LF4p, and Cnk2p (Wilson and Lefebvre, 2004; Berman et al., 2003; Bradley and Quarmby, 2005), a specific length-sensing mechanism has yet to be demonstrated. Differentiating between open and closed flagellar systems would benefit greatly from a *Chlamydomonas* codon-optimized photoactivatable GFP (Patterson and Lippincott-Schwartz, 2002).

An interesting observation that deserves additional investigation is the apparent lack of KAP-GFP retrograde transport. While kymographs of IFT27-GFP (Fig. 1F) and IFT20-GFP (data not shown) have a low background signal and frequent bright retrograde traces, KAP-GFP kymographs have higher background and retrograde traces that are infrequent and far less intense than anterograde traces (Fig. 1E). The lack of bright retrograde KAP-GFP traces is consistent with the observation in *fla11* (IFT172) mutants that kinesin can exit flagella independent of IFT (Pedersen et al., 2006). Without photoactivation, we cannot currently distinguish whether retrograde KAP is undergoing diffusion or whether it is transported back to the base as single molecules, obscured from detection by the flagellar noise. If kinesin does detach from IFT trains at the flagellar tip, this suggests a model for the turnaround of IFT trains where kinesin inhibits dynein during anterograde transport, either through pulling forces alone (Müller et al., 2008) or through protein interactions (Deacon et al., 2003). At the tip, kinesin is removed from IFT trains, immediately licensing dynein for retrograde transport. Such a model would predict a rapid turnaround of trains at the flagellar tip, a premise that can also be tested with photoactivation.

In summary, we have observed in that the size of IFT trains in regenerating *Chlamydomonas* flagella scales inversely and linearly as a function of flagellar length. This provides a plausible mechanism to support the balance-point model of flagellar length control. Based on our observations, we propose that the redistribution of a fixed quantity of IFT protein into IFT trains of variable size drives the length-dependent assembly rate, and thus the kinetics of flagellar regeneration and the steady-state flagellar length. It will be of great interest to see whether IFT is altered in the extensive catalogue of *Chlamydomonas* mutants that exhibit abnormally long (*lf*) or short (*shf*) flagellar lengths (Asleson and Lefebvre, 1998; Kuchka and Jarvik, 1987). It will also be informative to determine how IFT scales with flagellar length in other model systems such as *Trypanosoma*, *Tetrahymena*, *C. elegans*, and vertebrates, all of which have established GFP-reporter systems for observing IFT in live cells (Absalon et al., 2008; Tsao and Gorovsky, 2008; Orozco et al., 1999; Follit et al., 2006). While perhaps not as perfectly suited to studying flagellar regeneration, each of these organisms presents unique characteristics (two flagella of unequal length and age in *Trypanosoma*, for example) that may provide additional insights into the relationship between IFT and flagellar length.

Materials and Methods

Strains and Culture Conditions

Vegetative *Chlamydomonas* cells were grown in Tris-acetate-phosphate (TAP) media (Gorman and Levine, 1965) at 21°C with constant aeration. Wildtype mt+ (cc125), *pf18* mt+ (cc1036), and *pf18* mt- (cc1297) strains were obtained from the *Chlamydomonas* Genetics Center (Duke University, Durham, NC). KAP-GFP *fla3* mt- (Mueller et al., 2005), IFT27-GFP mt+ (Qin et al., 2007), and IFT20-GFP Δ IFT20 (K. Lechtreck, unpublished) strains were provided by M. Porter (University of Minnesota, Minneapolis, MN), J. Rosenbaum (Yale University, New Haven, CT), and G. Witman (University of Massachusetts Medical School, Worcester, MA), respectively. KAP-GFP *fla3 pf18*, IFT27-GFP *pf18*, and KAP-GFP (wildtype *fla3* allele) strains were generated through crosses. All constructs used *Chlamydomonas* codon-optimized GFP (Fuhrmann et al., 1999).

pH shock was performed by transiently lowering the pH of *Chlamydomonas* cultures, as previously described (Lefebvre, 1995). Long-zero regeneration was induced by passing cells through a 28-gauge insulin needle (BD Micro-Fine, #328410), which sheared off only one of the two flagella in a small percentage of the cells.

Live-Cell Microscopy and Image Analysis

For TIRF microscopy, 15 μ L of cells in TAP media were applied to #1.5 (Corning, 22mm x 22mm) coverglass and then inverted onto slides (Gold Seal,

#3010) with a square petroleum jelly spacer. Images were acquired at room temperature with NIS-Elements v2.3 on a Nikon TE2000-E inverted scope equipped with a through-the-objective TIRF system, Nikon Perfect Focus, Nikon 100x/1.49NA and 60x/1.45NA Apo TIRF oil immersion objectives, and a cooled Photometrics QuantEM:512SC EMCCD camera with quantitative gain. Cells were imaged at ~30 frames per second with adjusted TIRF, where the angle of incident light is slightly decreased from the supercritical range toward the critical angle, allowing a deeper range of observation in the area near the coverglass. The depth of illumination was measured to be roughly 250-350nm, using 6 μ m fluorescent beads as described by Mattheyses and Axelrod (2006). All images in each imaging session were acquired using the same angle of incidence and efforts were taken to replicate incidence angles between imaging sessions (though some variability occurred, see Fig. S1D for example). GFP was imaged with 488nm excitation and a 525/50 emission filter.

For DIC imaging, 10 μ L of wildtype cells were immobilized between a 0.25% agarose/TAP pad and the coverglass. The coverglass was then sealed to the slide with VALAP (equal parts petroleum jelly, lanolin, and paraffin) to prevent dehydration. Images were acquired at room temperature with NIS-Elements v2.3 on a TE2000-E inverted scope with a .85NA dry condenser, Nikon 100x/1.4NA oil objective, and a cooled Photometrics CoolSNAP HQ² interline CCD camera. Kymographs of both the TIRF and DIC imaging were generated with Metamorph v7.5.1.0 by drawing a box along the length of the flagella, with a width slightly greater than that of the flagella. The maximum intensity value (for TIRF) or

average intensity (for DIC) for each point along the length of the box was plotted for each frame in the movie, yielding kymographs with spatial information along the x-axis and time along the y-axis. Using NIS-Elements v2.3, kymographs were analyzed for average IFT train intensity, speed, frequency, and integrated flagellar intensity (see Fig. S1B). Intensity measurements were normalized for either camera noise or flagellar background signal. Camera noise was measured as the mean value of an ROI on the kymographs outside of the flagellar region. Flagellar background was measured as the average minimum value of several ROIs placed within the center of each flagellar region.

For the regeneration kinetics in Fig. 1A, cells were fixed every five minutes following pH shock and immediately imaged with an upright Zeiss Axioscop, 40x/.75NA air objective, and Digital Instruments SPOT CCD camera (model 1.4.0). Flagellar lengths at each timepoint were measured using NIS-Elements v3.0.

Fixed-Cell Photobleaching and Step Analysis

At various timepoints following pH shock, 100 μ L of cells were plated onto coverglass and fixed with formaldehyde (4% final concentration) for 10 minutes, shielded from the light. Cells were fixed after plating in order to preserve flagellar adhesion to the coverglass. The coverglass was then dipped in PBS to remove unadhered cells, mounted onto slides with 10 μ L PBS and a petroleum jelly spacer, and sealed with VALAP. Flagella were bleached with the same adjusted TIRF illumination that was used for live-cell imaging. Timeseries (~20 frames per

second) were acquired immediately after locating cells to ensure that the maximal number of bleaching events were recorded.

Mean intensity plots for individual trains were generated in NIS-Elements v2.3 from square ROIs ($0.416\mu\text{m} \times 0.416\mu\text{m}$) corresponding to points of peak intensity along the flagella. Steps were enhanced by filtering the raw data with an edge-preserving Chung-Kennedy algorithm, which passes two adjacent sliding windows of adjustable width (20-60 frames/window) over the dataset and outputs the mean of the window with the lower variance (Leake et al., 2006).

Though every step was not always clear, each intensity plot contained numerous steps of roughly the same size, from which the rest of the steps could be estimated. The number of bleaching events counted by eye was rechecked for each plot by dividing the total change in intensity by the average step size. The geometry of the axoneme in relation to the TIRF field did increase step-size variability, as GFP proteins further from the coverglass were less intense and less likely to photobleach, yielding smaller steps towards the end of the bleach (see Fig. 2B). Importantly, when the whole dataset was plotted together, the total change in intensity of the ROIs was tightly correlated with the number of GFP steps counted, validating the accuracy of the step quantification (Fig. S1D). However, the estimated number of KAP-GFP proteins per train may have been slightly inflated because train bleaching events were inseparable from the flagellar background.

Isolation of Flagella and Western Blotting

Flagella were isolated by pH shock and centrifugation onto a 25% sucrose cushion, as described in Cole et al. (1998). Western blots were probed with rat anti-KAP antibody (obtained from M. Porter; Mueller et al., 2005) at 1:5000, and goat anti-rat HRP secondary antibody (Jackson ImmunoResearch) at 1:20000.

Online Supplemental Material

Fig. S1 shows imaging and photobleaching controls. Fig. S2 shows IFT speed, frequency, and intensity correlations from the pH shock experiment (Fig. 1). Fig. S3 shows the complete raw and normalized data sets from the long-zero experiment (Fig. 3), corrected for camera noise instead of flagellar background. Videos 1-6 show KAP-GFP and IFT27-GFP cells from the pH shock and long zero experiments.

Acknowledgements

We thank Kurt Thorn and the Nikon Imaging Center at UC San Francisco for invaluable microscopy resources and assistance. We also thank Joshua Mueller, Mary Porter, Hongmin Qin, Joel Rosenbaum, Karl Lehtreck and George Witman for generously sharing strains and antibodies, as well as Orion Weiner, Bruce Alberts, Susanne Rafelski, Lani Keller, Sarah Goodwin, and the Marshall Lab for helpful discussions and careful reading of the manuscript. This work was funded by the W. M. Keck Foundation Distinguished Young Scholars Program (W. Marshall), the Searle Scholar Program (W. Marshall), the Genentech Graduate Fellowship (B. Engel), and the NSF Graduate Research Fellowship (W. Ludington).

Author Contributions

B. Engel planned and conducted the experiments, analyzed the results, and wrote the paper. W. Ludington conceived the strategy of quantifying IFT using KAP-GFP and suggested the pH shock and long-zero studies, while B. Engel devised the approach of using TIRF imaging and kymographs to acquire and analyze the data. W. Marshall supervised the project, suggested controls and analyses, and helped with writing the paper.

Figure Legends

Figure 1. During flagellar regeneration, there is an inverse relationship between IFT train size and flagellar length. (A) The kinetics of regeneration following pH shock. N for all timepoints combined: 2026 flagella. (B) The growth rate of regenerating flagella decreases as a function of length. (C) The balance-point model predicts that equilibrium will be reached between a length-independent disassembly rate and an assembly rate that decreases as a function of length. (D) The setup for imaging *Chlamydomonas* flagella via TIRF. Kymographs of (E) KAP-GFP and (F) IFT27-GFP cells undergoing regeneration after pH shock, generated from Videos 1 and 2. Horizontal bars: 5 μ m, vertical bars: 1 sec. The (G) frequency, (H) speed, and (I) average intensity of IFT trains during pH shock regeneration, binned by flagellar length. The intensities of IFT traces were normalized by either camera noise (dark blue and red bars) or background flagellar intensity (light blue bar). N for all timepoints in panels G,H, and I: 113 KAP-GFP flagella, 97 IFT27-GFP flagella, 97 wildtype flagella imaged by DIC. Error bars for all graphs indicate standard deviation.

Figure 2. Quantitative photobleaching confirms that IFT trains in short flagella contain more KAP protein. (A) At different timepoints following pH shock, KAP-GFP cells were fixed and photobleached under constant TIRF illumination. The mean intensity was measured from 0.4 μ m x 0.4 μ m ROIs (red squares) centered on IFT trains. Bar: 2 μ m. (B) Three examples of intensity plots of ROIs from flagella of different lengths. The raw data was filtered with a

Chung-Kennedy edge-preserving algorithm to enhance the detection of stepwise GFP bleaching events. (C) Histograms of the number of KAP-GFP proteins measured in ROIs from long, mid-length, and short flagella (yellow vertical bars denote the mean, yellow horizontal bars show the standard deviation). N: 230 ROIs from 90 flagella.

Figure 3. During long-zero regeneration, there is a linear correlation between IFT train size and flagellar length. (A) Three examples of KAP-GFP cells undergoing long-zero regeneration, showing brighter IFT trains in the shorter of the two flagella (cell dimensions are diagramed above the kymographs). As the length disparity between the long and short flagella increases (kymographs left to right), the difference in average train intensity also increases. Kymographs generated from Videos 3-5. S: short flagella, L: long flagella, C: corrected for camera noise, F: corrected for flagellar background. (B) Example of an IFT27-GFP long-zero cell. Kymograph generated from Video 6. In panels A and B, horizontal bars: 5 μ m, vertical bars: 1 sec. (C) Plotting data from all the KAP-GFP and IFT27-GFP long-zero cells together reveals a linear relationship ($r^2 = 0.86$) between the ratio of flagellar lengths and the ratio of IFT train intensities. Train intensities were corrected for the flagellar background and normalized by the ratio of integrated flagellar intensities (see Figure S3B) to control for variability in total IFT content. Despite this correlation between length and train intensity, the (D) speed and (E) frequency of IFT is the same in both the long and short flagella. Data in panels C, D, and E is plotted on a ratio scale.

Figure 4. *The original and revised balance-point models of flagellar length control, and possible mechanisms of IFT train size modulation.* (A) The original balance-point model predicted that flagella contain a fixed number of IFT trains. Thus, as flagella regenerate, the length-dependent assembly rate would be driven by the decreasing frequency of train arrival at the flagellar tip. This model was refuted by the DIC observation that IFT frequency is constant (Dentler, 2005). In the revised model, the length-dependent assembly rate is mediated by IFT train size that scales inversely with flagellar length. While the total amount of kinesin-2 and IFT protein in a flagellum is length-independent, these proteins are redistributed into a greater number of smaller trains as the flagellum regenerates, reducing the rate of flagellar assembly. (B) Two possible models of train size control. In a closed system, at least one essential component of the IFT machinery does not exchange freely with the cytoplasmic pool. As the flagellum lengthens, lower concentrations of this key protein arrive at the flagellar base via retrograde transport, which results in the production of smaller anterograde IFT trains. In an open system, there is always a high availability of IFT material at the flagellar base, as proteins freely exchange with the large cytoplasmic pool. Thus, an additional length-sensor mechanism is required to modulate the size of trains that enter the flagellum. Blue arrows indicate high IFT protein concentration, while red arrows indicate low concentration.

Figure S1. *Imaging and photobleaching controls.* (A) Analysis of two cells with overlapping flagella confirms that adjusted TIRF microscopy can image through flagella completely. In kymographs of both flagella (bottom center and right images, made from the arrow trajectories in top images), intensity from the other flagellum is visible at the point of intersection (asterisks), demonstrating that the field of illumination is deeper than the width of one flagellum. Bar: 5 μ m.

(B) The methods of kymograph analysis used in this study. IFT frequency was determined by dividing the number of visible traces by the time period of the kymograph, while the transport speed was calculated from the slope of these traces. Train intensity was measured by taking the mean intensity of single-pixel-wide lines that were drawn along each visible trace in the kymograph. The intensities of all the traces were then averaged, yielding the average train intensity for each flagellum. For flagella that were too short to observe train traffic (<2 μ m), intensity was measured as the mean of a line drawn on the flagellum along the time axis. The integrated flagellar intensity was measured as the summed intensity of every pixel in a ROI encompassing the entire flagellar region. Both train and flagella intensities were corrected for camera noise, and train intensities were additionally normalized by the flagellar background signal.

(C) Isolated flagella from wildtype cells, KAP-GFP expressing cells with the endogenous *fla3* KAP point mutation, and two wildtype back-crosses that express KAP-GFP. While the back-crosses contain a mix of endogenous and GFP-labeled KAP in their flagella, the *fla3* cells are enriched nearly exclusively for KAP-GFP, allowing superior quantification. (D) There is a tight linear

correlation (see r^2 values) between the number of GFP steps counted from each ROI photobleaching plot and the total intensity change of the bleach. The slope of this correlation (diagonal lines), and thus the unitary GFP step size, varies slightly by imaging session, but is consistent within each session.

Figure S2. Speed, frequency, and intensity correlations from the live-cell

pH shock experiment (Fig. 1). (A) In the complete dataset, there is a correlation between fast trains and trains with low GFP intensity. However, this is a result of the fact that long flagella consistently have fast, dim trains. When the data is binned into 4-6 μm and 2-4 μm flagellar lengths, the dynamic range where there is the most variability in both speed and intensity, the parameters are uncorrelated. (B) IFT frequency shows no correlation with train intensity, both in the full data set and when binned by short flagella of the same length. (C) Train speed and frequency are moderately correlated, both in the complete data set and when binned into 4-6 μm and 2-4 μm flagellar lengths. In panels A,B, and C, linear-fit r^2 values were calculated using the KAP-GFP dataset.

Figure S3. Complete raw and normalized data sets from the long-zero

experiment (Fig. 3), corrected for camera noise. (A) The complete raw long-zero dataset, showing the ratio of the average train intensity and corresponding ratio of total integrated flagellar intensity for each long-zero. Most long-zeros, particularly those with smaller length ratios, had integrated intensity ratios that were close to 1, indicating that both flagella contained similar quantities of GFP.

Flagella with integrated flagellar intensity ratios significantly greater or less than 1 also had average train intensity ratios that were shifted in the same direction (compare blue with yellow and red with green). This could either reflect transient differences in total protein content between the short and long flagella or could be due to imaging inconsistencies. In particular, the short flagella of long-zeros with high length ratios are so short ($<2\mu\text{m}$) that they do not remain consistently adhered to the coverglass, which may decrease the amount of measured intensity. Unlike Fig. 3, where train intensities were corrected for the flagellar background, here train intensities were corrected for camera noise. This allows display of the complete dataset, as flagellar background cannot be measured for very short flagella. (B) Normalizing the train intensity ratios by the ratios of total flagellar intensity yielded a tighter linear correlation between train intensity and flagellar length. Shown here is the complete normalized long-zero dataset, including long-zeros with length ratios greater than 4, which were excluded from Fig. 3 because the short flagella are so small that individual trains cannot be identified, making IFT speeds and frequencies immeasurable. The data is plotted on a ratio scale.

Supplementary Videos

Video 1. *C. reinhardtii* cell expressing KAP-GFP regenerating flagella following pH shock (from Fig. 1D). Imaged by TIRF microscopy, real-time, 9 seconds, 30 frames per second.

Video 2. *C. reinhardtii* cell expressing IFT27-GFP regenerating flagella following pH shock (from Fig. 1E). Imaged by TIRF microscopy, real-time, 7 seconds, 30 frames per second.

Video 3. *C. reinhardtii* cell expressing KAP-GFP undergoing long-zero flagellar regeneration (from Fig. 3A, left panel). One flagellum is 1.67 times longer than the other flagellum. Notice the difference in flagellar intensities between the short and long flagella. Several seconds in the middle of the video were omitted, where the cell temporarily lost close contact with the coverglass. Imaged by TIRF microscopy, real-time, 11 seconds, 27 frames per second.

Video 4. *C. reinhardtii* cell expressing KAP-GFP undergoing long-zero flagellar regeneration (from Fig. 3A, center panel). One flagellum is 2.47 times longer than the other flagellum. Notice the difference in flagellar intensities between the short and long flagella. Imaged by TIRF microscopy, real-time, 23 seconds, 30 frames per second.

Video 5. *C. reinhardtii* cell expressing KAP-GFP undergoing long-zero flagellar regeneration (from Fig. 3A, right panel). One flagellum is 8.25 times longer than the other flagellum. Notice the difference in flagellar intensities between the short and long flagella. The long flagellum appears to have low intensity due to scaling with the exceptionally bright short flagellum. Imaged by TIRF microscopy, real-time, 18 seconds, 30 frames per second.

Video 6. *C. reinhardtii* cell expressing IFT27-GFP undergoing long-zero flagellar regeneration (from Fig. 3B). One flagellum is 2.39 times longer than the other flagellum. Notice the difference in flagellar intensities between the short and long flagella. Imaged by TIRF microscopy, real-time, 14 seconds, 30 frames per second.

References

- Absalon, S., T. Blisnick, L. Kohl, G. Toutirais, G. Doré, D. Julkowska, A. Tavenet, and P. Bastin. 2008. Intraflagellar transport and functional analysis of genes required for flagellum formation in trypanosomes. *Mol. Biol. Cell.* 19:929-944.
- Axelrod, D. 2001. Total internal reflection fluorescence microscopy in cell biology. *Traffic.* 2:764-774.
- Baker, S. A., K. Freeman, K. Luby-Phelps, G. J. Pazour, and J. C. Besharse. 2003. IFT20 links kinesin II with a mammalian intraflagellar transport complex that is conserved in motile flagella and sensory cilia. *J. Biol. Chem.* 278:34211-34218.
- Berman, S. A., N. F. Wilson, N. A. Haas, and P. A. Lefebvre. 2003. A novel MAP kinase regulates flagellar length in *Chlamydomonas*. *Curr. Biol.* 13:1145-1149.
- Bisgrove, B. W. and H. J. Yost. 2006. The roles of cilia in developmental disorders and disease. *Development.* 133:4131-4143.
- Bloodgood, R. A. 1995. Flagellar surface motility: gliding and microsphere movements. *Methods Cell Biol.* 47:273-279.
- Bradley, B. A. and L. M. Quarmby. 2005. A NIMA-related kinase, Cnk2p, regulates both flagellar length and cell size in *Chlamydomonas*. *J. Cell Sci.* 118:3317-3326.
- Chung, S. H. and R. A. Kennedy. 1991. Forward-backward non-linear filtering technique for extracting small biological signals from noise. *J. Neurosci. Methods.* 40:71-86.
- Cole, D. G. 2003. The intraflagellar transport machinery of *Chlamydomonas reinhardtii*. *Traffic.* 4:435-442.
- Cole, D. G., D. R. Diener, A. L. Himelblau, P. L. Beech, J. C. Fuster, and J. L. Rosenbaum. 1998. *Chlamydomonas* kinesin-II-dependent intraflagellar transport (IFT): IFT particles contain proteins required for ciliary assembly in *Caenorhabditis elegans* sensory neurons. *J. Cell Biol.* 141:993-1008.
- Deacon, S. W., A. S. Serpinskaya, P. S. Vaughan, M. Lopez Fanarraga, I. Vernos, K. T. Vaughan, and V. I. Gelfand. 2003. Dynactin is required for bidirectional organelle transport. *J. Cell Biol.* 160:297-301.
- Dentler, W. 2005. Intraflagellar transport (IFT) during assembly and disassembly of *Chlamydomonas* flagella. *J. Cell Biol.* 170:649-659.
- Follit, J. A., R. A. Tuft, K. E. Fogarty, and G. J. Pazour. 2006. The intraflagellar transport protein IFT20 is associated with the Golgi complex and is required for cilia assembly. *Mol. Biol. Cell.* 17:3781-3792.
- Fuhrmann, M., W. Oertel, and P. Hegemann. 1999. A synthetic gene coding for the green fluorescent protein (GFP) is a versatile reporter in *Chlamydomonas reinhardtii*. *Plant J.* 19:353-361.
- Gorman, D. S. and R. P. Levine. 1965. Cytochrome f and plastocyanin: their sequence in the photosynthetic electron transport chain of *Chlamydomonas reinhardi*. *Proc. Natl. Acad. Sci. USA.* 54:1665-1669.

- Hou, Y., H. Qin, J. A. Follit, G. J. Pazour, J. L. Rosenbaum, and G. B. Witman. 2007. Functional analysis of an individual IFT protein: IFT46 is required for transport of outer dynein arms into flagella. *J. Cell Biol.* 176:653-665.
- Huang, B., M. R. Rifkin, and D. J. Luck. 1977. Temperature-sensitive mutations affecting flagellar assembly and function in *Chlamydomonas reinhardtii*. *J. Cell Biol.* 72:67-85.
- Iomini, C., V. Babaev-Khaimov, M. Sassaroli, and G. Piperno. 2001. Protein particles in *Chlamydomonas* flagella undergo a transport cycle consisting of four phases. *J. Cell Biol.* 153:13-24.
- Kozminski, K. G., P. L. Beech, and J. L. Rosenbaum. 1995. The *Chlamydomonas* kinesin-like protein FLA10 is involved in motility associated with the flagellar membrane. *J. Cell Biol.* 131:1517-1527.
- Kozminski, K. G., K. A. Johnson, P. Forscher, and J. L. Rosenbaum. 1993. A motility in the eukaryotic flagellum unrelated to flagellar beating. *Proc. Natl. Acad. Sci. USA.* 90:5519-5523.
- Leake, M. C., J. H. Chandler, G. H. Wadhams, F. Bai, R. M. Berry, and J. P. Armitage. 2006. Stoichiometry and turnover in single, functioning membrane protein complexes. *Nature.* 443:355-358.
- Lefebvre, P. A. 1995. Flagellar amputation and regeneration in *Chlamydomonas*. *Methods Cell Biol.* 47:3-7.
- Marshall, W. F. and J. L. Rosenbaum. 2001. Intraflagellar transport balances continuous turnover of outer doublet microtubules: implications for flagellar length control. *J. Cell Biol.* 155:405-414.
- Marshall, W. F., H. Qin, M. Rodrigo Brenni, and J. L. Rosenbaum. 2005. Flagellar length control system: testing a simple model based on intraflagellar transport and turnover. *Mol. Biol. Cell.* 16:270-278.
- Mattheyses, A. L. and D. Axelrod. 2006. Direct measurement of the evanescent field profile produced by objective-based total internal reflection fluorescence. *J. Biomed. Opt.* 11:014006.
- Mueller, J., C. A. Perrone, R. Bower, D. G. Cole, and M. E. Porter. 2005. The FLA3 KAP subunit is required for localization of kinesin-2 to the site of flagellar assembly and processive anterograde intraflagellar transport. *Mol. Biol. Cell.* 16:1341-1354.
- Müller, M. J., S. Klumpp, and R. Lipowsky. 2008. Tug-of-war as a cooperative mechanism for bidirectional cargo transport by molecular motors. *Proc. Natl. Acad. Sci. USA.* 105:4609-4614.
- Orozco, J. T., K. P. Wedaman, D. Signor, H. Brown, L. Rose, and J. M. Scholey. 1999. Movement of motor and cargo along cilia. *Nature.* 398:674.
- Ou, G., M. Koga, O. E. Blacque, T. Murayama, Y. Ohshima, J. C. Schafer, C. Li, B. K. Yoder, M. R. Leroux, and J. M. Scholey. 2007. Sensory ciliogenesis in *Caenorhabditis elegans*: assignment of IFT components into distinct modules based on transport and phenotypic profiles. *Mol. Biol. Cell.* 18:1554-1569.
- Pan, J. and W. J. Snell. 2005. *Chlamydomonas* shortens its flagella by activating axonemal disassembly, stimulating IFT particle trafficking, and blocking anterograde cargo loading. *Dev Cell.* 9:431-438.

- Parker, J. D. and L. M. Quarmby. 2003. *Chlamydomonas* fla mutants reveal a link between deflagellation and intraflagellar transport. *BMC Cell Biol.* 4:11.
- Patterson, G. H. and J. Lippincott-Schwartz. 2002. A photoactivatable GFP for selective photolabeling of proteins and cells. *Science.* 297:1873-1877.
- Pazour, G. J., B. L. Dickert, and G. B. Witman. 1999. The DHC1b (DHC2) isoform of cytoplasmic dynein is required for flagellar assembly. *J. Cell Biol.* 144:473-481.
- Pazour, G. J. and J. L. Rosenbaum. 2002. Intraflagellar transport and cilia-dependent diseases. *Trends Cell Biol.* 12:551-555.
- Pedersen, L. B., S. Geimer, and J. L. Rosenbaum. 2006. Dissecting the molecular mechanisms of intraflagellar transport in *Chlamydomonas*. *Curr. Biol.* 16:450-459.
- Pedersen, L. B., M. S. Miller, S. Geimer, J. M. Leitch, J. L. Rosenbaum, and D. G. Cole. 2005. *Chlamydomonas* IFT172 is encoded by FLA11, interacts with CrEB1, and regulates IFT at the flagellar tip. *Curr. Biol.* 15:262-266.
- Pigino, G., Geimer, S., Lanzavecchia, S., Paccagnini, E., Cantele, F., Diener, D. R., Rosenbaum, J. L., and Lupetti, P. 2009. Electron-tomographic analysis of intraflagellar transport particles in situ. *J. Cell Biol.* [submitted]
- Piperno, G. and K. Mead. 1997. Transport of a novel complex in the cytoplasmic matrix of *Chlamydomonas* flagella. *Proc. Natl. Acad. Sci. USA.* 94:4457-4462.
- Piperno, G., E. Siuda, S. Henderson, M. Segil, H. Vaananen, and M. Sassaroli. 1998. Distinct mutants of retrograde intraflagellar transport (IFT) share similar morphological and molecular defects. *J. Cell Biol.* 143:1591-601.
- Qin, H., D. R. Diener, S. Geimer, D. G. Cole, and J. L. Rosenbaum. 2004. Intraflagellar transport (IFT) cargo: IFT transports flagellar precursors to the tip and turnover products to the cell body. *J. Cell Biol.* 164:255-266.
- Qin, H., Z. Wang, D. Diener, and J. L. Rosenbaum. 2007. Intraflagellar transport protein 27 is a small G protein involved in cell-cycle control. *Curr. Biol.* 17:193-202.
- Randall, J., H. R. Munden, and P. H. Prest. 1969. The flagellar apparatus as a model organelle for the study of growth and morphopoiesis. *Proc. R. Soc. Lond. B. Biol. Sci.* 173:31-62.
- Rosenbaum, J. L. 2003. Organelle size regulation: length matters. *Curr Biol.* 13:R506-507.
- Rosenbaum, J. L., J. E. Moulder, and D. L. Ringo. 1969. Flagellar elongation and shortening in *Chlamydomonas*. The use of cycloheximide and colchicine to study the synthesis and assembly of flagellar proteins. *J. Cell Biol.* 41:600-619.
- Silflow, C. D. and P. A. Lefebvre. 2001. Assembly and Motility of Eukaryotic Cilia and Flagella. Lessons from *Chlamydomonas reinhardtii*. *Plant Physiol.* 127:1500-1507.
- Sloboda, R. D. and L. Howard. 2007. Localization of EB1, IFT polypeptides, and kinesin-2 in *Chlamydomonas* flagellar axonemes via immunogold scanning electron microscopy. *Cell Motil. Cytoskeleton.* 64:446-460.
- Sloboda, R. D. and J. L. Rosenbaum. 2007. Making sense of cilia and flagella. *J. Cell Biol.* 179:575-582.

Smith, D. A. 1998. A quantitative method for the detection of edges in noisy time-series. *Philos. Trans. R. Soc. Lond. B. Biol. Sci.* 353:1969-1981.

Snell, W. J., J. Pan, and Q. Wang. 2004. Cilia and flagella revealed: from flagellar assembly in *Chlamydomonas* to human obesity disorders. *Cell.* 117:693-697.

Tsao, C. C. and M. A. Gorovsky. 2008. Different effects of Tetrahymena IFT172 domains on anterograde and retrograde intraflagellar transport. *Mol. Biol. Cell.* 19:1450-1461.

Wilson, N. F. and P. A. Lefebvre. 2004. Regulation of flagellar assembly by glycogen synthase kinase 3 in *Chlamydomonas reinhardtii*. *Eukaryot. Cell.* 3:1307-1319.

Figure 1.1

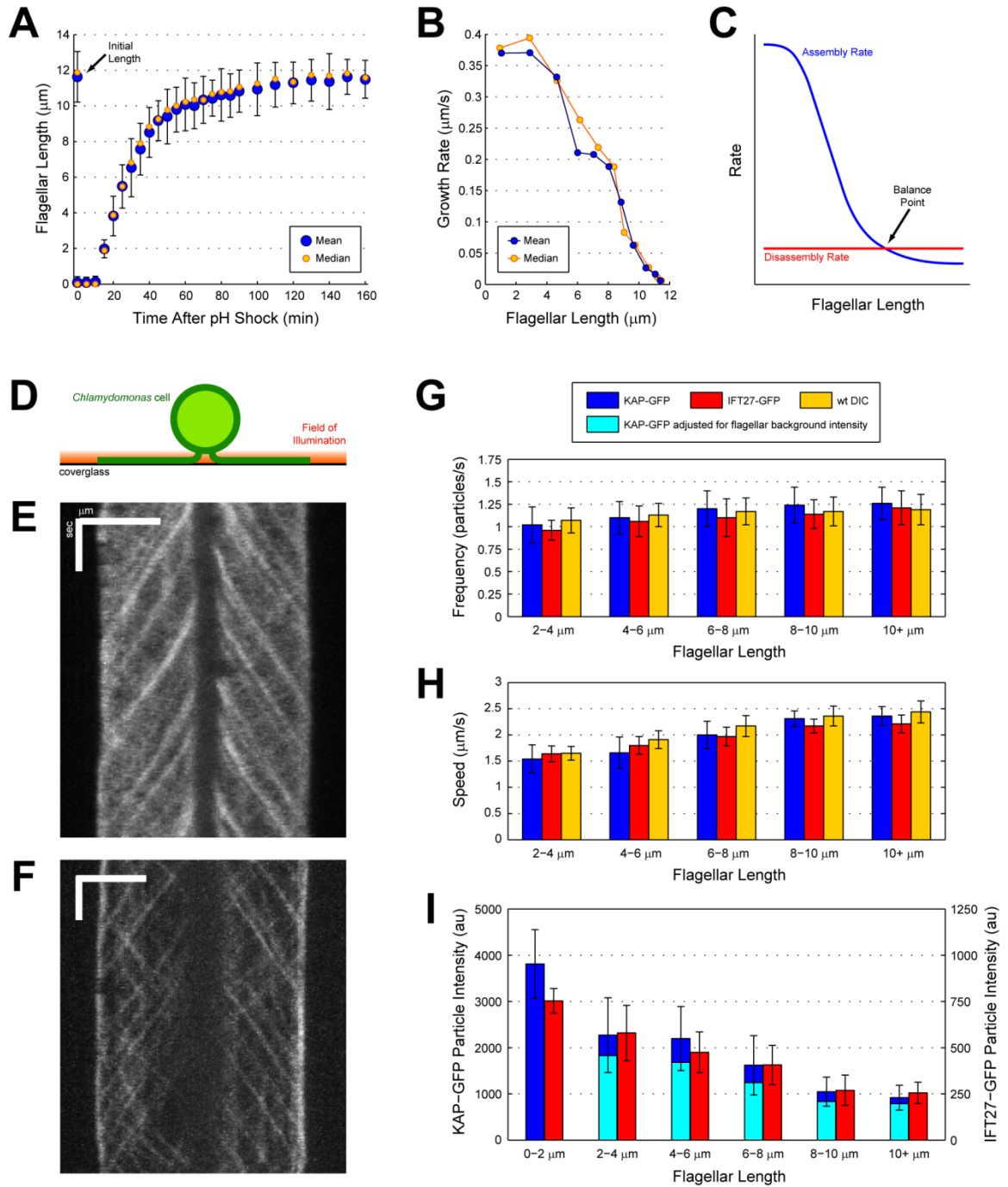


Figure 1.2

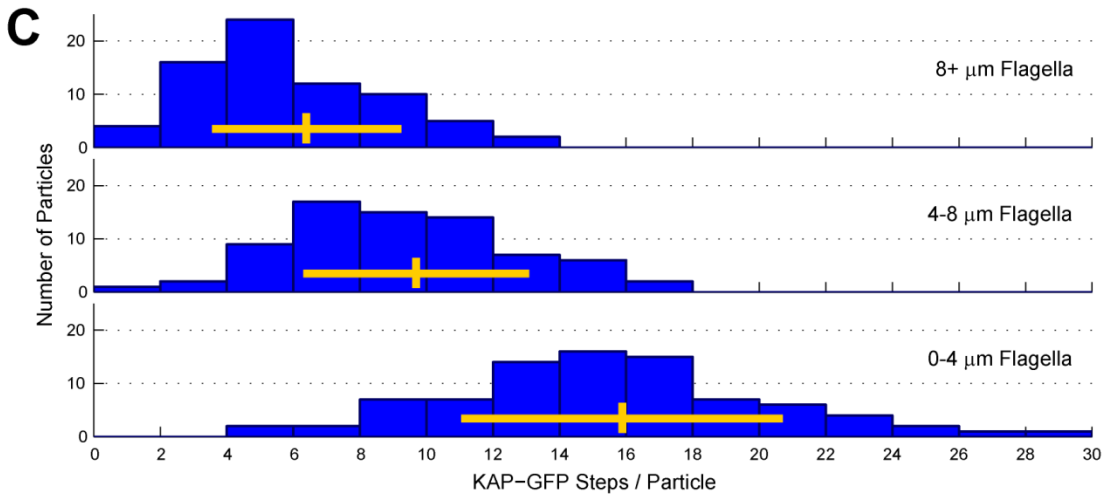
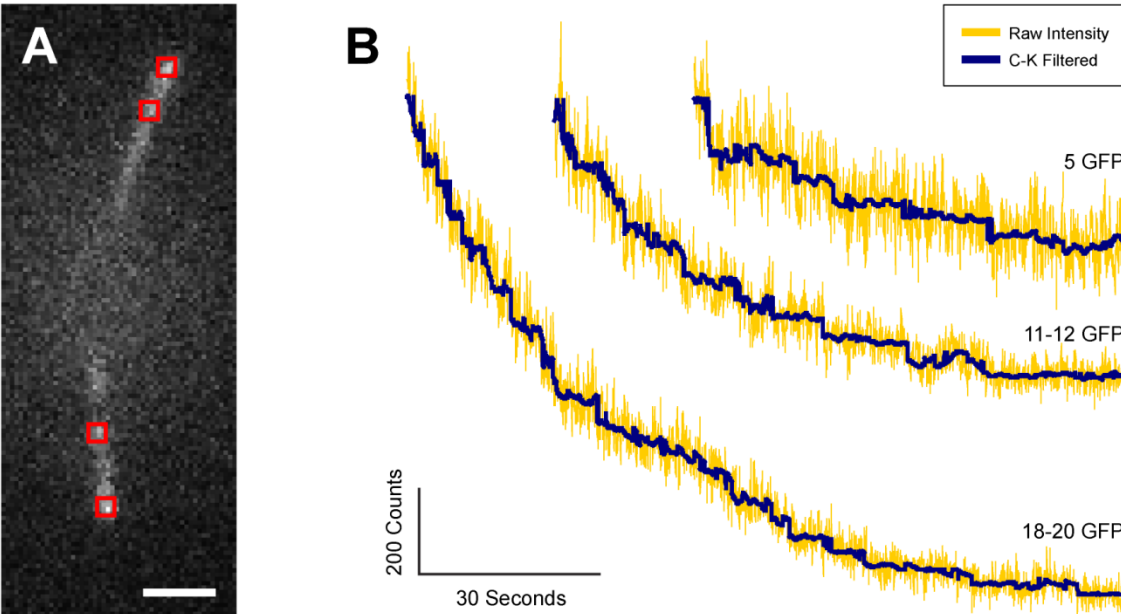


Figure 1.3

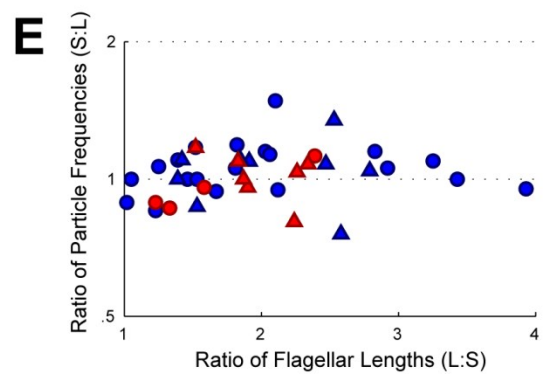
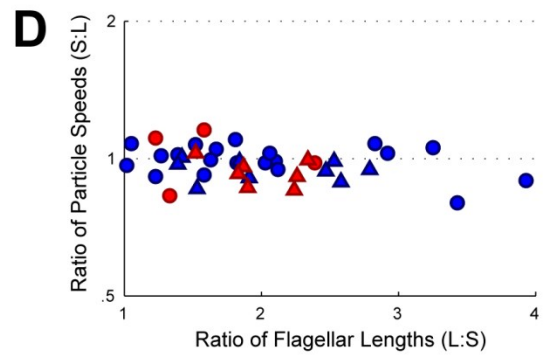
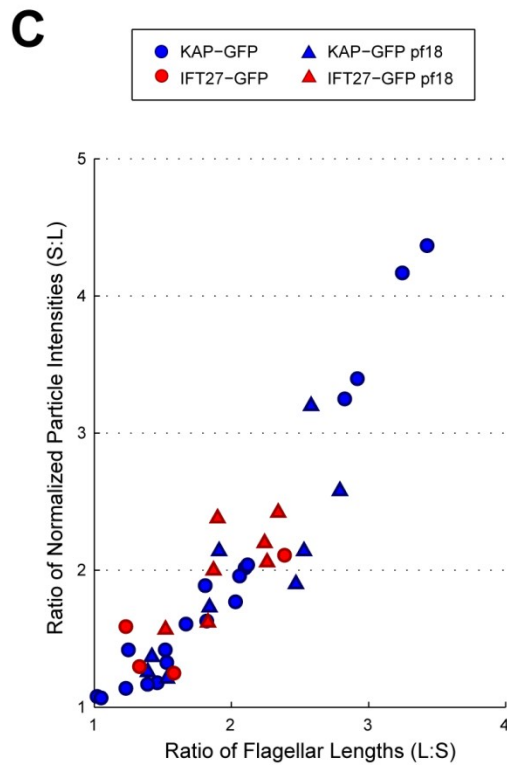
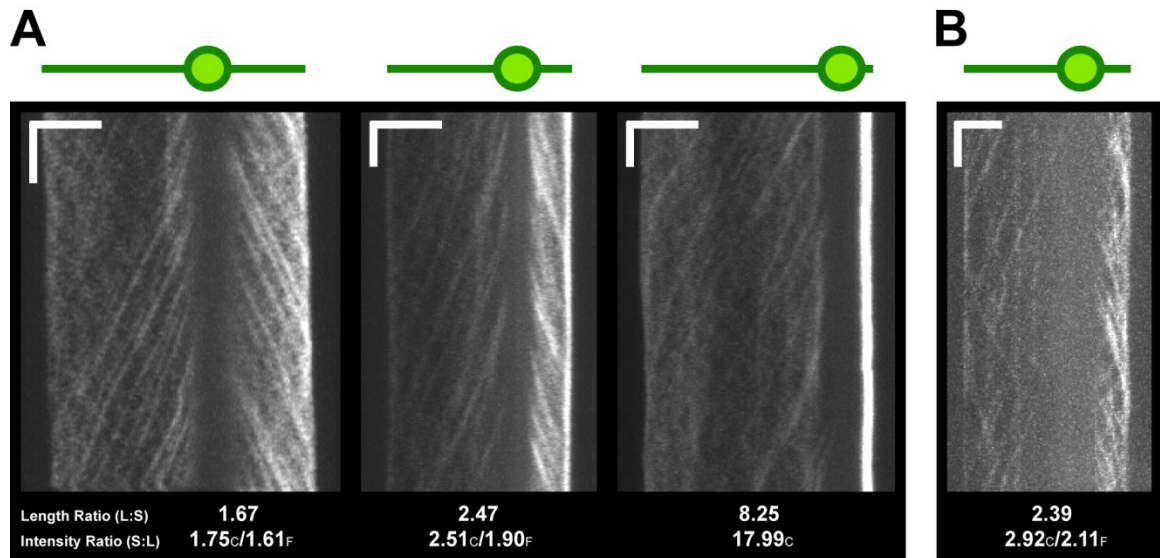
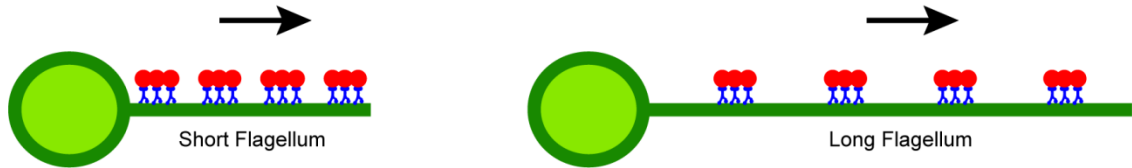


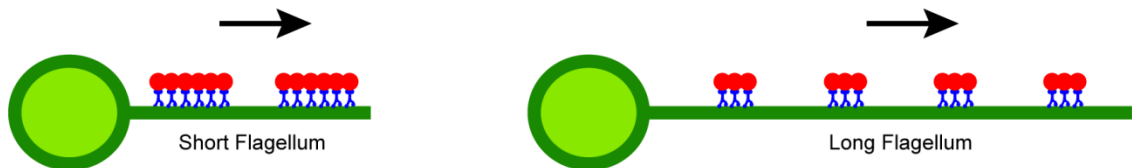
Figure 1.4

A

Original Balance-Point Model: Variable IFT Frequency



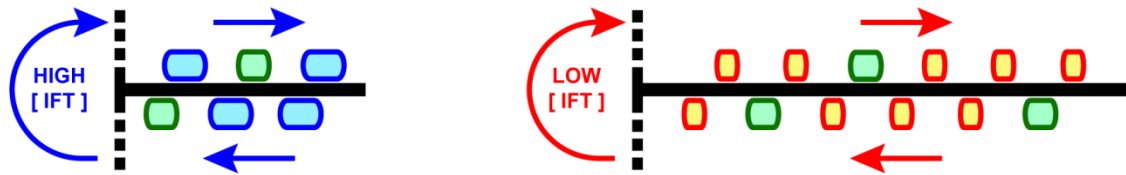
Revised Balance-Point Model: Variable IFT Particle Size



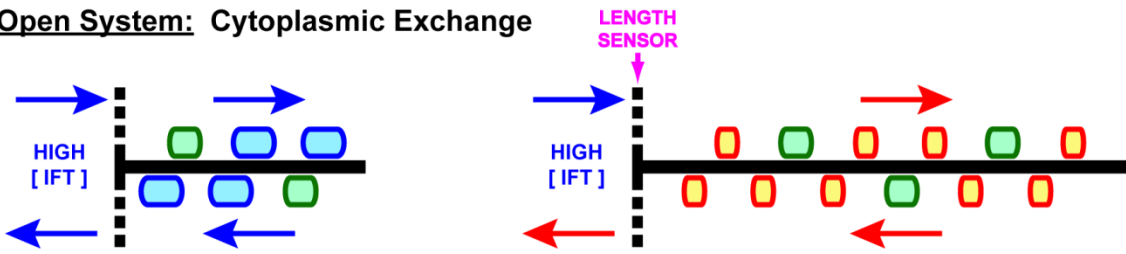
● IFT Proteins Y Kinesin-II

B

Closed System: No Cytoplasmic Exchange



Open System: Cytoplasmic Exchange



□ Large Particle □ Midsize Particle □ Small Particle

Figure 1.S1

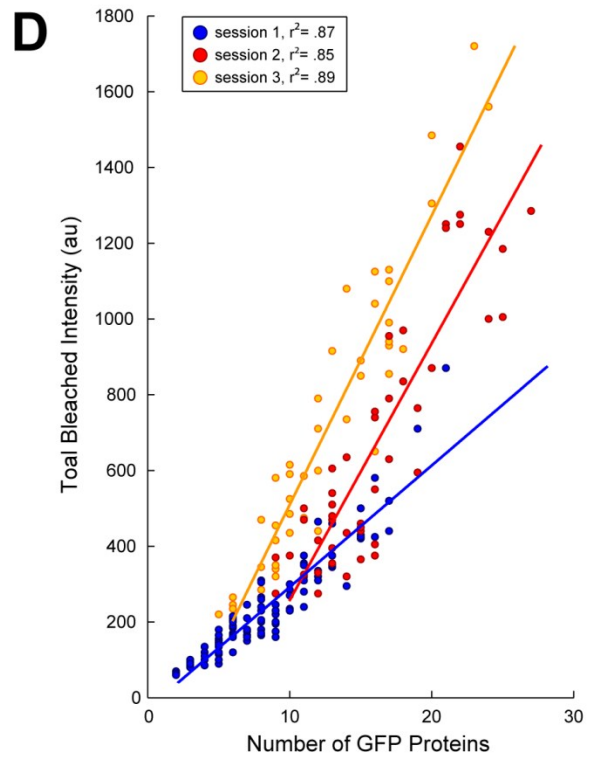
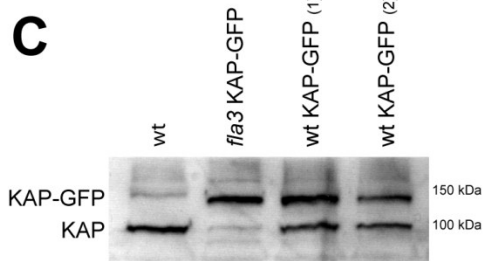
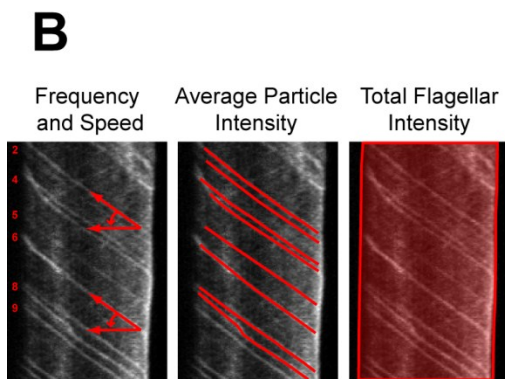
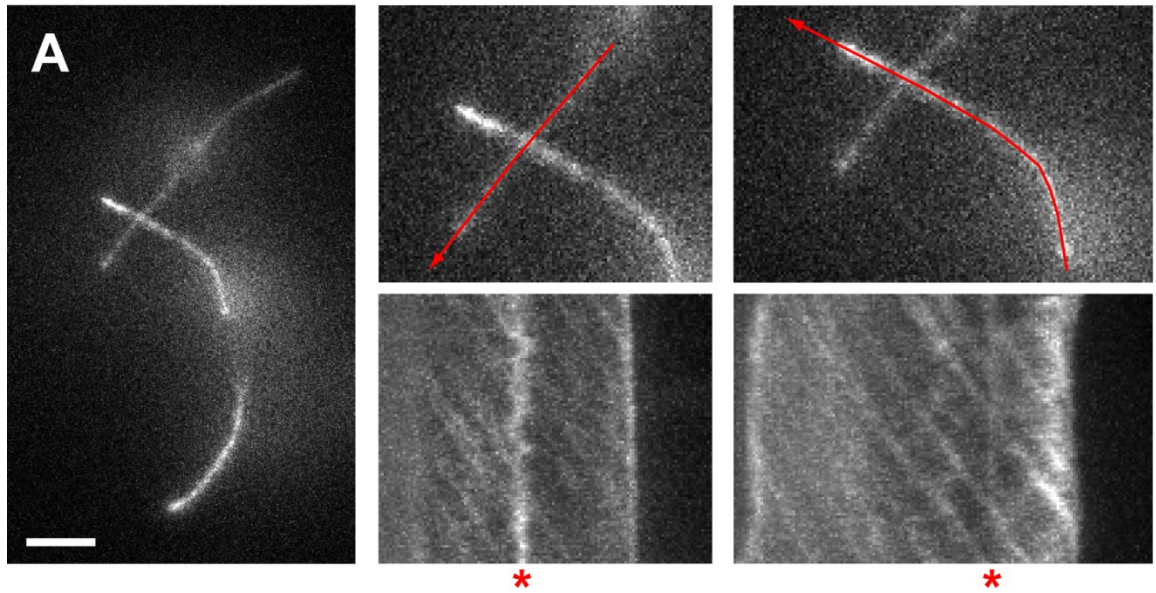


Figure 1.S2

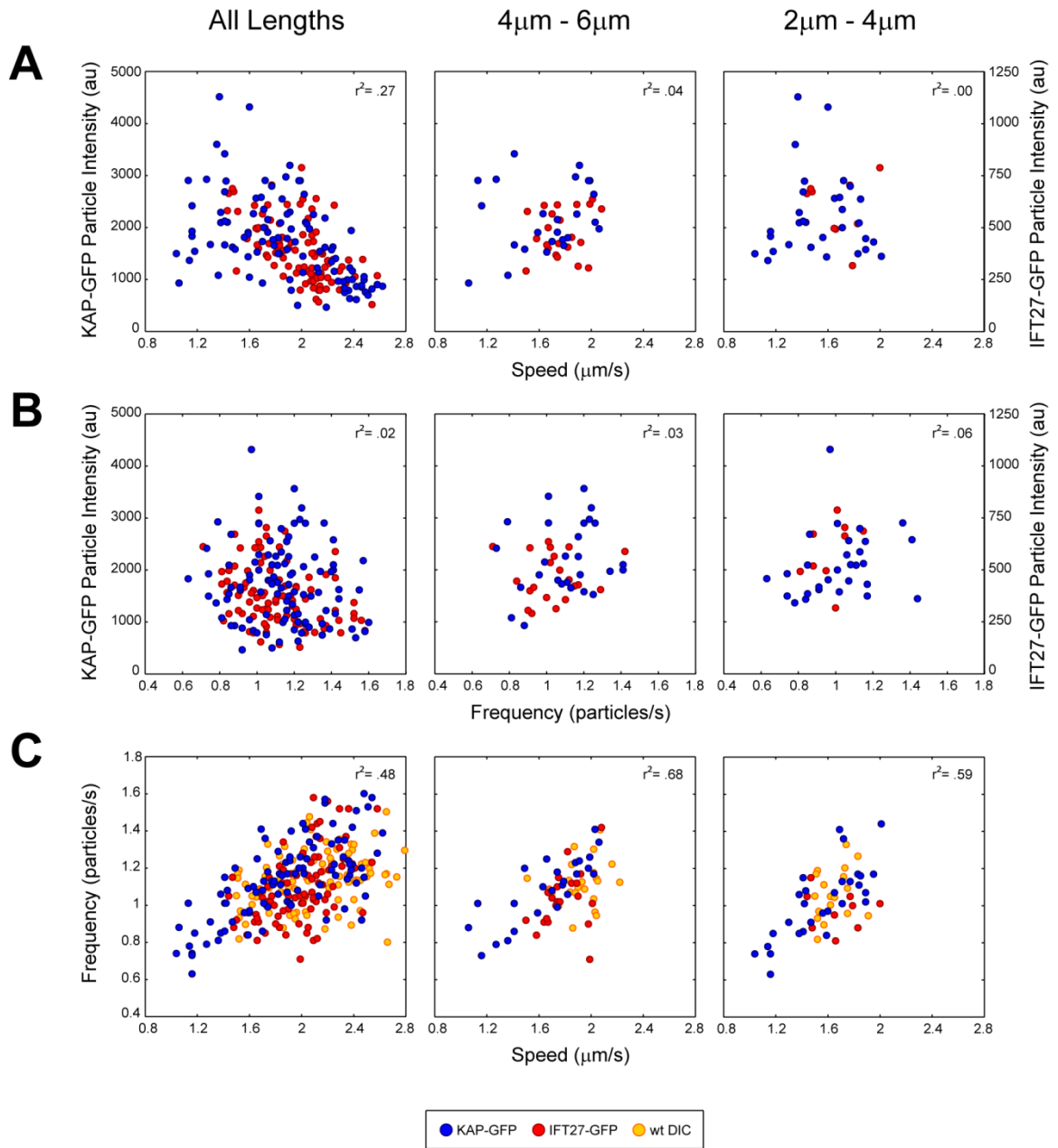
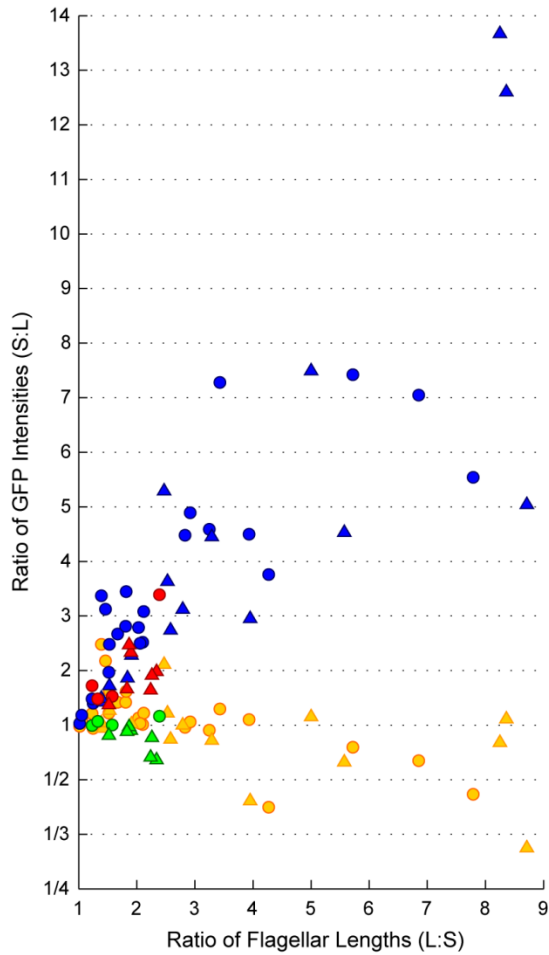
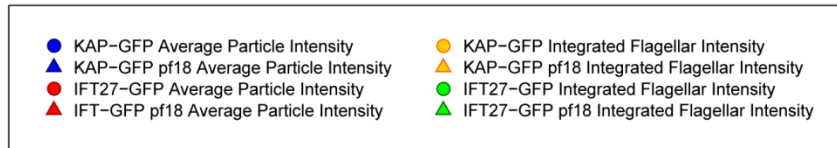
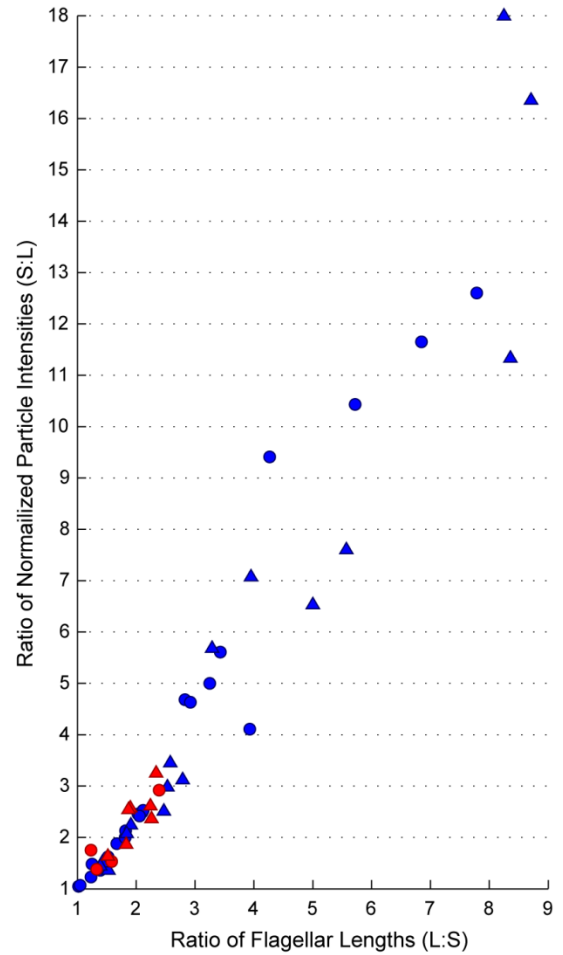


Figure 1.S3

A Average Particle Intensity and Integrated Flagellar Intensity



B Average Particle Intensity Normalized by Integrated Flagellar Intensity



Chapter 2

Total Internal Reflection Fluorescence (TIRF) Microscopy of *Chlamydomonas* Flagella

Benjamin D. Engel¹, Karl-Ferdinand Lehtreck², George B. Witman²,
& Wallace F. Marshall¹

1. Dept. of Biochemistry & Biophysics, UCSF
2. Department of Cell Biology, University of Massachusetts Medical School

Originally published in *Methods in Cell Biology*, 93:157-77, December 2009.

Abstract

The eukaryotic flagellum is host to a variety of dynamic behaviors, including flagellar beating, the motility of glycoproteins in the flagellar membrane, and intraflagellar transport (IFT), the bidirectional traffic of protein particles between the flagellar base and tip. IFT is of particular interest, as it plays integral roles in flagellar length control, cell signaling, development, and human disease. However, our ability to understand dynamic flagellar processes such as IFT is limited in large part by the fidelity with which we can image these behaviors in living cells. This chapter introduces the application of total internal reflection fluorescence (TIRF) microscopy to visualizing the flagella of *Chlamydomonas reinhardtii*. The advantages and challenges of TIRF are discussed in comparison to confocal and differential interference contrast (DIC) techniques. This chapter also reviews current IFT insights gleaned from TIRF microscopy of *Chlamydomonas* and provides an outlook on the future of the technique, with particular emphasis on combining TIRF with other emerging imaging technologies.

Article Outline

I. Introduction

II. Rationale: A History of Flagellar Microscopy in *Chlamydomonas*

A. Phase Contrast and Dark Field: Early Insights into Flagellar Motilities

B. DIC: The Discovery and Initial Characterization of IFT

C. Fluorescence: Algae Meet GFP

D. TIRF Microscopy: A Perfect Match for *Chlamydomonas*

III. Materials and Methods: Technical Considerations of *Chlamydomonas* TIRF

A. Slide Preparation and Cell Immobilization

B. The Angle of Incidence and Depth of the TIRF Field

C. GFP Labeling of *Chlamydomonas* Flagellar Proteins

IV. Discussion: Future Prospects for *Chlamydomonas* TIRF

A. Simultaneous Multi-Color TIRF

B. FRAP, Photoactivation, and Photoconversion

C. Applications Beyond IFT

V. Summary

Acknowledgements

References

I. Introduction

Nearly every cell in the human body projects a primary cilium from its apical surface into the extracellular environment. Once thought to be a vestigial remnant from our days as single-celled organisms, the primary cilium is now appreciated both as a mechanosensory organelle and as a specialized compartment for signaling pathways such as Hedgehog and PDGFR $\alpha\alpha$ (Huangfu *et al.*, 2003; Schneider *et al.*, 2005; Singla and Reiter, 2006). Meanwhile, ciliary defects have been implicated in a wide array of human disorders, from polycystic kidney disease to retinal degeneration and hydrocephalus (Pazour and Rosenbaum, 2002; Bisgrove and Yost, 2006; Lechtreck *et al.*, 2008).

For over 40 years, the humble green alga *Chlamydomonas reinhardtii* has carried the banner of flagellar biology. *Chlamydomonas* possesses a wealth of flagellar mutants, which have greatly informed our understanding of these organelles. The cell's two flagella (identical to cilia in every way but their name) are readily purified for biochemical studies (King, 1995) and are amenable to numerous experimental perturbations, including regeneration after amputation (Rosenbaum *et al.*, 1969; Lefebvre, 1995). However, one of this little alga's greatest contributions to flagellar biology was the discovery and characterization of intraflagellar transport (IFT).

IFT is indispensable for the assembly and maintenance of eukaryotic flagella. The only way for axonemal precursors to reach the site of flagellar assembly at the flagellar tip is to be carried there by large IFT particles, powered

by the anterograde motor heterotrimeric kinesin-2. At the tip, IFT particles are remodeled and loaded with axonemal turnover products for their return trip to the cell body, driven by the retrograde motor cytoplasmic dynein-1b. The IFT machinery is highly evolutionarily conserved and many *Chlamydomonas* genes that encode IFT proteins are homologous to human disease genes (Pazour *et al.*, 2000).

IFT is a live-cell microscopy-defined phenomenon. Though IFT particles (originally dubbed “rafts”) had been observed in electron micrographs for decades, their function was not understood until IFT was visualized by DIC microscopy (Kozminski *et al.*, 1993). Subsequent biochemistry studies have revealed much about the composition (Piperno and Mead, 1997; Cole *et al.*, 1998) of IFT particles, as well as their interactions with specific axonemal precursors (Qin *et al.*, 2004; Hou *et al.*, 2007). In addition, cryo-electron tomography studies have produced insights into the modular 3D architecture of IFT particles (Pigino *et al.*, 2007). However, since IFT is a description of the movement of proteins, live-cell microscopy remains an invaluable technique for understanding this important cellular behavior. In this paper, we briefly review the history of transmitted light and fluorescence microscopy in *Chlamydomonas* and then detail the promising new application of TIRF microscopy to studying IFT and other dynamic flagellar processes.

II. Rationale: A History of Flagellar Microscopy in

Chlamydomonas

A. Phase Contrast and Dark Field: Early Insights into Flagellar Motilities

Each new advance in imaging technology has yielded fresh perspectives on the numerous dynamic processes of *Chlamydomonas* flagella. Phase contrast microscopy was central to many of the early descriptions of *Chlamydomonas* flagellar behaviors, including the kinetics of flagellar regeneration and shortening under a variety of conditions (Rosenbaum *et al.*, 1969). Decades later, these careful measurements still provide the foundation for investigations into flagellar length control. Phase contrast was also utilized to observe the dynamic bidirectional movements of polystyrene microspheres along the surface of the flagellar membrane (Bloodgood, 1977). This motility was later associated with the movements of flagellar glycoproteins and *Chlamydomonas* gliding motility, which occurs when the cell's flagella adhere to a solid surface (Bloodgood, 1995). Dark field microscopy, which provides enough contrast to visualize the dynamic instability of individual microtubules, was used to elegantly observe the rotation of the central pair microtubules in detergent-treated *Chlamydomonas* flagella (Kamiya, 1982). However, little was known about the traffic of proteins within eukaryotic flagella until researchers began examining *Chlamydomonas* with differential interference contrast (DIC) microscopy.

B. DIC: The Discovery and Initial Characterization of IFT

IFT was first described by video-enhanced DIC microscopy in 1993 (Kozminski *et al.*, 1993), and for the following decade, this was the only technique available for visualizing IFT in living *Chlamydomonas* cells. While the molecular identities of the IFT proteins were elucidated by biochemistry, these experiments were guided by DIC microscopy of temperature-sensitive mutants. Following identification of the *fla10* mutant as a “kinesin-like protein” (Walther *et al.*, 1994; later shown to be part of heterotrimeric kinesin-2 by Cole *et al.*, 1998), DIC microscopy of *fla10* at the restrictive temperature revealed that kinesin-2 was required for IFT (Kozminski *et al.*, 1995a). Two groups took advantage of this observation to identify at least 15 IFT proteins that were depleted from *fla10* flagella at the restrictive temperature (Piperno and Mead, 1997; Cole *et al.*, 1998). Thus, microscopy steered the biochemical isolation of the IFT proteins, and throughout the subsequent years, DIC mutant analysis continued to shed light on the mechanisms of IFT. For instance, the loss of only retrograde trafficking events in *fla15*, *fla16*, and *fla17* mutants correlated with the specific depletion of IFT complex A proteins from flagella, implying that complex A is exclusively required for retrograde transport (Piperno *et al.*, 1998). While the wild-type speeds of anterograde and retrograde transport were reported with the initial description of IFT, detailed DIC kymograph analysis of speeds and frequencies enabled numerous *fla* mutants to be classified as defective in one or more stages of IFT: particle loading at the base, anterograde transport, particle turnaround at the tip, and retrograde transport (Iomini *et al.*, 2001). DIC

kymograph analysis has also revealed that the frequency of IFT is relatively constant in shortening, lengthening, and steady-state flagella (Dentler, 2005).

Although DIC microscopy was invaluable for the discovery and initial characterization of IFT, the technique suffers from a few major limitations. The quality of IFT visualization is highly contingent on how flagella are oriented in relation to the axis of shear (parallel provides the greatest contrast). DIC quality also varies depending on how flagella are immobilized (certain paralyzed strains work better than others and mounting cells on agarose pads decreases resolution; Kozminski, 1995b). However, the greatest drawback of DIC is the inability to distinguish the traffic of specific proteins. Although combining DIC with temperature-sensitive mutants enabled the correlation of different IFT proteins with distinct IFT behaviors (Piperno *et al.*, 1998; Iomini *et al.*, 2001), these observations are indirect. In order to further tease apart the intricacies of IFT, it is necessary to examine the dynamics of specific IFT proteins and cargos through fluorescence microscopy.

C. Fluorescence: Algae Meet GFP

The first fluorescence imaging of IFT was achieved in *C. elegans* in 1999 (Orozco *et al.*, 1999). In the last decade, tremendous work has gone into characterizing IFT in worms and nearly 20 IFT proteins have now been tagged with green fluorescent protein (GFP) (Snow *et al.*, 2004; Blacque *et al.*, 2006; Mukhopadhyay *et al.*, 2007; Ou *et al.*, 2007). By quantifying IFT speeds in several mutants, these worm studies provided insights into the coordination of

different IFT proteins and anterograde motors (Ou *et al.*, 2005). Efforts to visualize IFT with GFP in other organisms, including *Chlamydomonas* (Mueller *et al.*, 2005; Qin *et al.*, 2007) *Trypanosoma* (Absalon *et al.*, 2008) and mammalian cells (Follit *et al.*, 2006), lagged behind for several years but are currently all areas of active research. Due to its GC-codon bias, *Chlamydomonas* does not easily express many foreign proteins (Heitzer *et al.*, 2007). At the same time that the first fluorescent IFT proteins were being put into worms, *Chlamydomonas* received a codon-optimized EGFP that fortuitously eliminated a cryptic splice site from the original sequence (Fuhrmann *et al.*, 1999). Six years later, KAP (kinesin-associated protein, the non-motor subunit of heterotrimeric kinesin-2) became the first GFP-labeled IFT protein in *Chlamydomonas* (Fig. 2E; Mueller *et al.*, 2005). Since then, additional IFT proteins have been tagged, including IFT27 (Fig. 2D; Qin *et al.*, 2007), IFT20 (Fig. 2B, 2C and Fig. 4; Lechtreck *et al.*, 2009a), and BBS4 (Fig. 4; Lechtreck *et al.*, 2009a). The signaling protein CrPKD2 has also been labeled with GFP, revealing that ~10% of flagellar CrPKD2 undergoes anterograde transport, likely as an IFT cargo (Huang *et al.*, 2007).

While fluorescence imaging of IFT in *Chlamydomonas* has its share of hurdles (difficulties with protein expression, no homologous recombination, cells are autofluorescent and highly motile), there are significant advantages as well. At ~12 μ m, wild-type *Chlamydomonas* flagella are twice as long as *C. elegans* sensory cilia and most mammalian primary cilia, enabling a more detailed analysis of protein traffic. Furthermore, *Chlamydomonas* flagella extend away

from the cell body, which greatly enhances the signal-to-noise ratio by allowing the flagella to be imaged upon a dark background. In contrast, mammalian primary cilia must contend with the backdrop of a GFP-expressing cell. Finally, *Chlamydomonas* is endowed with a rich catalogue of flagellar mutants, such as the kinesin-2 mutant *fla10* (Huang *et al.*, 1977; Walther *et al.*, 1994), which can be mated to GFP-tagged strains to observe altered IFT dynamics.

D. TIRF Microscopy: A Perfect Match for Chlamydomonas

The imaging advantages of examining GFP-labeled flagellar proteins in *Chlamydomonas* become significantly pronounced with the addition of TIRF microscopy. While spinning disk confocal microscopy is superior to epifluorescence (less rapid GFP bleaching and better signal-to-noise by omitting out-of-focus light), TIRF provides even greater imaging fidelity at video rate speeds (compare Figs. 2B and 2C). Instead of passing the excitation laser through the sample like confocal microscopy, with TIRF the angle of incident light is increased until a critical angle is reached where all the light is reflected from the interface between the higher refractive index glass ($n=1.518$) and lower refractive index aqueous medium ($n=1.33-1.38$). Although no incident light penetrates the sample, it generates an electromagnetic field in the lower refractive index medium, known as the evanescent wave. This TIRF field has the same wavelength as the incident light and decays exponentially as it propagates from the interface, illuminating only the bottom few hundred nanometers of the sample (Axelrod, 2001).

Chlamydomonas is an ideal specimen for TIRF microscopy due to its natural gliding behavior. When *Chlamydomonas* encounters a solid substrate such as the coverglass, it tightly adheres both flagella to the glass, orienting them 180 degrees from each other (Bloodgood, 1977; 1995). Since the flagella are roughly 200nm thick, they fit perfectly within the evanescent field, while the large autofluorescent cell body is excluded from the field of illumination (Fig. 1A). Multiple through-the-objective TIRF systems are commercially available, each equipped with high NA objectives that are capable of producing the increased angles of incident illumination required for TIRF (for the images in Fig. 2, we used a Nikon TE2000-E inverted scope equipped with a 100x/1.49NA TIRF objective, the exceptionally useful Nikon Perfect Focus System, and a cooled Photometrics QuantEM:512SC EMCCD camera with quantitative gain).

By eliminating light pollution from the rest of the sample, TIRF achieves exceptional signal-to-noise, enabling the clear visualization of low abundance proteins, such as BBS4-GFP, that would otherwise be difficult to detect (Fig. 4). We utilized this improved image fidelity to assay the protein content of IFT particles in regenerating *Chlamydomonas* flagella. With TIRF, we managed to quantify not only the speed and frequency of IFT events, but also the GFP intensity of these trafficking IFT particles (Engel *et al.*, 2009). We found that the KAP-GFP and IFT27-GFP intensities of particles in short flagella were several times brighter than particles in long flagella, suggesting that particles in short flagella are assembled from more IFT proteins. We confirmed this disparity in protein content by counting the stepwise GFP bleaching events of particles in

formaldehyde-fixed flagella exposed to TIRF illumination. Because TIRF has exceptional signal detection and slower photobleaching kinetics, many distinct GFP steps can be identified, especially when the bleach intensity plots are enhanced with an edge-preserving filter (Chung and Kennedy, 1991; Leake *et al.*, 2006). Thus, by simply applying TIRF techniques to existing GFP-labeled *Chlamydomonas* strains, we were able to revise the balance-point model of flagellar length control (proposed in Marshall *et al.*, 2001, 2005), concluding that IFT particle size scales inversely with flagellar length.

A clear advantage of fluorescence microscopy (and TIRF in particular) is the ability to follow the traffic of specific GFP-tagged flagellar proteins. While DIC primarily visualizes large, processive anterograde and retrograde particles (Fig. 2A; Kozminski *et al.*, 1993; Iomini *et al.*, 2001; Dentler, 2005), TIRF microscopy of *Chlamydomonas* flagella has revealed different classes of IFT behavior. KAP-GFP, IFT27-GFP, and IFT20-GFP all have large anterograde particles that move with the same frequency and speed as the anterograde particles seen in DIC (Fig. 2A-E). However, while IFT27-GFP has processive retrograde transport similar to particles imaged by DIC (Fig. 2D), IFT20-GFP has slow, thick retrograde traces that frequently pause or change speeds (Figs. 2B and 2C). KAP-GFP, meanwhile, shows very few retrograde traces at all and has much higher background flagellar fluorescence than IFT27-GFP and IFT20-GFP, particularly toward the flagellar tip (Fig. 2E). Thus, the observation of only three GFP-labeled proteins has already begun to reveal several new intricacies of IFT. All three proteins likely travel out to the flagellar tip together at $\sim 2\mu\text{m/s}$, in large

processive anterograde particles that are clearly visible by DIC (Figs. 2F and 2G). At the tip, it is possible that some proteins, including the kinesin-2 anterograde motor and IFT20, which helps link kinesin-2 to IFT complex B, detach from these large particles. While the core of IFT complex B (including IFT27) undergoes processive retrograde transport in a protein complex large enough to be seen by DIC, IFT20 (perhaps bound to neighboring peripheral proteins such as IFT57) appears to undergo slower and less processive transport in complexes that may be too small for DIC visualization. Meanwhile, it is possible that many kinesin-2 proteins do not partake in retrograde transport at all, but rather remain diffuse in the flagellum. This observation potentially conflicts with the model that kinesin-2 is transported out of flagella on retrograde IFT particles powered by cytoplasmic dynein (Signor *et al.*, 1999). It should be noted that the divergent retrograde behaviors of IFT20-GFP and KAP-GFP could be the result of interference from the GFP tags. However, IFT20-GFP and KAP-GFP both fully rescue endogenous protein mutations and both have anterograde transport that is identical to IFT27-GFP and IFT observed by DIC, suggesting that the GFP-labeled proteins function normally. In addition, all three GFP-tagged proteins have reduced retrograde frequencies compared to frequencies that have been reported by DIC (Iomini *et al.*, 2001; Dentler, 2005). This may be due to detection limits of the TIRF technique, or it may present additional evidence that there are several different species of retrograde particles that cannot be distinguished by DIC. Of course, it is of great interest to label other

IFT proteins with GFP to compile a complete description of which proteins share different IFT behaviors.

III. Materials and Methods: Technical Considerations of *Chlamydomonas* TIRF

A. Slide Preparation and Cell Immobilization

Preparing GFP-labeled *Chlamydomonas* cells for observation by TIRF microscopy is straightforward. After growing cells in liquid media, simply plate a small volume (~15 μ L) on untreated coverglass (we use #1.5). Though specially conditioned coverglass may also work, *Chlamydomonas* cells readily adhere to untreated glass. It is necessary to place a spacer between the slide and coverglass (we use a square ring of petroleum jelly) to prevent cells from being crushed. Focusing on the interface between the coverglass and the media should reveal numerous adherent cells whose flagella are perfectly positioned for TIRF microscopy.

While the unique gliding motility of *Chlamydomonas* cells makes TIRF imaging possible, it also poses one of the greatest obstacles to the technique. Although cells often remain in a stationary gliding position for up to a minute, which is ample time to analyze IFT, cells are quite mobile and will either glide out of the field of view or detach from the coverglass altogether. This is further complicated by the phototactic and photophobic behaviors of *Chlamydomonas*. The mere act of observing the cells with TIRF illumination is enough to either encourage cells to flee the field of view or cluster tightly together on the

coverglass, depending on the strain. Mounting cells on an agarose pad is an effective tool for immobilizing *Chlamydomonas* cells for DIC or confocal microscopy. However, agarose pads rarely immobilize cells in a gliding position. Instead, the autofluorescent cell bodies are pressed against the coverglass (and into the TIRF field), while the flagella do not evenly adhere to the glass. Coating the coverglass with poly-lysine has also proved problematic for immobilizing gliding cells. At 0.1 mg/mL, poly-lysine slightly decreases cell motility. At increased concentrations (up to 10 mg/mL), gliding motility nearly stops, but the tips of adherent flagella begin to curl up and cells deflagellate, leaving their flagella behind on the coverglass (Kozminski, 1995b). Additionally, because poly-lysine has a higher refractive index than aqueous media, it can interfere with the propagation of the evanescent wave and cause light scattering and increased background signal (George, 2008). When considering coverglass coatings, it is also important to ensure that the layers are thin so they will not occupy a significant portion of the TIRF field. It is possible that a more specific coating, such as antibodies to the flagellar membrane glycoprotein FMG1 (Bloodgood *et al.*, 1986), might prove more effective. However, even if we could completely immobilize the flagella to a substrate, *Chlamydomonas* may simply shed their flagella as seen with poly-lysine.

We have had greater success by crossing GFP strains to mutants with paralyzed flagella (such as the central-pair mutant *pf18*). While these cells tend to remain adhered to one spot for significantly longer time periods than wild-type cells, ultimately they too glide away or detach. There are additional

Chlamydomonas mutants that may prove useful for immobilizing cells in the gliding position. *ptx* mutants are defective in phototaxis, and thus may not react to the excitation light (Horst and Witman, 1993). Concanavalin A has been reported to interfere with gliding motility in the *L-23 pf18* mutant (Bloodgood and Salomonsky, 1989). There are also a large number of *gli* mutants that were isolated by screening for gliding defects (Kozminski, 1995c), though the identities of these genes remain unknown, which complicates potential crosses to GFP strains. It is also important to note that mutant backgrounds may introduce unexpected variables (for example, *pf18* cells regenerate their flagella with slowed kinetics), and thus should always be compared to wild-type cells. Finally, gliding motility is reportedly inhibited by lowering the free calcium concentration with EGTA and adding 100mM NaCl (Kozminski *et al.*, 1993; Bloodgood, 1995). However, these conditions also induce flagellar resorption through unknown mechanisms (Lefebvre *et al.*, 1978), and consequently are less useful for observing flagella under steady-state length conditions. The immobilization of adherent *Chlamydomonas* cells during TIRF microscopy remains an unresolved issue, and until a solution is found, confocal and DIC microscopy will maintain an advantage for the prolonged observation of single cells.

B. The Angle of Incidence and Depth of the TIRF Field

The depth of the evanescent field varies greatly as a function of the excitation laser's angle of incidence. Greater angles create shallower fields (Mattheyes and Axelrod, 2006), so for most flagellar imaging applications, the

incident angle should be reduced to near the critical angle to ensure the deepest possible TIRF field. By adjusting the angle of incidence very close to the critical angle, we have measured TIRF fields on our microscope that are 250nm-300nm deep (Engel *et al.*, 2009). Even though this is enough to image completely through *Chlamydomonas* flagella, it is very important to note that TIRF illumination is not constant, but rather falls off exponentially as a function of distance from the coverglass (Axelrod, 2001). This property of the evanescent field should always be considered when interpreting results. For example, when comparing IFT particles within a flagellum, it is impossible to distinguish whether differences in intensity are due to unequal protein content or different positions of the particles on the axoneme (Fig. 1B). However, it is legitimate to compare the average intensity of IFT particles between different flagella (as shown in Engel *et al.*, 2009). The relationship between axoneme geometry and the TIRF field also increases the variability of GFP step sizes during quantitative photobleaching of fixed cells. GFP molecules that are further from the coverglass produce less intensity and are also less likely to bleach (Fig. 1B). Thus, although many GFP step sizes are similar, it is not uncommon to see a few smaller steps towards the end of the bleach. Since even slight variations in the incident angle significantly impact GFP intensity and the depth of the evanescent field, motorized control of the laser trajectory is quite useful, especially when trying to be consistent between imaging sessions. Other parameters, such as laser power and camera settings should also be kept constant when attempting to compare intensities between images. Many new EMCCD cameras are equipped with linear gain,

which increases the reliability of comparing intensities between images.

However, gain decreases as EMCCD cameras age (Ingley *et al.*, 2008), so imaging sessions should be performed as close together as possible.

C. GFP Labeling of *Chlamydomonas* Flagellar Proteins

Fluorescence detection is greatly increased if every copy of a specific flagellar protein is labeled with GFP. Furthermore, complete labeling enables quantification of protein abundance via intensity measurements and quantitative photobleaching (Engel *et al.*, 2009). However, since targeted gene deletion and homologous recombination are not simple feats in *Chlamydomonas*, the best candidates for GFP-labeling are IFT genes that already have identified *Chlamydomonas* mutations. These mutants can then be rescued with genes encoding GFP-tagged versions of the proteins. Rescuing IFT mutants provides the additional advantage of demonstrating that the exogenous GFP-labeled protein is functioning correctly. Moreover, when tagged proteins are expressed in the presence of the untagged endogenous protein, the latter may out-compete the former for interaction with a limited number of binding partners (Lechtreck *et al.*, 2009b). The existing GFP-tagged IFT20 and BBS4 strains are in null mutant backgrounds, where all endogenous flagellar protein has been replaced with the labeled version (Fig. 3, Lechtreck *et al.*, 2009a). KAP-GFP was expressed in the temperature-sensitive KAP mutant, *fla3* (Mueller *et al.*, 2005). However, at all temperatures, the flagellar KAP population is almost completely labeled with GFP (minute levels of the endogenous mutant protein may remain, see Fig. 3). IFT27-

GFP, on the other hand, was expressed in wild-type cells. As a result, only half of the flagellar IFT27 protein is GFP-labeled, yielding a much weaker fluorescent signal (compare Fig. 2D with 2C and 2E; Qin *et al.*, 2007).

Two distinct cloning strategies have been successfully employed for GFP-labeling in *Chlamydomonas*: 1) Insertion of the tag sequence into an exon near the 3' end of the target gene (KAP-GFP) and 2) fusion of fluorescent proteins to the C-terminus of the target proteins (IFT27-GFP, CrPKD2-GFP, IFT20-GFP, IFT20-mCherry, BBS4-GFP). Proteins can be expressed either from vectors containing genomic sequences including the endogenous promoters (KAP-GFP, IFT27-GFP, CrPKD2-GFP) or from vectors using the *HSP70B/rbcS* or *FLA14* promoters, the latter of which was used to express cDNAs of *IFT20* and *BBS4*. Because the *FLA14* gene does not contain introns, its promoter efficiently expresses intronless cDNA. Furthermore, since *FLA14* encodes the flagellar dynein light chain LC8 (Pazour *et al.*, 1998), tagged flagellar proteins (such as IFT20-GFP) are expressed by the *FLA14* promoter at relatively wild-type levels and have equal flagellar abundance to endogenous protein in wild-type cells (Fig. 3).

Chlamydomonas cells can be transformed with linearized plasmids using the glass-bead method (Kindle, 1990) or electroporation (Shimogawara *et al.*, 1998). Screening transformants for rescue of a selectable phenotype enables thousands of transformants to be screened and strains expressing fusion proteins to be easily identified. IFT20-GFP, for example, was expressed in an *ift20* deletion mutant, which is immotile due to the lack of flagella. Transformants

were selected for restoration of motility, and expression of the GFP-fusion protein was then verified. If phenotypic selection of cells is not possible, cells expressing the fusion protein may be identified by fluorescence microscopy and western blotting. In our experience, FACS identification of GFP-expressing cells is difficult because the strong autofluorescence of the cell body masks GFP emission, but it may be possible to apply this approach to “white” *Chlamydomonas* mutants (McCarthy *et al.*, 2004).

IV. Discussion: Future Prospects for *Chlamydomonas* TIRF

A. Simultaneous Multi-Color TIRF

Simultaneously observing two or more proteins tagged with different color fluorophores holds great promise for understanding the co-localization of multiple IFT proteins and cargos as they transit through the flagellum. Considering that our initial observations appear to have revealed different classes of retrograde behaviors (Fig. 2), it will be of great interest to visualize which proteins traffic together.

In principle, there are few limitations to labeling numerous flagellar proteins with different fluorophores. Initially, *Chlamydomonas* IFT proteins had only been tagged with codon-optimized GFP because of concerns about protein expression. However, IFT20 fused to a synthetic mCherry sequence optimized for human codon bias was successfully expressed (Fig. 4; Lechtreck *et al.*, 2009a), opening the door to two-color experiments. IFT20-mCherry was observed to be less photostable and half as bright as IFT20-GFP. Initial

observations of cells expressing both IFT20-mCherry and BBS4-GFP revealed that BBS4 is carried by only a subset of anterograde particles (Fig. 4). YFP and CFP variants of codon-optimized GFP have also been expressed in *Chlamydomonas* (Feldman, 2008), providing additional avenues for multi-color imaging.

Simultaneous multi-color TIRF presents several unique hurdles compared to single-channel imaging. In order to cleanly image two colors simultaneously, several specialized pieces of equipment are required, including a multiline laser launch, a multipass dichroic mirror that directs both excitation wavelengths to the sample, and an emission splitter (such as Photometrics Dual-View or Cairn OptoSplit) that separates each emission wavelength to opposite halves of a single camera or two different cameras. (The movie in Fig. 4 was acquired with an Olympus IX71 Inverted Microscope equipped with an Olympus 60x/1.4NA PlanApo objective, a Semrock FF498/581 multipass beam splitter with laser-line filters to clean the two colors of excitation light, a custom-built emission splitter system with a Semrock FF562-Di01 dichroic mirror and Semrock 525/50nm and 630/69nm emission filters that block both excitation wavelengths, and an Andor iXon DV860 back-illuminated EMCCD camera).

Most commercially available TIRF systems use a single fiber-optic cable to deliver multiple laser wavelengths to the sample. These systems can only introduce light at one incident angle and at one focus setting, which creates two complications for multi-color imaging. The first issue to consider is the effect of excitation color on laser focusing. Because different wavelengths of light are

refracted at different angles when passing through the objective, they do not share the same focal point. Unless each laser is independently focused, the beam will be slightly less collimated, leading to increased light scattering and background signal (George, 2008). The second issue to consider is the effect of laser color on the depth of the evanescent field. The depth of field penetration depends on the refractive indices of the coverglass ($n=1.518$) and the aqueous medium ($n=1.33-1.38$), in addition to both the angle and wavelength of the incident illumination (Axelrod, 2001; George, 2008). Since the refractive indices of the imaging setup are relatively fixed, the angle of incidence must be adjusted for different excitation wavelengths to maintain the same depth and intensity of TIRF illumination. Even with motorized control of laser trajectory, tuning the incident angle when switching between excitation colors introduces too great a lag for the simultaneous imaging of fast-moving IFT particles. While neither of these wavelength-related effects is severe, simultaneous multi-color TIRF would benefit from an imaging setup with separate light paths for each laser, each with its own independent angle and focus adjustments.

B. FRAP, Photoactivation, and Photoconversion

Several advanced photobleaching and photoactivation techniques can be combined with TIRF to shed light on additional aspects of IFT. Measuring the kinetics of FRAP (fluorescence recovery after photobleaching) may yield insights into how readily different IFT proteins in the flagella exchange with the cytoplasm. Tagging IFT proteins with photoactivatable or photoconvertible

fluorophores would provide a reciprocal approach to this question.

Photoactivation in the cytoplasm would facilitate the observation of protein exchange into the flagella. Because *Chlamydomonas* is biflagellate, photoactivating within one flagellum would also be highly informative. Protein exchange could be judged not only by loss of fluorescent IFT particles within the photoactivated flagellum, but also by the appearance of fluorescence in the dark flagellum. Finally, photoactivation and photoconversion would provide useful tools for understanding the dynamics of IFT turnaround at the flagellar tip. By only activating a small subset of the IFT particles in a flagellum, it would become clear whether particles immediately undergo retrograde transport when they reach the tip, and whether retrograde KAP (Fig. 2E) truly is diffuse or whether it undergoes an active transport mechanism that is undetectable in fully-labeled KAP-GFP flagella.

One potential obstacle to these promising experiments is the expression of photoactivatable and photoconvertible proteins in *Chlamydomonas*. The design of photoactivatable GFP (PA-GFP) should only require the straight-forward task of making a few simple base pair changes to the codon-optimized GFP sequence (following the scheme outlined by Patterson and Lippincott-Schwartz, 2002). The expression of more exotic fluorophores, such as the green-to-red photoconvertible proteins Kaede (Ando *et al.*, 2002), EosFP (Wiedenmann *et al.*, 2004), and Dendra2 (Labas *et al.*, 2002; Adam *et al.*, 2009), and the reversibly photoswitchable Dronpa (Habuchi *et al.*, 2005) may require codon optimization.

However, it is possible that, like mCherry, these proteins will express without alterations to their sequence.

The greatest challenge to performing FRAP or photoactivation in TIRF will probably be the immobilization of *Chlamydomonas* cells. As previously discussed, even paralyzed strains glide out of the field of view or detach from the coverglass within minutes. It is likely that *Chlamydomonas* will have a strong photophobic response to the intense laser energy required for FRAP.

Furthermore, the phototropin blue-light receptors localized in *Chlamydomonas* flagella (Huang *et al.*, 2004) will certainly be stimulated by the 405nm light used to activate PA-GFP, though the function of these photoreceptors is unknown. It is possible that a combination of the strategies discussed in section IIIA (such as *ptx* mutants and calcium depletion) will immobilize adherent cells long enough to facilitate these powerful protein tracking techniques. For some questions, such as protein exchange between the flagellar and cytoplasmic pools, confocal microscopy should suffice, allowing immobilization on agarose pads.

C. Applications Beyond IFT

TIRF should prove equally beneficial to imaging other *Chlamydomonas* flagellar proteins that are not continuously trafficked by IFT. This includes monitoring the dynamics of membrane-bound signaling proteins, such as CrPKD2-GFP (Huang *et al.*, 2007) and tracking changes in flagellar membrane glycoprotein distribution (Bloodgood *et al.*, 1986). FRAP is not limited to studying the exchange of IFT particles, but can also be used to examine the turnover of

membrane proteins and integrated axonemal proteins, such as dynein arms (Watanabe *et al.*, 2004). Based on the incorporation of HA-tubulin in quadraflagellates, it had been concluded that axonemal tubulin does not treadmill (Marshall *et al.*, 2001). However, this hypothesis could be tested more elegantly in live cells by either speckling axonemal tubulin with GFP (Waterman-Storer and Danuser, 2002) or by bleaching a fiducial mark on a fluorescent axoneme and monitoring this mark for movement. In another novel use of the technique, TIRF was recently combined with calcium-responsive dyes to measure transient spikes in flagellar calcium concentration. These transient calcium spikes rapidly increased in frequency prior to deflagellation (Wheeler *et al.*, 2008). Clearly, TIRF microscopy of *Chlamydomonas* flagella holds great promise for a range of applications beyond the study of IFT.

V. Summary

TIRF microscopy is a versatile new method for observing fluorescence in *Chlamydomonas* flagella. While there are still a few technical hurdles, such as protein expression and cell immobilization, TIRF provides greatly improved fidelity for imaging flagellar proteins in live cells. It has already provided some glimpses of new IFT behaviors (Fig. 2), but a wealth of untapped potential remains. Substantial inquiries into the mechanisms of IFT, as well as a full gamut of other flagellar biology questions, are waiting to be explored through additional protein labeling and the incorporation of multi-color, FRAP, and photoactivation techniques. Perhaps in the more distant future, it may even be

possible to combine TIRF of *Chlamydomonas* flagella with super resolution technologies such as PALM/STORM (Betzig *et al.*, 2006; Rust *et al.*, 2006) and Structured Illumination (Gustafsson, 2000).

Acknowledgements

We thank Kurt Thorn and the Nikon Imaging Center at UC San Francisco and Mitsuo Ikebe and Tsuyoshi Sakai in the Department of Physiology at the University of Massachusetts Medical School for invaluable microscopy resources and assistance. We also thank Joshua Mueller, Mary Porter, Hongmin Qin, and Joel Rosenbaum for generously sharing GFP-labeled strains, as well as Kurt Thorn, Arthur Millius, Sarah Goodwin, Jennifer Blake and the Marshall Lab for helpful discussions and careful reading of the manuscript. This work was supported by the W. M. Keck Foundation Distinguished Young Scholars Program (W. F. Marshall), the Searle Scholar Program (W. F. Marshall), the Genentech Graduate Fellowship (B. D. Engel), National Institutes of Health Grant GM 030626 (G. B. Witman), and the Robert W. Booth Fund at the Greater Worcester Community Foundation (G. B. Witman).

Figure Legends

Figure 1. *Chlamy* TIRF Imaging Setup and the Effect of Axoneme Geometry on GFP Fluorescence. (A) Imaging of *Chlamydomonas* via through-the-objective TIRF. Excitation light comes out of the objective at an incident angle that is greater than the critical angle. The light is totally internally reflected, creating an evanescent field on the other side of the interface. Both flagella adhere to the coverglass and are readily imaged, while the cell body remains outside of the TIRF field. (B) Due to the ~200nm diameter of the axoneme, GFP molecules near the glass interface will be brighter and more likely to photobleach, while GFP proteins on the far side of the axoneme will produce a weaker signal, but are also less likely to bleach. This effect of the flagellar geometry should be considered during both live-cell imaging and fixed-cell quantitative photobleaching experiments.

Figure 2. Comparison of DIC, Spinning Disk Confocal, and TIRF Microscopy and Summary of Current IFT Observations via TIRF. For all kymographs, the X-axis represents distance (base of flagellum on the left, tip on the right), while the Y-axis is time. Vertical scale bars: 2 sec; horizontal scale bars: 2 μm . (A) DIC kymograph of KAP-GFP *fla3*. Anterograde and retrograde traces are processive. Acquired at intermediate resolution with an .85NA dry condenser. For higher quality DIC kymographs of IFT (taken with 1.4NA oil condensers), see Iomini *et al.*, 2001 and Dentler, 2005. (B) Spinning disk kymograph of IFT20-GFP Δ *ift20*. Compare fidelity with the TIRF kymograph of

IFT20-GFP $\Delta ift20$ in (C). Anterograde is processive, but retrograde has broad, slow traces that pause and change speed. (D) TIRF kymograph of IFT27-GFP in a wild-type background. Anterograde and retrograde traces are processive, similar to DIC. (E) TIRF kymograph of KAP-GFP *fla3*. Anterograde is processive but there are very few retrograde traces and the flagellar background is higher than IFT20-GFP or IFT27-GFP, especially towards the flagellar tip. Compare to the processive retrograde in the DIC kymograph in part A. (F) A hypothetical anterograde particle. The three GFP-labeled IFT proteins are color-coded to match part G. (G) An illustrated kymograph that summarizes the behaviors of all three proteins seen in parts C, D, and E.

Figure 3. Protein Abundance in the Flagella of Wild-type and GFP-tagged Strains. Top panel: KAP-GFP *fla3* flagella almost exclusively contain KAP-GFP protein (though a small amount of endogenous protein remains). KAP-GFP levels are similar to endogenous KAP levels in wild-type and IFT20-GFP flagella. Middle panel: IFT20-GFP flagella only contain exogenous protein because the fusion protein was expressed in a null *ift20* background. IFT20-GFP levels are similar to endogenous IFT20 levels in wild-type and KAP-GFP flagella. Bottom panel: the expression of exogenous KAP-GFP and IFT20-GFP does not interfere with the flagellar levels of IFT172 (part of IFT complex B), IFT139 (part of IFT complex A), or IC69 (an intermediate chain of axonemal outer arm dynein). The top panel was probed with anti-KAP, the middle panel was probed with anti-

IFT20, and the bottom panel was probed with anti-IFT172, anti-IFT139 and anti-IC69 antibodies.

Figure 4. *Simultaneous Two-Color TIRF of IFT20-mCherry and BBS4-GFP.*

For all kymographs, the X-axis represents distance (base of flagellum on the left, tip on the right), while the Y-axis is time. Vertical scale bar: 2 sec; horizontal scale bar: 2 μm . BBS4-GFP is much lower in abundance than IFT20-mCherry, and is only localized to a subset of the IFT20-mCherry particles. In the merged image, BBS4-GFP is green and IFT20-mCherry is red. Please see the color version of this kymograph online.

Supplementary Videos

Video 1. *TIRF microscopy of IFT20-GFP in Chlamydomonas flagellum.*

Bright anterograde and retrograde particles are clearly visible (from Fig. 2C). 29 seconds, 24fps.

Video 2. *TIRF microscopy of IFT27-GFP in Chlamydomonas flagellum.*

Anterograde and retrograde particles are clearly visible. Notice that the signal is greatly reduced compared to IFT20-GFP because only half the flagellar IFT27 is tagged with GFP (from Fig. 2D). 23 seconds, 30fps.

Video 3. *TIRF microscopy of KAP-GFP in Chlamydomonas flagellum.*

Flagellar background fluorescence is higher than IFT20-GFP and IFT27-GFP and only anterograde particles are clearly visible (from Fig 2E). 29 seconds, 26fps.

Video 4. *Simultaneous Two-Color TIRF microscopy of IFT20-mCherry and BBS4-GFP in Chlamydomonas flagellum.*

IFT20-mCherry (red) and BBS4-GFP (green) traffic together on IFT particles (from Fig. 4). 5 seconds, 30fps.

References

- Absalon, S., Blisnick, T., Kohl, L., Toutirais, G., Doré, G., Julkowska, D., Tavenet, A., and Bastin, P. (2008). Intraflagellar transport and functional analysis of genes required for flagellum formation in trypanosomes. *Mol. Biol. Cell* **19**, 929-944.
- Adam, V., Nienhaus, K., Bourgeois, D., and Nienhaus, G. U. (2009). Structural basis of enhanced photoconversion yield in GFP-like protein Dendra2. *Biochemistry* [Apr 16, Epub ahead of print]
- Ando, R., Hama, H., Yamamoto-Hino, M., Mizuno, H., and Miyawaki, A. (2002). An optical marker based on the UV-induced green-to-red photoconversion of a fluorescent protein. *Proc. Natl. Acad. Sci. U.S.A.* **99**, 12651-12656.
- Axelrod, D. (2001). Total internal reflection fluorescence microscopy in cell biology. *Traffic* **2**, 764-774.
- Bisgrove, B. W., and Yost, H. J. (2006). The roles of cilia in developmental disorders and disease. *Development* **133**, 4131-4143.
- Blacque, O. E., Li, C., Inglis, P. N., Esmail, M. A., Ou, G., Mah, A. K., Baillie, D. L., Scholey, J. M., and Leroux, M. R. (2006). The WD repeat-containing protein IFTA-1 is required for retrograde intraflagellar transport. *Mol. Biol. Cell*. **17**, 5053-5062.
- Betzig, E., Patterson, G. H., Sougrat, R., Lindwasser, O. W., Olenych, S., Bonifacino, J. S., Davidson, M. W., Lippincott-Schwartz, J., and Hess, H. F. (2006). Imaging intracellular fluorescent proteins at nanometer resolution. *Science* **313**, 1642-1645.
- Bloodgood, R. A. (1977). Motility occurring in association with the surface of the *Chlamydomonas* flagellum. *J. Cell Biol.* **75**, 983-989.
- Bloodgood, R. A. (1995). Flagellar surface motility: gliding and microsphere movements. In "Methods in Cell Biology" (W. Dentler and G. B. Witman, Ed.), Vol. 47, pp. 273-279. Elsevier Inc., San Diego.
- Bloodgood, R. A., and Salomonsky, N. L. (1989). Use of a novel *Chlamydomonas* mutant to demonstrate that flagellar glycoprotein movements are necessary for the expression of gliding motility. *Cell Motil. Cytoskeleton* **13**, 1-8.
- Bloodgood, R. A., Woodward, M. P., and Salomonsky, N. L. (1986). Redistribution and shedding of flagellar membrane glycoproteins visualized using an anti-carbohydrate monoclonal antibody and concanavalin A. *J. Cell Biol.* **102**, 1797-1812.
- Chung, S. H., and Kennedy, R. A. (1991). Forward-backward non-linear filtering technique for extracting small biological signals from noise. *J. Neurosci. Methods* **40**, 71-86.
- Cole, D. G., Diener, D. R., Himelblau, A. L., Beech, P. L., Fuster, J. C., and Rosenbaum, J. L. (1998). *Chlamydomonas* kinesin-II-dependent intraflagellar transport (IFT): IFT particles contain proteins required for ciliary assembly in *Caenorhabditis elegans* sensory neurons. *J. Cell Biol.* **141**, 993-1008.
- Dentler, W. (2005). Intraflagellar transport (IFT) during assembly and disassembly of *Chlamydomonas* flagella. *J. Cell Biol.* **170**, 649-659.

Engel, B. D., Ludington, W. B., and Marshall, W. F. (2009). Intraflagellar transport particle size scales inversely with flagellar length: revisiting the balance-point length control model. *J. Cell Biol.* **[In review]**

Feldman, J. L. (2008). Deconstructing Cell Architecture: Exploring centriole structure, function, and positioning in the green alga *Chlamydomonas reinhardtii*. *Ph.D. Thesis*. University of California, San Francisco.

Follit, J. A., Tuft, R. A., Fogarty, K. E., and Pazour, G. J. (2006). The intraflagellar transport protein IFT20 is associated with the Golgi complex and is required for cilia assembly. *Mol. Biol. Cell* **17**, 3781-3792.

Fuhrmann, M., Oertel, W., and Hegemann, P. (1999). A synthetic gene coding for the green fluorescent protein (GFP) is a versatile reporter in *Chlamydomonas reinhardtii*. *Plant J.* **19**, 353-361.

George, N. B. (2008). Overcoming optical challenges to live-cell TIRF microscopy. *Biophotonics* **15**, 30-33.

Gustafsson, M. G. (2000). Surpassing the lateral resolution limit by a factor of two using structured illumination microscopy. *J. Microsc.* **198**, 82-87.

Habuchi, S., Ando, R., Dedecker, P., Verheijen, W., Mizuno, H., Miyawaki, A., and Hofkens, J. (2005). Reversible single-molecule photoswitching in the GFP-like fluorescent protein Dronpa. *Proc. Natl. Acad. Sci. U.S.A.* **102**, 9511-9516.

Heitzer, M., Eckert, A., Fuhrmann, M., and Griesbeck, C. (2007). Influence of codon bias on the expression of foreign genes in microalgae. *Adv. Exp. Med. Biol.* **616**, 46-53.

Horst, C. J., and Witman, G. B. (1993). ptx1, a nonphototactic mutant of *Chlamydomonas*, lacks control of flagellar dominance. *J. Cell Biol.* **120**, 733-741.

Hou, Y., Qin, H., Follit, J. A., Pazour, G. J., Rosenbaum, J. L., and Witman, G. B. (2007). Functional analysis of an individual IFT protein: IFT46 is required for transport of outer dynein arms into flagella. *J. Cell Biol.* **176**, 653-665.

Huang, B., Rifkin, M. R., and Luck, D. J. (1977). Temperature-sensitive mutations affecting flagellar assembly and function in *Chlamydomonas reinhardtii*. *J. Cell Biol.* **72**, 67-85.

Huang, K., Diener, D. R., Mitchell, A., Pazour, G. J., Witman, G. B., and Rosenbaum, J. L. (2007). Function and dynamics of PKD2 in *Chlamydomonas reinhardtii* flagella. *J. Cell Biol.* **179**, 501-514.

Huang, K., Kunkel, T., and Beck, C. F. (2004). Localization of the blue-light receptor phototropin to the flagella of the green alga *Chlamydomonas reinhardtii*. *Mol. Biol. Cell* **15**, 3605-3614.

Huangfu, D., Liu, A., Rakeman, A. S., Murcia, N. S., Niswander, L., and Anderson, K. V. (2003). Hedgehog signalling in the mouse requires intraflagellar transport proteins. *Nature* **426**, 83-87.

Ingley, R., Smith, D. R., and Holland, A. D. (2008). Life testing of EMCCD gain characteristics. *Nucl. Instrum. Methods Phys. Res., Sect. A* **600**, 460-465.

Iomini, C., Babaev-Khaimov, V., Sassaroli, M., and Piperno, G. (2001). Protein particles in *Chlamydomonas* flagella undergo a transport cycle consisting of four phases. *J. Cell Biol.* **153**, 13-24.

- Kamiya, R. (1982). Extrusion and rotation of the central-pair microtubules in detergent-treated *Chlamydomonas* flagella. *Prog. Clin. Biol. Res.* **80**, 169-173.
- Kindle, K. L. (1990). High-frequency nuclear transformation of *Chlamydomonas reinhardtii*. *Proc. Natl. Acad. Sci. U.S.A.* **87**, 1228-1232.
- King, S. M. (1995). Large-scale isolation of *Chlamydomonas* flagella. In "Methods in Cell Biology" (W. Dentler and G. B. Witman, Ed.), Vol. 47, pp. 9-12. Elsevier Inc., San Diego.
- Kozminski, K. G. (1995)c. Beat-independent flagellar motilities in *Chlamydomonas* and an analysis of the function of alpha-tubulin acetylation. *Ph.D. Thesis*. Yale University.
- Kozminski, K. G. (1995)b. High-resolution imaging of flagella. In "Methods in Cell Biology" (W. Dentler and G. B. Witman, Ed.), Vol. 47, pp. 263-271. Elsevier Inc., San Diego.
- Kozminski, K. G., Beech, P. L., and Rosenbaum, J. L. (1995)a. The *Chlamydomonas* kinesin-like protein FLA10 is involved in motility associated with the flagellar membrane. *J. Cell Biol.* **131**, 1517-1527.
- Kozminski, K. G., Johnson, K. A., Forscher, P., and Rosenbaum, J. L. (1993). A motility in the eukaryotic flagellum unrelated to flagellar beating. *Proc. Natl. Acad. Sci. U.S.A.* **90**, 5519-5523.
- Labas, Y. A., Gurskaya, N. G., Yanushevich, Y. G., Fradkov, A. F., Lukyanov, K. A., Lukyanov, S. A., and Matz, M. V. (2002). Diversity and evolution of the green fluorescent protein family. *Proc. Natl. Acad. Sci. U.S.A.* **99**, 4256-4261.
- Leake, M. C., Chandler, J. H., Wadhams, G. H., Bai, F., Berry, R. M., and Armitage, J. P. (2006). Stoichiometry and turnover in single, functioning membrane protein complexes. *Nature* **443**, 355-358.
- Lehtreck, K. F., Delmotte, P., Robinson, M. L., Sanderson, M. J., and Witman, G. B. (2008). Mutations in Hydin impair ciliary motility in mice. *J. Cell Biol.* **180**, 633-643.
- Lehtreck, K. F., Johnson, E. C., Sakai, T., Ikebe, M., and Witman, G. B. (2009)a. The *Chlamydomonas* BBSome is transported by a subset of IFT particles and *bbs* mutants abnormally accumulate flagellar signaling proteins. *J. Cell Biol.* **187**, 1117-1132.
- Lehtreck, K. F., Luro, S., Awata, J., and Witman, G. B. (2009)b. HA-tagging of putative flagellar proteins in *Chlamydomonas reinhardtii* identifies a novel protein of intraflagellar transport complex B. *Cell Motil. Cytoskeleton.* **66**, 469-482.
- Lefebvre, P. A. (1995). Flagellar amputation and regeneration in *Chlamydomonas*. In "Methods in Cell Biology" (W. Dentler and G. B. Witman, Ed.), Vol. 47, pp. 3-7. Elsevier Inc., San Diego.
- Lefebvre, P. A., Nordstrom, S. A., Moulder, J. E., and Rosenbaum, J. L. (1978). Flagellar elongation and shortening in *Chlamydomonas*. IV. Effects of flagellar detachment, regeneration, and resorption on the induction of flagellar protein synthesis. *J. Cell Biol.* **78**, 8-27.
- Marshall, W. F., and Rosenbaum, J. L. (2001). Intraflagellar transport balances continuous turnover of outer doublet microtubules: implications for flagellar length control. *J. Cell Biol.* **155**, 405-414.
- Marshall, W. F., Qin, H., Rodrigo Brenni, M., and Rosenbaum, J. L. (2005). Flagellar length control system: testing a simple model based on intraflagellar transport and turnover. *Mol. Biol. Cell* **16**, 270-278.

- Mattheyses, A. L., and Axelrod, D. (2006). Direct measurement of the evanescent field profile produced by objective-based total internal reflection fluorescence. *J. Biomed. Opt.* **11**, 014006.
- McCarthy, S. S., Kobayashi, M. C., and Niyogi, K. K. (2004). White mutants of *Chlamydomonas reinhardtii* are defective in phytoene synthase. *Genetics* **168**, 1249-57.
- Mueller, J., Perrone, C. A., Bower, R., Cole, D. G., and Porter, M. E. (2005). The FLA3 KAP subunit is required for localization of kinesin-2 to the site of flagellar assembly and processive anterograde intraflagellar transport. *Mol. Biol. Cell* **16**, 1341-1354.
- Mukhopadhyay, S., Lu, Y., Qin, H., Lanjuin, A., Shaham, S., and Sengupta, P. (2007). Distinct IFT mechanisms contribute to the generation of ciliary structural diversity in *C. elegans*. *EMBO J.* **26**, 2966-2980.
- Orozco, J. T., Wedaman, K. P., Signor, D., Brown, H., Rose, L., and Scholey, J. M. (1999). Movement of motor and cargo along cilia. *Nature* **398**, 674.
- Ou, G., Blacque, O. E., Snow, J. J., Leroux, M. R., and Scholey, J. M. (2005). Functional coordination of intraflagellar transport motors. *Nature* **436**, 583-587.
- Patterson, G. H., and Lippincott-Schwartz, J. (2002). A photoactivatable GFP for selective photolabeling of proteins and cells. *Science* **297**, 1873-1877.
- Pazour, G. J., Dickert, B. L., Vucica, Y., Seeley, E. S., Rosenbaum, J. L., Witman, G. B., and Cole, D. G. (2000). *Chlamydomonas* IFT88 and its mouse homologue, polycystic kidney disease gene *tg737*, are required for assembly of cilia and flagella. *J. Cell Biol.* **151**, 709-718.
- Pazour, G. J., and Rosenbaum, J. L. (2002). Intraflagellar transport and cilia-dependent diseases. *Trends Cell Biol.* **12**, 551-555.
- Pigino, G., Geimer, S., Lanzavecchia, S., Paccagnini, E., Cantele, F., Rosenbaum, J. L., and Lupetti, P. (2007). Electron tomographic analysis of intraflagellar transport complexes in situ. *Mol. Biol. Cell* **18**(suppl), abstract 272.
- Piperno, G., and Mead, K. (1997). Transport of a novel complex in the cytoplasmic matrix of *Chlamydomonas* flagella. *Proc. Natl. Acad. Sci. U.S.A.* **94**, 4457-4462.
- Piperno, G., Siuda, E., Henderson, S., Segil, M., Vaananen, H., and Sassaroli, M. (1998). Distinct mutants of retrograde intraflagellar transport (IFT) share similar morphological and molecular defects. *J. Cell Biol.* **143**, 1591-1601.
- Qin, H., Diener, D. R., Geimer, S., Cole, D. G., and Rosenbaum, J. L. (2004). Intraflagellar transport (IFT) cargo: IFT transports flagellar precursors to the tip and turnover products to the cell body. *J. Cell Biol.* **164**, 255-266.
- Qin, H., Wang, Z., Diener, D., and Rosenbaum, J. L. (2007). Intraflagellar transport protein 27 is a small G protein involved in cell-cycle control. *Curr. Biol.* **17**, 193-202.
- Rosenbaum, J. L., Moulder, J. E., and Ringo, D. L. (1969). Flagellar elongation and shortening in *Chlamydomonas*. The use of cycloheximide and colchicine to study the synthesis and assembly of flagellar proteins. *J. Cell Biol.* **41**, 600-619.
- Rust, M. J., Bates, M., and Zhuang, X. (2006). Sub-diffraction-limit imaging by stochastic optical reconstruction microscopy (STORM). *Nat. Methods* **3**, 793-795.

Schneider, L., Clement, C. A., Teilmann, S. C., Pazour, G. J., Hoffmann, E. K., Satir, P., and Christensen, S. T. (2005). PDGFRalpha signaling is regulated through the primary cilium in fibroblasts. *Curr Biol.* **15**, 1861-1866.

Shimogawara, K., Fujiwara, S., Grossman, A., and Usuda, H. (1998). High-efficiency transformation of *Chlamydomonas reinhardtii* by electroporation. *Genetics* **148**, 1821-1828.

Signor, D., Wedaman, K. P., Orozco, J. T., Dwyer, N. D., Bargmann, C. I., Rose, L. S., and Scholey, J. M. (1999). Role of a class DHC1b dynein in retrograde transport of IFT motors and IFT raft particles along cilia, but not dendrites, in chemosensory neurons of living *Caenorhabditis elegans*. *J. Cell Biol.* **147**, 519-530.

Singla, V., and Reiter, J. F. (2006). The primary cilium as the cell's antenna: signaling at a sensory organelle. *Science* **313**, 629-633.

Snow, J. J., Ou, G., Gunnarson, A. L., Walker, M. R., Zhou, H. M., Brust-Mascher, I., and Scholey, J. M. (2004). Two anterograde intraflagellar transport motors cooperate to build sensory cilia on *C. elegans* neurons. *Nat. Cell Biol.* **6**, 1109-1113.

Walther, Z., Vashishtha, M., and Hall, J. L. (1994). The *Chlamydomonas* FLA10 gene encodes a novel kinesin-homologous protein. *J. Cell Biol.* **126**, 175-188.

Watanabe, Y., Hayashi, M., Yagi, T., and Kamiya, R. (2004). Turnover of actin in *Chlamydomonas* flagella detected by fluorescence recovery after photobleaching (FRAP). *Cell Struct. Funct.* **29**, 67-72.

Waterman-Storer, C. M., and Danuser, G. (2002). New directions for fluorescent speckle microscopy. *Curr. Biol.* **12**, R633-640.

Wheeler, G. L., Joint, I., and Brownlee, C. (2008). Rapid spatiotemporal patterning of cytosolic Ca²⁺ underlies flagellar excision in *Chlamydomonas reinhardtii*. *Plant J.* **53**, 401-413.

Wiedenmann, J., Ivanchenko, S., Oswald, F., Schmitt, F., Röcker, C., Salih, A., Spindler, K. D., and Nienhaus, G. U. (2004). EosFP, a fluorescent marker protein with UV-inducible green-to-red fluorescence conversion. *Proc. Natl. Acad. Sci. U.S.A.* **101**, 15905-15910.

Figure 2.1

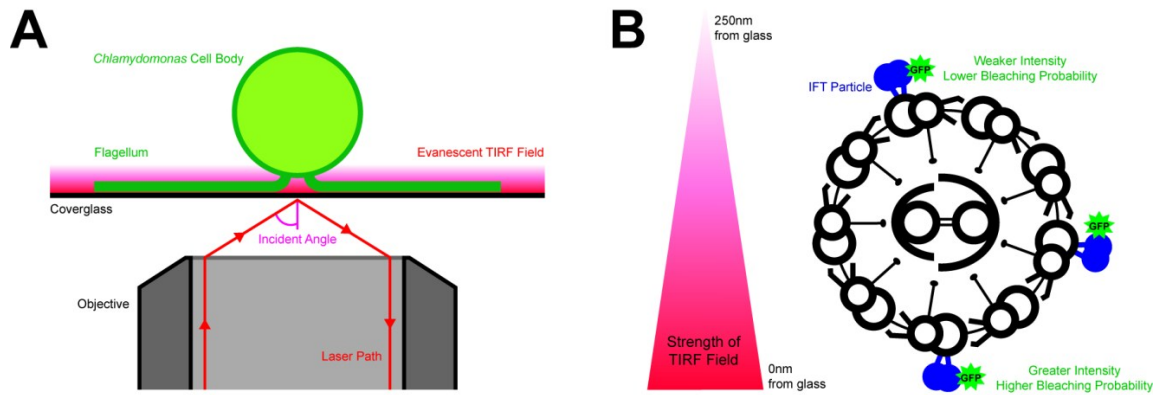


Figure 2.2

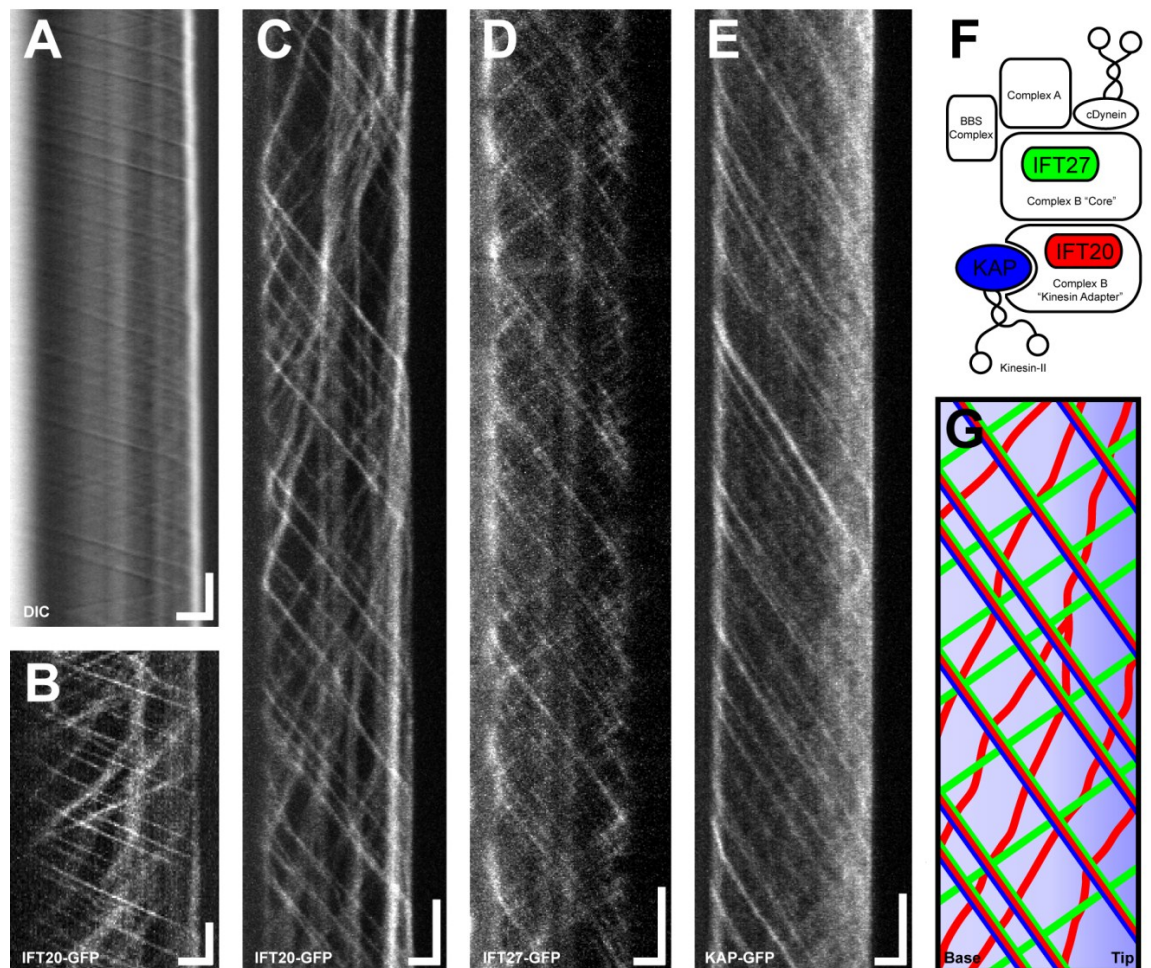


Figure 2.3

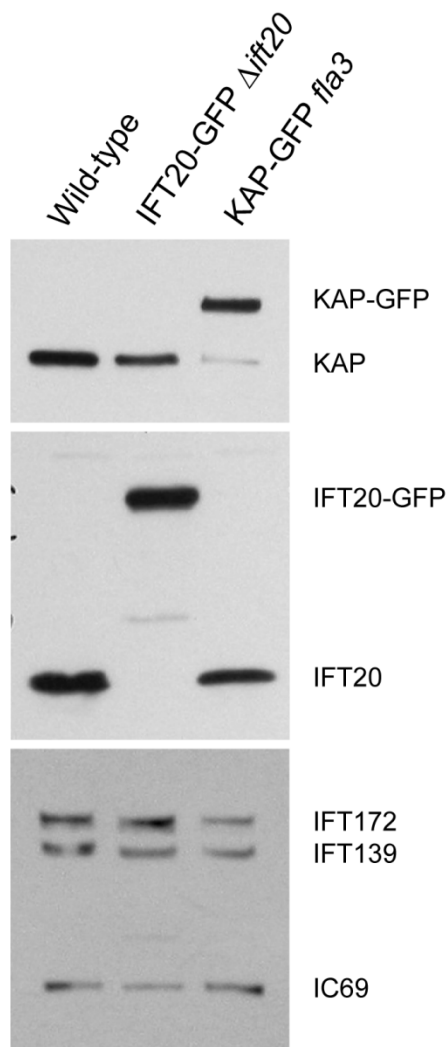
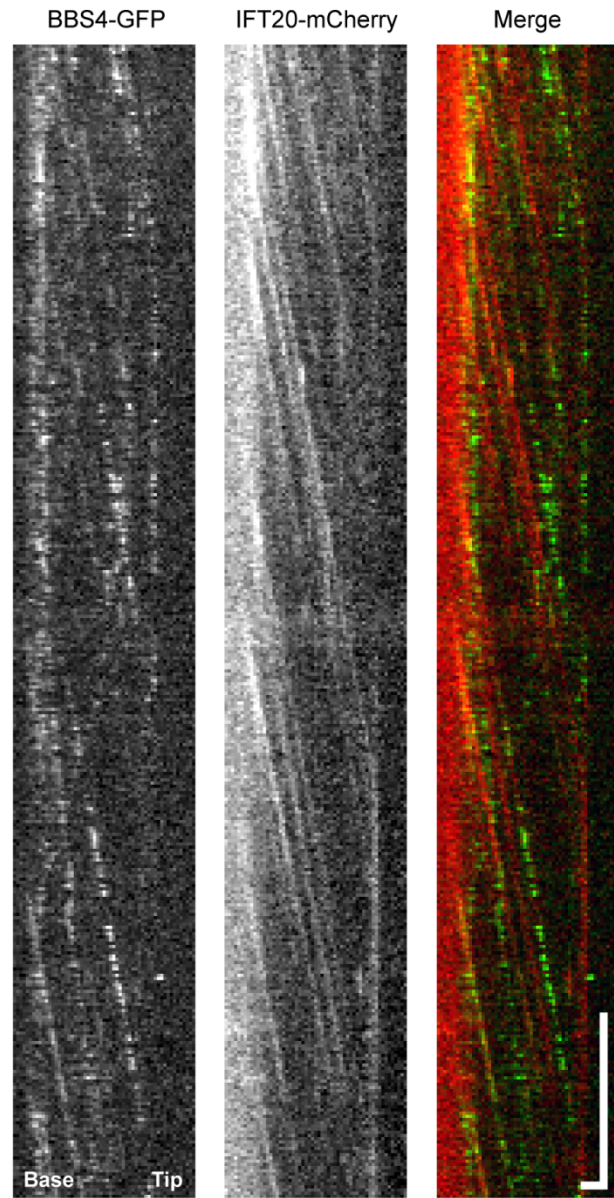


Figure 2.4



Chapter 3

A Cell-based Screen for Inhibitors of Flagella-driven Motility in *Chlamydomonas* Reveals a Novel Modulator of Ciliary Length and Retrograde Actin Flow

Benjamin D. Engel¹, Hiroaki Ishikawa¹, Jessica L. Feldman¹, Christopher W. Wilson², Pao-Tien Chuang², June Snedecor³, Janice Williams³, Zhaoxia Sun⁴, & Wallace F. Marshall¹

1. Dept. of Biochemistry & Biophysics, UCSF
2. Cardiovascular Research Institute, UCSF
3. Small Molecule Discovery Center, UCSF
4. Dept. of Genetics, Yale University School of Medicine

Originally published in *Cytoskeleton*, 68:188-203, March 2011.

Abstract

Cilia are motile and sensory organelles with critical roles in physiology. Ciliary defects can cause numerous human disease symptoms including polycystic kidneys, hydrocephalus, and retinal degeneration. Despite the importance of these organelles, their assembly and function is not fully understood. The unicellular green alga *Chlamydomonas reinhardtii* has many advantages as a model system for studies of ciliary assembly and function. Here we describe our initial efforts to build a chemical-biology toolkit to augment the genetic tools available for studying cilia in this organism, with the goal of being able to reversibly perturb ciliary function on a rapid time-scale compared to that available with traditional genetic methods. We screened a set of 5520 compounds from which we identified four candidate compounds with reproducible effects on flagella at non-toxic doses. Three of these compounds resulted in flagellar paralysis and one induced flagellar shortening in a reversible and dose-dependent fashion, accompanied by a reduction in the speed of intraflagellar transport. This latter compound also reduced the length of cilia in mammalian cells, hence we named the compound “ciliabrevin” due to its ability to shorten cilia. This compound also robustly and reversibly inhibited microtubule movement and retrograde actin flow in *Drosophila* S2 cells. Ciliabrevin may prove especially useful for the study of retrograde actin flow at the leading edge of cells, as it slows the retrograde flow in a tunable dose-dependent fashion until flow completely stops at high concentrations, and these effects are quickly reversed upon washout of the drug.

Introduction

Cilia and flagella are motile and sensory organelles found in most cells of the body (Sloboda and Rosenbaum 2007; Satir et al., 2010). Defects in cilia underlie a diverse set of human diseases known collectively as the ciliopathies, including Polycystic Kidney Disease, Immotile Cilia Syndrome, Joubert Syndrome, Meckel Syndrome, and Bardet-Biedl syndrome (Afzelius, 2004; Badano et al., 2006; Fliegauf et al., 2007; Marshall 2008). There is currently an outstanding need for pharmacological treatments for these diseases. Cilia and flagella, names that can be used interchangeably, are composed of nine microtubule doublets surrounded by a specialized membrane. Although the protein components of cilia have been enumerated in recent years (Pazour et al., 2005; Inglis et al., 2006; Gherman et al., 2006), the molecular pathways that coordinate the assembly and function of this complex organelle remain poorly understood and are currently a topic of intense investigation (Pedersen et al., 2008; Santos and Reiter, 2008). Most analyses of cilia thus far have relied on genetics, imaging, or biochemical approaches. A chemical biology approach, using small molecule modulators of ciliary assembly or function, would provide an orthogonal set of tools for probing ciliary biology. As the use of small molecule inhibitors is a well established strategy for studying the cytoskeleton (Peterson and Mitchison, 2002), we decided to extend this strategy to cilia. One major advantage of a chemical approach compared to genetics is that a much higher degree of temporal control can be attained than with conditional mutations. Such an approach, however, requires a toolbox of small molecules

affecting cilia. While a few such compounds have been found in tests of functionally pre-selected molecules (Nakamura et al., 1987; Tuxhorn et al., 1998; Wilson and Lefebvre, 2004; Ou et al., 2009; Besschetnova et al., 2010), and in an assay for modulators of hedgehog signaling (Hyman, 2009), a systematic search for compounds targeting cilia using direct assays for ciliary assembly or function has not been reported.

Molecules targeting cilia would not only provide useful tools for basic studies of ciliary biology, but could also serve as starting points for pharmacological treatments of cilia-related diseases (Afzelius, 2004). Moreover, several types of tumors rely on hedgehog signaling and can be treated by hedgehog signaling inhibitors (Low and de Sauvage, 2010). Since cilia are required for hedgehog signaling (Huangfu and Anderson, 2005), inhibitors of ciliogenesis may be useful as chemotherapeutic agents for hedgehog-dependent tumors. We expect that cilia would make good drug targets, since they protrude into the extracellular environment where they are directly exposed to dissolved compounds, they lack export pumps and detoxifying enzymes found in the cell body (Pazour et al., 2005), and they contain numerous druggable targets including kinases and channels (Beck and Uhl, 1994; Berman et al., 2003; Pan and Snell, 2004; Qin et al., 2005; Wang et al., 2006; Qin et al., 2007). Moreover, many ciliated tissues in the human body are physically accessible to direct forms of drug delivery, for example via injection into the retina (Gaudana et al., 2010) or aerosol-mediated delivery to the airway (Kleinstreuer et al., 2008). Hence, the pharmacodynamic barriers to treatment of ciliopathies affecting these tissues may

be lower than many other human diseases that involve deep internal tissues or organs. In order to begin exploring chemical strategies, we need to implement high throughput screens for compounds targeting cilia. One approach is to use mammalian culture cells and employ imaging-based screening to directly measure cilia. However, this approach may be complicated by the high sensitivity of the degree of ciliation of tissue culture cells to variation in proliferation state, confluence, and metabolic conditions. An alternative approach is to take advantage of the highly consistent levels of ciliation typically seen in free-living unicellular model organisms.

We have previously reported a simple cell-based assay for ciliary function suitable for small molecule screening in a 96 well plate format (Marshall, 2009). This assay exploits the unicellular green alga *Chlamydomonas reinhardtii* (Merchant et al., 2007), which swims through liquid media at a speed of 100-200 $\mu\text{m}/\text{sec}$ using its two flagella, which are structurally and molecularly equivalent to the cilia of animal cells. Much of our present molecular understanding of ciliary assembly and motility has come from experiments first performed in *Chlamydomonas*. Examples include the discovery of intraflagellar transport (Kozminski et al., 1993; Cole et al., 1998) and the identification of the radial spoke complex (Yang et al., 2006). Although *Chlamydomonas* is routinely used for genetic screens (Silflow and Lefebvre, 2001), chemical screens for flagella-affecting compounds in this organism have not been reported. Although the *Chlamydomonas* cell is surrounded by a strong cell wall that might impede drug entry into the cytoplasm, the flagella themselves protrude from the cell wall and

should therefore be fully accessible to any membrane-permeable small molecules in the growth media.

Our plate imaging-based motility assay exploits the tendency of certain wild-type strains of *Chlamydomonas* to dive rapidly to the bottom of a container. This movement requires active cell motility (Marshall, 2009). It is not currently known if this active diving to the bottom of the container is a form of gravitaxis driven by downward directed swimming, a form of negative phototaxis away from light that is more intense above versus below the plate, or some type of bioconvection (Pedley et al., 1988). For the purposes of our assay, we are less concerned with the mechanism of diving than with the fact that it is highly robust and reproducible. This is a strain-dependent behavior such that some wild-type strains will dive to the bottom of a container while other strains do not. Cells from diving strains grown in liquid culture will dive to the center of a U-bottom well, which is the well's lowest point. Importantly, cells that cannot swim are not able to move to the bottom and remain dispersed throughout the entire well (Marshall, 2009). Cellular distribution in the wells is easily visualized thanks to the green color produced by chlorophyll in the chloroplasts. Motile cells produce a dark green spot in the center of the well, while non-motile cells form a larger, light green circle with diameter equal to the well diameter (Figure 1A).

In this report, we employed this high throughput motility assay to screen a diverse set of drug-like small molecules and identified four that affect *Chlamydomonas* flagella. We named one of these compounds "ciliabrevin" because it also shortens the length of cilia in mammalian cells. In addition to

modulating ciliary length and intraflagellar transport speed and frequency, ciliabrevin also inhibits retrograde actin flow in *Drosophila* S2 cells, hinting at a possible link between actin dynamics and ciliogenesis.

Results

Screening collection of diverse compounds yields candidate hits

Prior to screening compounds, we conducted control experiments using mutant cells, comparing assay scores for wild-type cells versus *bld1* mutant cells (Brazelton et al., 2001) that lack flagella. We found that the coefficients of variation of the assay scores were in the range 6-8% for wild-type cells and 2-4% for mutant cells. We characterized assay selectivity using the Z'-factor (Zhang et al., 1999), a measure of the ability of the assay to discriminate positive from negative controls. The Z'-factor ranges from 0 to 1, with 1 being a perfect assay, 0 being a completely uninformative assay. A score over 0.5 is considered an "excellent assay" for cell-based high throughput screening (An and Tolliday, 2010) on the grounds that the assay is sufficiently selective to yield a high fraction of true hits without the assay becoming swamped with false positives. For our assay, we found that Z' was 0.72, using wild-type and *bld1* mutants as the two control groups. This score falls into the "excellent" range of Z' especially for cell-based assays, which tend naturally to have higher variability than assays with purified enzymes, and indicates the assay should be effective at discriminating motile from non-motile cells.

We screened a diverse set of 5520 compounds (results shown in Figure 1C). The average assay scores (“M” values, see materials and methods) were 4.5 ± 0.7 , 17.6 ± 0.8 , and 4.6 ± 0.8 for the negative control wells, positive control wells, and the 5520 unknown sample wells, respectively. To evaluate the efficacy of the screen, we calculated the Z-factor, another indicator of assay performance (Zhang et al., 1999), which differs from the Z'-factor in that rather than comparing a positive control set to a negative control set, it compares a positive control set to the results of a set of diverse compounds. Assays that are overly sensitive to perturbation by small molecules would give a low Z-factor, indicating that the false hit rate is unacceptably high for use in a screen. Like Z', Z factors range from 0 to 1, with 0 meaning the screen cannot work and 1 indicating an ideal screen. We calculated a Z-factor of 0.63, demonstrating that our assay is not overly sensitive to random small molecules. We also evaluated plate to plate variability by screening the first 2000 compounds in duplicate. The correlation coefficient for corresponding wells between the two sets of plates was 0.98, indicating a low plate to plate variability.

Out of the 5520 compounds screened, a total of 20 compounds were selected as potential hits because they gave high assay scores and also gave high scores for cell density, indicating a lack of toxicity (see Materials and Methods). In all cases, the original well images were visually inspected and it was confirmed that each of these candidate compounds caused cells to uniformly fill the wells, mimicking the pattern seen in motility-defective mutants (for example, see well E2 of the plate image in Figure 1A). All twenty compounds

continued to yield positive scores when re-assayed in fresh plates, confirming the reproducibility of the screening assay. Of these twenty compounds, sixteen were available for resupply from the vendor, and all of these continued to produce a positive assay score when the re-supplied compounds were re-tested using the same assay.

Secondary screening for effects on flagella

In principle there are many reasons why a *Chlamydomonas* cell might not undergo the diving behavior characteristic of the cc-124 strain, some of which might be unrelated to flagella, such as changes in cell density, viability, or membrane excitability (Yoshimura et al., 2003). We therefore tested the sixteen candidate compounds in a set of simple secondary assays. In our initial screen we had excluded overtly toxic compounds where cells failed to grow within one day. To test more carefully for subtler toxic effects, we grew lower density cultures in the presence of the compounds for four days, providing a more sensitive assay for effects on growth. Based on visual inspection of these cultures, we ruled out five compounds as having a noticeable effect on growth rates.

Next, we grew cultures for three days in the presence of each compound at doses sufficient to completely block diving behavior, mounted live cells under coverslips, and checked for presence of flagella using differential interference contrast (DIC) microscopy. Live imaging allowed us to determine if the cells were motile or not. From these rough visual analyses, we found that eight of the

sixteen compounds showed a clear-cut effect on flagella as judged by a majority of cells in the culture either lacking flagella or having paralyzed flagella that failed to beat at concentrations that produced no visually observable toxicity.

One potential non-specific effect that posed a possible concern is the pH shock response. Following a sudden drop in pH from neutral down to pH 4-5, *Chlamydomonas* cells undergo "flagellar autotomy", in which cilia are severed at the base and released into the media (Quarmby, 2004). To rule out the possibility that some of our compounds were sufficiently acidic that they triggered the pH shock response and therefore induced cilia loss for a trivial reason, we measured the pH of solutions of each compound diluted in cell growth media. We found that none of the compounds resulted in a detectable reduction in pH, with all cultures including untreated controls having pH 7.3, the usual pH of the TAP media used to grow the cells.

We next examined the homogeneity of the effect on a population of cells by microscopy-based examination of flagellar length and motility at a range of doses. We found that four of the eight compounds had non-homogenous effects, that is, at any non-toxic dose assayed, only a sub-set of cells showed a defect in the length or motility of the flagella, with others looking normal. Such compounds, which only affected a fraction of the total cell population, were deemed undesirable for follow-up because the heterogeneous response would not only greatly complicate further efforts to understand the nature of the effect, it would also limit the utility of the compounds as experimental tools for studying flagella. These four compounds were thus excluded from further consideration.

Such inhomogeneous effects had not been noticed during the initial screen, apparently because the non-motile cells were sufficiently numerous to provide a uniform green pattern filling the well, thus leading to a high assay score. These secondary screening assays thus narrowed the potential hits to four compounds that showed homogenous effects on flagella at non-toxic doses (Figure 2). Of these four, our preliminary visual survey indicated that one (compound B) affected the length of the flagella, while the other three (compounds E, F, and P) produced paralysis of flagellar motility. We named compound B "ciliabrevin", reflecting its ability to shorten cilia and flagella. The four candidate compounds were tested over a range of concentrations and scored for the fraction of cells that had motile flagella, paralyzed flagella, or no flagella after four hours of growth in the presence of compound. As indicated in Table 1, all four compounds showed activity in the micromolar range of concentrations.

Ciliabrevin induces flagellar shortening and loss

We noted that treatment with 30 μ M ciliabrevin (compound B) predominantly caused loss of flagella in the original assay, which involved 1-4 days of growth in the presence of the compound. If ciliabrevin really required multiple days to act, it would be far less useful as a tool for studies of flagellar dynamics than if its speed of action were relatively fast compared to cellular processes such as the cell cycle. Therefore, we monitored the flagellar phenotype as a function of time. We added ciliabrevin at a range of

concentrations and examined cells by DIC microscopy at regular intervals (Figure 3A). No immediate effect was seen after adding the compound, but by 30-60 minutes all cells that retained flagella had shortened their flagella depending on the dose of ciliabrevin added. These shorter steady-state flagellar lengths were then stably maintained for 12 hours when cells were left in the presence of the compound. While 25 μ M ciliabrevin produced cells with half-length flagella, higher concentrations of the compound did not shorten flagella further, but rather lead to flagellar loss and visible signs of toxicity, including cell lysis. In separate experiments, flagella returned to normal length within 2 hours following ciliabrevin wash out (data not shown). The time-scale of ciliabrevin action (\sim 1 hour) is thus substantially shorter than the time scale of the *Chlamydomonas* cell division cycle (\sim 8 hours). The fact that the flagella eventually stop shortening and remain constant at approximately half-length and no shorter could indicate a difference between the proximal and distal halves of the flagellum. Dentler reported that colchicine induces shortening of the distal but not proximal portions of the flagellum (Dentler and Adams, 1992), while Piperno has shown that the inner dynein arm protein composition of the proximal and distal halves of the flagellum are distinct (Piperno and Ramanis, 1991), and Yagi demonstrated that the proximal portion of the flagellum possesses novel low-abundance dynein heavy chains (Yagi et al., 2009). It is thus possible that whatever the target of ciliabrevin is, it has a more direct influence of dynamics of the distal half of the flagellum.

Ciliabrevin also affected the kinetics of flagellar regeneration following flagellar excision by pH shock (Lefebvre, 1995). We found that 25 μM ciliabrevin caused flagella to grow more slowly and reach a shorter steady-state length of ~ 8 μm (Figure 3B, red line), similar to the stable length that flagella shorten to when treated with the same concentration of the compound (Figure 3A, red line). This effect on the initial growth rate is distinct from the effect of protein synthesis inhibitors, which cause flagella to regenerate to a shorter length but have no effect on the initial growth rate (Rosenbaum et al., 1969).

These results show that ciliabrevin induces a dynamic dose-dependent shortening of flagella, which is accompanied by flagellar loss in a fraction of cells (see Table 1). Furthermore, flagellar regeneration in the presence of ciliabrevin proceeds more slowly and yields shorter flagella. Based on these observations, the balance-point model of flagellar length control (Marshall et al., 2005; Engel et al., 2009) predicts that ciliabrevin either decreases the assembly rate or increases the disassembly rate at the flagellar tip, as both shortening and regenerating flagella approach the same shorter steady-state length.

Effect of ciliabrevin on intraflagellar transport

The combined shortening and loss of flagella upon treatment with ciliabrevin is reminiscent of the phenotype observed in a specific class of *Chlamydomonas* mutants. These mutants are defective in the process of anterograde intraflagellar transport (IFT), the kinesin-powered transport of flagellar proteins from the cell body to the site of assembly at the flagellar tip

(Cole 2003; Scholey 2003; Pedersen and Rosenbaum, 2008). Anterograde IFT is also required to maintain flagella after assembly, and when conditional mutants in this process are shifted to the restrictive temperature, their flagella undergo shortening (Kozminski et al., 1995). The reported shortening rates seen in IFT conditional mutants following shift to restrictive temperature (Kozminski et al., 1995) are similar to the shortening rates that we observed here.

When conditional mutants in IFT are shifted to restrictive temperature, not only do the flagella shorten they also begin to detach from the cell (Adams et al., 1982; Parker and Quarmby, 2003). This flagellar detachment utilizes the same flagellar autotomy mechanism that causes flagellar detachment in response to pH shock (Parker and Quarmby, 2003), which is mediated by a physical severing of the flagella away from the cell at the base of the flagellum. The *fa1* mutation inhibits flagellar autotomy (Finst et al., 1998) and prevents conditional IFT mutants from detaching their flagella when IFT is turned off (Parker and Quarmby, 2003). We therefore asked whether the shedding of flagella induced by ciliabrevin would likewise require the flagellar autotomy system. We treated *fa1* mutant cells with 30 μ M ciliabrevin for 24 hours. While this concentration was sufficient to cause complete flagellar loss in wild-type cells, 82% of *fa1* mutant retained flagella after 24 hours of treatment. In this experiment we did not measure flagellar lengths, but only scored their presence or absence. We also tested *adf1* mutants (Finst et al., 1998), which block flagellar autotomy at an upstream signaling point but, unlike *fa1*, do not inhibit flagellar detachment following cessation of IFT (Jeremy Parker and Lynne Quarmby, personal

communication). Unlike the rescue seen with *fa1*, 97% of *adf1* mutant cells still lost their flagella following treatment with 30 μ M ciliabrevin. Thus, in terms of the induced flagellar shortening rate, the shedding of flagella, and interactions with the *fa1* and *adf1* mutants, ciliabrevin treatment appears to mimic the inhibition of IFT.

Based on the apparent similarities between ciliabrevin treatment and IFT loss, we imaged and quantified IFT in the flagella of living cells expressing a GFP-tagged subunit of the kinesin-2 anterograde motor using total internal reflection fluorescence (TIRF) microscopy (Figure 3C; Movie S1; method described in Engel et al., 2009 a,b). As plotted in Figures 3D-E, we found that IFT was not blocked in cells treated with 34 μ M ciliabrevin. However, the frequency and speed of anterograde IFT experienced a moderate decrease in full-length flagella that had begun to shorten following drug addition. Considering just full-length flagella, the average frequency of IFT particles passing any given point of the flagellum dropped from 1.26 ± 0.18 per second (N=16 flagella) to 1.08 ± 0.20 per second (N=28 flagella), and the speed of the particles dropped from 2.36 ± 0.18 μ m/sec to 1.87 ± 0.23 μ m/sec (\pm denotes standard deviation). These differences are statistically significant ($P < 0.003$, $t = 3.14$ and $P < 0.0001$, $t = 8.55$), indicating that ciliabrevin changes both the frequency and speed of intraflagellar transport in full-length flagella. Because we used the KAP subunit as the marker for IFT, which does not clearly reveal retrograde IFT traces (Engel et al., 2009 b), we were not able to determine whether or not ciliabrevin affects retrograde IFT or only anterograde. We have previously shown that anterograde

IFT speed and frequency vary moderately as a function of flagellar length in regenerating untreated cells (Engel et al., 2009 b), so one possible explanation is that the reduction in IFT speed and frequency are not a direct effect of ciliabrevin but rather an indirect effect of the flagellar shortening induced by the compound. However this observed correlation between IFT and flagellar length would not explain the fact that IFT speed and frequency were reduced in full-length ciliabrevin-treated flagella before they had undergone shortening.

It is interesting to note that the anterograde IFT speed in full-length ciliabrevin-treated flagella was reduced to exactly the speed that would normally be seen in regenerating flagella that are 6-8 μm in length (Figure 3D). This corresponds to the length that flagella would ultimately attain following ciliabrevin treatment, suggesting that the compound may alter the molecular regulatory pathways that control IFT as a function of flagellar length, adjusting the system to a new length set-point. However, because the exact role of IFT in the maintenance of flagellar length is still not fully understood (Marshall et al., 2005; Wemmer and Marshall, 2007), at this point we are not able to conclude whether the shortening and loss of flagella caused by ciliabrevin can be accounted for solely by the observed reduction in IFT speed and frequency.

Characterization of flagella-paralyzing compounds

In contrast to ciliabrevin, the other three remaining compounds obtained from our screen do not affect flagellar length, but rather seem to act by paralyzing flagellar motility. To quantify this effect, we treated cells for one hour

with compounds E and F at a range of concentrations listed in Table 2 and measured swimming speeds as described in the Materials and Methods. As shown in Table 2, both compounds show a dose-dependent reduction in swimming speed in the micromolar to sub-micromolar concentration range, confirming that these compounds do indeed result in paralysis of flagella-driven motility.

Effects of compounds in other cell types

We next tested whether any of the four compounds that we characterized in *Chlamydomonas* would have efficacy in cell types from other species. The ciliate *Paramecium aurelia* is a unicellular protozoan that swims using hundreds of cilia on its cell surface. We added the compounds at a concentration of 34 μM to cultures of *Paramecium* and examined the cells by microscopy after 1 hour and after 1 day. After 1 hour, ciliabrevin induced lysis of all cells in the culture. Compounds E, F, and P had no effect after 1 hour, nor did a DMSO control. In contrast, after 1 day of incubation with the compounds, the fraction of cells that were swimming dropped from 96% in controls to 37% in cells treated with compound E and 30% in cultures treated with compound F. In contrast, the fraction of swimming cells was 95% in cultures treated with compound P. We conclude that compounds E and F paralyze cilia-driven swimming in *Paramecium* while ciliabrevin causes rapid cell lysis and compound P produces no discernable effect.

We next tested the compounds on cultured mammalian cells. We added ciliabrevin to cultured mouse IMCD3 cells at a concentration of 14 μ M for three days and then visualized cilia by immunofluorescence (Figure 4). We found that ciliabrevin caused cilia to become roughly 25% shorter, comparable to the effect seen in *Chlamydomonas* with a similar concentration of the compound. Because the cilia of IMCD3 cells are normally non-motile we did not test the other compounds in this cell type. As an alternative cell culture system with motile cilia, we tested effect of the compounds on cultured mouse tracheal epithelial cells (MTECs), which are covered with arrays of beating cilia. Ciliabrevin reduced the fraction of cells with motile cilia from 45% down to 22% after 16 hours of treatment, while compounds E, F, and P had comparatively less effect, with fraction of cells with motile cilia after 16 hours measured as 28%, 29%, and 46%, respectively. After 40 hours of treatment, the fraction of cells with motile cilia dropped from 54% down to 20% after ciliabrevin treatment, while the fraction only dropped to 45% after 40 hours treatment with compound E, and in cells treated with compounds F, or P, the fraction of cells with motile cilia actually increased slightly. We conclude that ciliabrevin inhibits cilia formation in cultured mammalian cells, but that compounds E, F, and P have only minor effects, if any.

In order to determine if any of these compounds could be used to study cilia function in animal development, we treated zebrafish embryos by adding the compounds at a final concentration of 34 μ M to the embryo media. We found that ciliabrevin as well as compounds E and F caused embryos to die before

hatching, while compound P had no effect on development (data not shown). No obvious phenotypes attributable to cilia defects (e.g. kidney cysts) were detected in ciliabrevin treated fish other than an overall body curvature sometimes associated with ciliary defects (data not shown). At higher dosage, ciliabrevin treatment led to shortened body axis and embryonic lethality yet direct examination of embryos treated with ciliabrevin at various stages of development showed that cilia were still present in the embryos. We conclude that ciliabrevin has a broader impact on zebrafish development than affecting cilia alone, although we did not directly measure ciliary motility, leaving open the possibility that motility could have been affected.

Ciliabrevin reversibly arrests cytoskeletal dynamics in cultured cells

Because ciliabrevin shortens cilia, which are microtubule-based organelles, we decided to examine whether the compound affects the dynamics of cytoplasmic microtubules by direct microscopic observation of live *Drosophila* S2 cells expressing tubulin-GFP. Treatment with 34 μ M ciliabrevin caused a dramatic cessation of microtubule movements, abrogating both microtubule bending in the cell interior and the normal centripetal motion of free microtubule plus ends away from the cell periphery (Figure 5A; MovieS2). Microtubules lengthened for several minutes immediately after drug addition, then shortened to stable lengths (Figure 5A kymograph). The effects of ciliabrevin were reversible, as microtubule movements were restored within 10 minutes following washout with fresh media (data not shown).

In contrast, 1 μM taxol caused free tubulin to form small aggregates and microtubules to stiffen and break as they were pushed towards the center of the cell by inwardly-directed forces (Figure 5B; Movie S3). Pretreatment of cells with increasing concentrations of ciliabrevin slowed the centripetal movement of microtubules and tubulin aggregates following taxol addition (Figures 5C-E; Movies S4-S6; quantified in Figure 5G). When 34 μM ciliabrevin was added before taxol, microtubules were not pushed inwards at all, and instead appeared to thicken and acquire bulbous ends (Figure 5E; Movie S6). The retrograde motion of microtubules in these cells was restored following washout with one change of fresh media (Figure 5F; Movie S7), albeit at slower speeds due either to incomplete restoration of inwardly-directed forces or to strengthening of the thick bulbous microtubules. When 1 μM taxol was added before 34 μM ciliabrevin had stopped microtubule motion, the velocity of the inward movement of microtubule plus-ends from the cell periphery decayed over time as a simple exponential (Figure 5H; Movie S8), suggesting that ciliabrevin may reduce microtubule speed in a series of random independent events that irreversibly inactivate individual force-generating units in a stochastic manner.

One of the primary mechanical forces that moves microtubules in S2 cells is the retrograde flow of cortical actin from the cell periphery (Rodriguez et al., 2003). To address whether ciliabrevin affects actin dynamics, we imaged S2 cells expressing actin-GFP and Arp2-mCherry while adding increasing concentrations of the drug (Figure 6). Even at lower 7 μM and 17 μM concentrations, ciliabrevin arrested retrograde actin flow (Figure 6A-B; Movies

S9-S10). At 34 μ M, ciliabrevin not only inhibited retrograde flow, but also caused round actin-GFP aggregates to accumulate at the center of the cell (Figure 6C; Movie S11). Ciliabrevin began to act immediately after addition and partially or completely inhibited retrograde actin flow in a dose-dependent fashion, reaching full effect within 5-10 minutes (Figure 5E). These effects were reversible, as 10 minutes following washout of 34 μ M ciliabrevin with one change of fresh media, actin-GFP aggregates disappeared and retrograde flow was restored (Figure 6D; Movie S12). Like the cessation of microtubule movements in Figure 5H, the retrograde flow of Actin-GFP also slowed exponentially after drug addition, suggesting a mechanism of ciliabrevin action involving multiple independent random events (Figure 6F; Movie S11). Since retrograde actin flow involves a complex interplay between myosin motors and pathways regulating actin polymerization and depolymerization (reviewed in Welch et al., 1997), it is not possible to guess from these results what molecular element of the retrograde flow machinery might be affected by ciliabrevin.

The phenotype of ciliabrevin treatment shared some similarities with the actin-interfering drugs phalloidin, latrunculin B, and jasplakinolide, yet had unique characteristics of its own (Figure S1). Like ciliabrevin, phalloidin removed actin-GFP from the cell periphery and produced actin-GFP aggregates within the cytoplasm (Figure S1A, Movie S14). However, the phalloidin actin-GFP aggregates were more filamentous and less centrally located compared to ciliabrevin actin-GFP aggregates. Furthermore, phalloidin did not stop retrograde flux, as small particles were still seen moving inward from the cell periphery. The

effects of latrunculin B and jasplakinolide were even more distinct from ciliabrevin. Latrunculin B did stop retrograde actin flow, but left small actin-GFP aggregates throughout the cytoplasm and around the cell periphery (Figure S1C, Movie S16). Jasplakinolide produced a rapid increase in Actin-GFP fluorescence throughout the cytoplasm, which was pushed towards the cell center, where much of the fluorescence disappeared and the rest remained as bright Actin-GFP aggregates (Figure S1E, Movie S18). Drug washout with one change of fresh media produced a transient increase of cytoplasmic Arp2-mCherry followed by the restoration of actin-GFP dynamics in cells treated with ciliabrevin (Figure 6D, Movie S12, S13), phalloidin (Figure S1B, Movie S15), and latrunculin B (Figure S1D, Movie S17), but had no restorative effect on jasplakinolide-treated cells (Figure S1F, Movie S19). Ciliabrevin and phalloidin only robustly impaired actin dynamics at concentrations over 10 μ M, while latrunculin B and jasplakinolide were both potent at sub-micromolar concentrations. Considering the similarities in phenotypes, working concentrations, and washout, ciliabrevin most closely resembles phalloidin, though it differs in the cessation of retrograde flow and the production of round actin aggregates at the center of the cell.

Discussion

Efficacy of Chlamydomonas plate-well imaging based screen

This study demonstrates that our plate-well imaging based screen is able to identify compounds that affect the assembly and motility of cilia. This

suggests that if we continue this screen on a much larger scale it could be a productive source of new chemical tools for perturbing cilia.

The screen and secondary assays reported above were all performed in the unicellular green alga *Chlamydomonas reinhardtii*. This is one of the major model systems currently in use for studying cilia and flagella, and we expect that these compounds will provide useful tools to augment current genetic approaches in this organism. Ciliabrevin in particular, with its ability to reduce IFT speed and stably shorten flagella to specific lengths, may be applicable to studies of flagellar length regulation.

Our preliminary studies in different cell types suggest that of the four compounds we identified, only ciliabrevin has efficacy in vertebrate cells. However, this was a limited screen using a small number of compounds, and the fact that one out of four hits showed efficacy in vertebrate cells is actually encouraging for future prospects. If a greater number of compounds were screened in *Chlamydomonas*, it should be possible to obtain additional compounds that are applicable to vertebrate studies.

Joint inhibitor of ciliogenesis and retrograde actin flow

There are several conceivable explanations for the shared activity of ciliabrevin on both cilia and retrograde actin flow. One possibility is that there are simply two different targets hit by this compound, one affecting cilia and one affecting actin flow. We have no data at present to rule out this possibility. However, we note that components of the actin cytoskeleton, as well as

regulators of actin dynamics, are known to play important roles in various different aspects of ciliogenesis (Tamm and Tamm 1988; Boisvieux-Ulrich et al., 1990; Pan et al., 2007; Dawe et al., 2009; Bershteyn et al., 2010; Kim et al., 2010). Thus one possibility is that the compound hits one target molecule that is involved in both actin flow and ciliogenesis. A third, more interesting possibility is that the compound primarily targets actin and the effect on cilia reflects the role of actin itself in ciliogenesis. One published study indicates that cytochalasin treatment can result in flagellar shortening in *Chlamydomonas* (Dentler and Adams, 1992). A recent investigation combining inhibitors of actin regulation with micropatterned substrates to modulate cell stretching has further implicated actin networks in the regulation of ciliogenesis (Pitaval et al., 2010). It is also worth noting that actin is known to interact with cytoplasmic microtubules (Rodriguez et al., 2003), so that if the primary target of the drug is involved in the actin cytoskeleton, this could affect cytoplasmic microtubules which then might alter trafficking to the cilium or other aspects of ciliogenesis. Overall, our studies support the idea that actin perturbations might lead to effects on cilia, but further work will be required to test the role of actin perturbation on the cilia-related effects of ciliabrevin. In the meantime, ciliabrevin will provide a potentially useful tool to explore two important fundamental cell biological processes – ciliogenesis and actin flow.

Prospects for target identification

Identification of candidate compounds that affect cilia is clearly just the first step, and the more difficult task of identifying molecular targets still lies ahead. Indeed, identification of the relevant target is currently the major challenge in cell-based high throughput screening (An and Tolliday, 2010). Actin and components of the actin regulatory system are obvious candidate targets for ciliabrevin, however the chemical structure of ciliabrevin does not bear any obvious similarity to that of the standard natural product inhibitors of actin (latrunculin and cytochalasin).

The fact that our screen was performed in a genetically tractable unicellular model system means that resistance screens can in principle be used to identify potential molecular targets. Resistance screens have been conducted in *Chlamydomonas* using a number of microtubule-targeting herbicides and successfully identified mutations in alpha tubulin (James et al., 1993) confirming the feasibility of such an approach in this organism.

In the case of the paralyzing compounds E, F, and P, we performed a proof of concept suppression study using a series of mutants (sup-pf-1, sup-pf-2, and sup-pf-3) that are known to suppress mutations in the central pair of the flagella, restoring limited motility to mutants that are otherwise completely paralyzed (Porter et al., 1994). We treated each of these three suppressor strains with our compounds and found that the sup-pf-1 mutation conferred partial resistance to compound P (data not shown). Since the sup-pf-1 gene

encodes a component of the dynein regulatory complex, this result suggests that this complex, or an upstream regulatory factor, may be the target of compound P.

In the case of ciliabrevin, we note that this same compound was reported in a screen for inhibitors of calcium activated potassium channels (Sorensen et al., 2008). We do not know how this activity might relate to the effects of this compound on ciliogenesis, IFT, or actin flow, but this result does at least provide one possible starting point for target identification.

Materials and Methods

Plate-well image analysis assay

We used wild-type strain cc-124 obtained from the *Chlamydomonas* Genetic Center (www.chlamy.org), which we chose because it shows robust diving. Another wild-type strain of the opposite mating type, cc-125, does not exhibit this diving behavior, so in setting up this screen it is critical to make sure the starting strain reliably dives.

In our screen, cells were grown in TAP media to an OD₆₀₀ of 1.0 under continuous illumination in 200 ml flasks on a floor shaker, and then diluted to an OD₆₀₀ of 0.03 with fresh TAP media. 190 μ l of diluted cells were dispensed into wells of Corning Costar 96-well U-bottom clear polystyrene plates using a Wellmate dispenser system. Prior to adding cells, wells were pre-loaded with compounds from a diverse collection of small molecules whose structures predict drug-like properties (ChemDiv, San Diego, CA), to yield a final concentration of 5 μ M in 0.5% DMSO after addition of the cell media. Cell-based chemical screens are typically performed in the 1-10 μ M range. We chose a concentration in the middle of this range to balance the desire to obtain compounds with low effective doses with potential concerns that the hit rate might become too low if the screening concentration was further reduced. We did not perform any systematic tests to determine whether this particular concentration is optimal. The first and last columns of each plate were used for controls, the first column being a DMSO-only control and the last column being loaded with a culture of a non-motile mutant, *bld1*, that lacks flagella (Brazelton et al., 2001). Plates were

allowed to grow under continuous light for one day and then scanned with a flat-bed scanner (HP Scanjet 4070).

Custom software was used to analyze the plate images in a fully automated image processing pipeline, similar to that previously described (Marshall, 2009). Scanned RGB images of each plate were processed to extract a series of 96 sub-images corresponding to each well based on position within the image. The green channel was converted to black and white and the contrast inverted, so that darker pixels, indicating high density of green cells, were assigned larger numerical values. The software then estimated the distribution of cells as an intensity weighted first moment:

$$M = \frac{\sum_{x,y} I_{x,y} \sqrt{(x - \bar{x})^2 + (y - \bar{y})^2}}{\sum_{x,y} I_{x,y}}$$

Where x and y are the coordinates of each pixel, “ I ” is the intensity at each pixel, and summations are taken over all pixels in the well sub-image. The resulting first moment serves as the assay score for that well, as depicted in the heat map of Figure 1B. Potential hits can be detected as wells with a high value of “ M ”.

Because the calculation of the assay score “ M ” involves normalization by the total intensity over the whole well, toxic compounds can yield high assay scores since cell death can lead to a low uniform greenish-yellow coloration throughout the well. Hence, we implemented a built-in counter screen for toxicity by measuring the average cell density in each well based on the average intensity of the well images. Outliers with average density more than three

standard deviations below that measured in control wells were scored as toxic and discarded from further analysis.

Secondary assays in Chlamydomonas

For secondary assays, resupplied compounds were stored as stock compounds in 100% DMSO at a concentration of 1 mg/ml, and then used at dilutions indicated in the text and tables.

Visual assessment of the presence or absence of flagella (Table 1) was performed by mounting 10 μ l of live cell culture under a coverslip with a Vaseline ring and imaging on a Zeiss Axioskop using a 40x air lens and DIC optics (Carl Zeiss MicroImaging, LLC, Thornwood, NY). Swimming speeds (Table 2) were calculated by adjusting the condenser on a Zeiss Axioskop to give a dark-field like image, then acquiring 0.5 second exposures with a SPOT camera (Diagnostic Instruments, Sterling Heights, MI). This produced streak-like images for swimming cells, and speed was estimated by tracing the length of each streak using the SPOT analysis software and dividing length by the exposure time. Flagellar regeneration (Figure 3B) was performed by transiently lowering the pH of liquid cultures as previously described (Lefebvre, 1995). Detailed flagellar length measurements in fixed *Chlamydomonas* cells (Figures 3A, 3B) were attained by capturing images on a Zeiss Axioskop equipped with a SPOT camera and measuring flagellar lengths with NIS-Elements AR software (version 3.2, Nikon).

For TIRF measurement of IFT, cells expressing GFP-tagged kinesin-2 motor subunit KAP (Mueller et al., 2005) were grown in TAP media under continuous illumination in test tubes on a roller drum. Cells were mounted and imaged as previously described (Engel et al., 2009 a), and IFT speeds were measured by kymograph analysis as detailed previously (Engel et al., 2009 b).

Mouse IMCD3 and MTEC cell culture methods

Mouse IMCD3 cells were cultured in Dulbecco's modified Eagle's medium and Ham's F-12 medium mixture containing 10% heat-inactivated fetal bovine serum (FBS) at 37°C in 5% CO₂. Cells were cultured on acid-washed coverslips, fixed with methanol for 5 min at -20°C, and washed three times with phosphate-buffered saline (PBS). Cells were blocked in 1% bovine serum albumin in PBS for 10 min at room temperature and incubated with primary antibodies for 1 hour in a humid chamber. Cells were then washed with PBS and incubated with FITC, TRITC and Cy5 conjugated secondary antibodies (Jackson ImmunoResearch laboratories, West Grove, PA) for 30 min. Samples were washed with PBS and mounted with Vectashield (Vector laboratory, Burlingame, CA), then observed using a DeltaVision microscope (Applied Precision, Issaquah, WA) with a 60x objective (Olympus, Tokyo, Japan). Z-stack images were obtained at 0.2- μ m intervals, then deconvolved and projected with DeltaVision software (Applied Precision).

MTECs were derived and cultured essentially as described (You et al, 2002). Briefly, tracheae were excised from adult mice, cleaned of surrounding

tissue, and digested with 1.5 mg/ml Pronase (Roche) overnight at 4°C. The next day, FBS (Cellgro) was added to neutralize the enzyme, and the suspended tracheae were inverted to release cells. The supernatant was centrifuged at 200 x g and the cell pellet was resuspended in MTEC/Basic (You et al, 2002) media and plated for 4 hours at 37°C to remove contaminating fibroblasts. The supernatant was again removed, spun, and resuspended in MTEC/Plus (You et al, 2002) media. 2.5×10^4 MTECs were plated on 0.4 µm collagen I (Roche) coated Transwell inserts (Corning) and media was added to the upper and lower chambers. After confluence was reached, media was removed from the upper chamber, and MTEC/NS (You et al, 2002) was added to the lower chamber to create an air-liquid interface (ALI) and induce the ciliary differentiation program. After 7-10 days of culture, MTECs were treated with compounds for 24 h, and were then imaged using established procedures (Wilson et al, 2009).

Analysis of cytoskeletal dynamics in Drosophila S2 cells

Cells were grown at room temperature in Schneider's *Drosophila* medium supplemented with 10% fetal bovine serum. Before imaging, cells were plated on 14 mm glass bottom microwell dishes (P35G-1.5-14-C, MatTek, Ashland, MA) coated with 10% Concanavalin A, and allowed to adhere for 1-2 hours. The time allowed for cell adhesion was important to ensure that cells were well spread but still had roughly uniform circular morphology. Drug addition was performed without interrupting movie acquisition by carefully adding 10 µl of a 10x dilution of drug in cell media to 90 µl cell media already covering the cells. Washout was

also performed without interrupting movie acquisition by carefully pipetting out the drugged media and replacing it with 150 μ l fresh media without touching the cell chamber. Towards the end of each movie, signal intensity decreased due to GFP photobleaching. Cells were imaged on a Nikon Eclipse Ti-E motorized inverted spinning disc confocal microscope (Nikon, Tokyo, Japan), equipped with an integrated Nikon Perfect Focus System, a 100x/1.40na oil Plan Apo VC objective, and a Photometrics Evolve EMCCD camera (Photometrics, Tucson, AZ).

Four kymographs were generated from each movie (vertical, horizontal, and two diagonal cross-sections) using a custom-made ImageJ plugin (version 1.42g, National Institutes of Health) that plotted the maximum intensity along each point of a straight 50-pixel wide line for each movie frame. The speed of retrograde microtubule and actin flux was calculated from the angle of traces moving inward from the cell periphery (measured with ImageJ) and average speeds for each movie were plotted in Figures 5G and 6E. The plots of microtubule and actin position in Figures 5H and 6F were generated with a custom-made Matlab script (version R2007a, Mathworks), which plotted peak pixel intensities from a single kymograph trace and fitted this distribution with a simple exponential decay trend line.

Acknowledgements

We thank Ethan Scott and Herwig Baier for providing *Paramecium* cultures; Elena Ingerman, Lauren Goins, and Dyche Mullins for providing *Drosophila* S2 cells expressing actin-GFP and ARP2-mCherry; Sarah Goodwin and Ron Vale for providing S2 cells expressing tubulin-GFP; and Prachee Crofts for careful reading of the manuscript. We are grateful to Kurt Thorn for microscopy assistance and the Nikon Imaging Center at UCSF for access to the confocal and TIRF microscopes used in the study. Susanne Rafelski designed the ImageJ kymograph plugin. This work was funded by the Sandler Program in Basic Science and the W.M. Keck Foundation.

Table 1. Dose response for candidate compounds. Cells were grown for four hours with the indicated dose of compound and then examined by DIC microscopy and scored for percent of cells having normal beating flagella, paralyzed flagella, or lacking flagella.

Compound	Concentration (μ M)	Normal (%)	Paralyzed (%)	Lacking
B	3	83	17	0
	6	75	25	0
	15	80	5	15
	30	24	15	61
E	0.6	0	100	0
	1.5	0	100	0
	3	0	76	24
	6	0	51	49
	15	3	20	77
	30	0	7	93
F	0.6	38	57	5
	1.5	11	86	1
	3	1	98	1
	6	1	75	24

P	0.6	65	35	0
	1.5	15	85	0
	3	4	96	0

Table 2. *Swimming speed versus concentration of compounds E and F*

Compound	Concentration (μM)	Swimming Speed ($\mu\text{m}/\text{sec}$)
E	0.15	83.3 ± 21.3
	0.3	56.2 ± 29.7
	0.6	23.2 ± 26.3
	1.5	11.9 ± 5.2
F	0.15	108.2 ± 14.3
	0.3	106.3 ± 12.7
	0.6	90.2 ± 25.3
	1.5	46.7 ± 32.7

Figure Legends

Figure 1. Screen characterization and results. (A) Image of a plate from the assay. In all plates, untreated wild-type cells were loaded on the left column of 8 wells in media containing 0.5% DMSO as a negative control and *bld1* mutant cells lacking flagella were loaded on the right column of 8 wells as a positive control. (B) Heat-map scoring of a typical plate. Color scale shown on inset color-bar, ranging from 4 (dark blue, indicating a small assay score characteristic of untreated cells) to 18 (red, indicating a high assay score characteristic of non-motile cells). (C) Screening statistics. Red and green marks signify positive (*bld1* mutants) and negative (untreated wild-type cells) controls, respectively. Gray circles signify unknown compounds. Red and green lines indicate three standard deviations above and below the mean assay scores for positive and negative controls, respectively.

Figure 2. Structures of candidate compounds obtained in the initial screen and validated in secondary assays to confirm homogenous effects at non-toxic doses.

Figure 3. Effects of ciliabrevin (compound B) on *Chlamydomonas* flagellar length and intraflagellar transport. (A) Flagellar length versus time after addition of ciliabrevin to wild-type cc-125 cells at a variety of concentrations. N= 3698 flagella for all concentrations and timepoints combined. (B) Regeneration kinetics of wild-type cc-125 flagella following pH shock in the presence (red) or absence (blue, adapted from Engel et al., 2009 b) of 25 μ M ciliabrevin. N= 2464

flagella with ciliabrevin and 2178 flagella without drug. (C) Kymograph of a KAP-GFP cell imaged by TIRF microscopy, showing anterograde IFT traces 1 hour after addition of 34 μ M ciliabrevin. Horizontal scale bar= 2 μ m, vertical scale bar= 2 seconds. (D) Speed and (E) frequency of anterograde KAP-GFP traffic during pH shock regeneration (blue, adapted from Engel et al., 2009 b) and 34 μ M ciliabrevin-induced shortening (red), binned by flagellar length. Error bars in all panels indicate 99% confidence intervals. N= 94 flagella with ciliabrevin and 101 flagella without drug.

Figure 4. Effect of ciliabrevin (compound B) on mammalian cell ciliary length. (A) Control mouse IMCD3 cells and (B) IMCD3 cells treated with 14 μ M ciliabrevin, showing reduced cilia length. Cells were stained for the cilia marker acetylated tubulin (green), the cell junction marker ZO-1 (red), and the centrosome marker pericentrin (magenta). Scale bar= 10 μ m. (C) Average length of cilia in treated and control IMCD3 cells. Error bars indicate 99% confidence intervals. (D) Ciliary length distribution in treated (red) and control (blue) cells. N= 931 control cilia and 562 cilia in presence of drug.

Figure 5. Effects of ciliabrevin (compound B) on tubulin dynamics in *Drosophila* S2 cells. (A-F) Cells expressing tubulin-GFP were treated with ciliabrevin, taxol, both drugs sequentially, or cells treated with both drugs and then washed with fresh media as indicated. Frames from movies are shown in left panels, kymographs generated from cross-sections of movies are shown in right panels.

The time following drug addition or washout is indicated on the movie frame panels, Pre= before treatment. On kymographs, black arrowheads= ciliabrevin addition, white arrowheads= taxol addition, asterisks= drug washout. Horizontal scale bar= 10 minutes, vertical scale bar= 10 μm . (G) Quantification of the mean microtubule retrograde flux speed for the experiments in panels B-F, before (blue) and after (red) drug addition or washout. Error bars indicate 99% confidence intervals. (H) Plot of the maximum pixel intensity position vs. time (blue line) and exponential decay fit (red line) of a kymograph trace from a cell where 1 μM taxol was added before 34 μM ciliabrevin had stopped the retrograde flux of microtubule plus ends.

Figure 6. Effects of ciliabrevin (compound B) on actin dynamics in *Drosophila* S2 cells. (A-D) Cells expressing actin-GFP (green) and Arp2-mCherry (red) were treated with increasing concentrations of ciliabrevin or washed with fresh media as indicated. Two-color frames from movies are shown in left panels, Actin-GFP kymographs generated from cross-sections of movies are shown in right panels. The time following drug addition or washout is indicated on the movie frame panels, Pre= before treatment. On kymographs, black arrowheads= ciliabrevin addition, asterisks= drug washout. Horizontal scale bar= 10 minutes, vertical scale bar= 10 μm . (E) Measurement of the mean actin retrograde flow speed over time following ciliabrevin addition for the experiments in panels A-D. Error bars indicate 99% confidence intervals. (F) Plot of the maximum pixel intensity position vs. time (blue line) and exponential decay fit (red line) of a

kymograph trace from a cell where actin flow was stopped by adding 34 μM ciliabrevin.

Figure S1. Effects of known actin-inhibiting drugs on actin dynamics in *Drosophila* S2 cells expressing actin-GFP (green) and Arp2-mCherry (red). (A) Addition of 20 μM phalloidin and (B) washout with one change of fresh media. (C) Addition of 1 μM latrunculin B and (D) washout. (E) Addition of 1 μM jasplakinolide and (D) washout. The time following drug addition or washout is indicated on the movie frame panels, Pre= before treatment. Vertical scale bar= 10 μm .

Supplementary Videos

Video S1. TIRF microscopy of a *Chlamydomonas* cell expressing KAP-GFP and treated with 34 μ M ciliabrevin for one hour. This movie was used to generate the kymograph displayed in Figure 3C. Acquired at \sim 30 frames per second, movie play speed is real-time.

Video S2. Confocal microscopy of *Drosophila* S2 cells expressing tubulin-GFP. Treated with 34 μ M ciliabrevin, corresponds to data in Figure 5A. Acquired at 1 frame every 3 seconds, movie play speed is 60x real-time (1 second = 1 minute). Ciliabrevin addition occurs 4 seconds into the movie. Reduction in image intensity at the end of the movie is due to GFP photobleaching.

Video S3. Confocal microscopy of *Drosophila* S2 cells expressing tubulin-GFP. Treated with 1 μ M taxol, corresponds to data in Figure 5B. Acquired at 1 frame every 3 seconds, movie play speed is 60x real-time (1 second = 1 minute). Taxol addition occurs 9 seconds into the movie.

Video S4. Confocal microscopy of *Drosophila* S2 cells expressing tubulin-GFP. Treated with 7 μ M ciliabrevin followed by 1 μ M taxol, corresponds to data in Figure 5C. Acquired at 1 frame every 3 seconds, movie play speed is 60x real-time (1 second = 1 minute). Ciliabrevin addition occurs 4 seconds into the movie, followed by taxol addition at 6 seconds.

Video S5. Confocal microscopy of *Drosophila* S2 cells expressing tubulin-GFP. Treated with 17 μ M ciliabrevin followed by 1 μ M taxol, corresponds to data in Figure 5D. Acquired at 1 frame every 3 seconds, movie play speed is 60x real-time (1 second = 1 minute). Ciliabrevin addition occurs 4 seconds into the movie, followed by taxol addition at 7 seconds.

Video S6. Confocal microscopy of *Drosophila* S2 cells expressing tubulin-GFP. Treated with 34 μ M ciliabrevin followed by 1 μ M taxol, corresponds to data in Figure 5E. Acquired at 1 frame every 3 seconds, movie play speed is 60x real-time (1 second = 1 minute). Ciliabrevin addition occurs 3 seconds into the movie, followed by taxol addition at 5 seconds.

Video S7. Confocal microscopy of *Drosophila* S2 cells expressing tubulin-GFP. Washout of 34 μ M ciliabrevin and 1 μ M taxol with one change of fresh media, corresponds to data in Figure 5F. Acquired at 1 frame every 3 seconds, movie play speed is 60x real-time (1 second = 1 minute). Washout occurs 2 seconds into the movie,

Video S8. Confocal microscopy of *Drosophila* S2 cells expressing tubulin-GFP. Treated with 34 μ M ciliabrevin followed by 1 μ M taxol before microtubule movements had stopped, corresponds to data in Figure 5H. Acquired at 1 frame every 3 seconds, movie play speed is 60x real-time (1 second = 1 minute).

Ciliabrevin addition occurs 4 seconds into the movie, followed by taxol addition at 5 seconds.

Video S9. Confocal microscopy of *Drosophila* S2 cells expressing actin-GFP and Arp2-mCherry. Treated with 7 μ M ciliabrevin, corresponds to data in Figure 6A. Acquired at 1 frame every 3 seconds, movie play speed is 60x real-time (1 second = 1 minute). Ciliabrevin addition occurs 2 seconds into the movie.

Video S10. Confocal microscopy of *Drosophila* S2 cells expressing actin-GFP and Arp2-mCherry. Treated with 17 μ M ciliabrevin, corresponds to data in Figure 6B. Acquired at 1 frame every 3 seconds, movie play speed is 60x real-time (1 second = 1 minute). Ciliabrevin addition occurs 2 seconds into the movie.

Video S11. Confocal microscopy of *Drosophila* S2 cells expressing actin-GFP and Arp2-mCherry. Treated with 34 μ M ciliabrevin, corresponds to data in Figures 6C,F. Acquired at 1 frame every 3 seconds, movie play speed is 60x real-time (1 second = 1 minute). Ciliabrevin addition occurs 2 seconds into the movie.

Video S12. Confocal microscopy of *Drosophila* S2 cells expressing actin-GFP and Arp2-mCherry. Washout of 34 μ M ciliabrevin with one change of fresh media, corresponds to data in Figure 6D. Acquired at 1 frame every 3 seconds,

movie play speed is 60x real-time (1 second = 1 minute). Washout occurs 2 seconds into the movie.

Video S13. Confocal microscopy of *Drosophila* S2 cells expressing actin-GFP and Arp2-mCherry. Washout of 17 μ M ciliabrevin with one change of fresh media. Acquired at 1 frame every 3 seconds, movie play speed is 60x real-time (1 second = 1 minute). Washout occurs 2 seconds into the movie.

Video S14. Confocal microscopy of *Drosophila* S2 cells expressing actin-GFP and Arp2-mCherry. Treated with 20 μ M phalloidin, corresponds to data in Figure S1A. Acquired at 1 frame every 3 seconds, movie play speed is 60x real-time (1 second = 1 minute). Phalloidin addition occurs 2 seconds into the movie.

Video S15. Confocal microscopy of *Drosophila* S2 cells expressing actin-GFP and Arp2-mCherry. Washout of 20 μ M phalloidin with one change of fresh media, corresponds to data in Figure S1B. Acquired at 1 frame every 3 seconds, movie play speed is 60x real-time (1 second = 1 minute). Washout occurs 2 seconds into the movie.

Video S16. Confocal microscopy of *Drosophila* S2 cells expressing actin-GFP and Arp2-mCherry. Treated with 1 μ M latrunculin B, corresponds to data in Figure S1C. Acquired at 1 frame every 3 seconds, movie play speed is 60x real-

time (1 second = 1 minute). Latrunculin B addition occurs 2 seconds into the movie.

Video S17. Confocal microscopy of *Drosophila* S2 cells expressing actin-GFP and Arp2-mCherry. Washout of 1 μ M latrunculin B with one change of fresh media, corresponds to data in Figure S1D. Acquired at 1 frame every 3 seconds, movie play speed is 60x real-time (1 second = 1 minute). Washout occurs 2 seconds into the movie.

Video S18. Confocal microscopy of *Drosophila* S2 cells expressing actin-GFP and Arp2-mCherry. Treated with 1 μ M jasplakinolide, corresponds to data in Figure S1E. Acquired at 1 frame every 3 seconds, movie play speed is 60x real-time (1 second = 1 minute). Jasplakinolide addition occurs 2 seconds into the movie.

Video S19. Confocal microscopy of *Drosophila* S2 cells expressing actin-GFP and Arp2-mCherry. Washout of 1 μ M jasplakinolide with one change of fresh media, corresponds to data in Figure S1F. Acquired at 1 frame every 3 seconds, movie play speed is 60x real-time (1 second = 1 minute). Washout occurs 1 second into the movie.

References

- Adams GM, Huang B, Luck DJ. 1982. Temperature-sensitive, assembly defective flagellar mutants of *Chlamydomonas reinhardtii*. *Genetics* 100, 579-586.
- Afzelius BA. 2004. Cilia-related diseases. *J. Pathol.* 204, 470-477.
- An WF, Tolliday N. 2010. Cell-based assays for high-throughput screening. *Mol. Biotechnol.* 45, 180-186.
- Badano JL, Mitsume N, Beales PL, Katsanis N. 2006. The ciliopathies: an emerging class of human genetic disorders. *Annu. Rev. Genomics Hum. Genet.* 7, 125-48.
- Beck C, Uhl R. 1994. On the localization of voltage-sensitive calcium channels in the flagella of *Chlamydomonas reinhardtii*. *J. Cell Biol.* 125, 1119-1125.
- Berman, S.A., Wilson, N.F., Haas, N.A., and Lefebvre, P.A. 2003. A novel MAP kinase regulates flagellar length in *Chlamydomonas*. *Curr. Biol.* 13, 1145-1149.
- Bershtyn M, Atwood SX, Woo WM, Li M, Oro AE. 2010. MIM and cortactin antagonism regulates ciliogenesis and hedgehog signaling. *Dev. Cell* 19, 270-283.
- Besschetnova TY, Kolpakova-Hart E, Guan Y, Zhou J, Olsen BR, Shah JV. 2010. Identification of signaling pathways regulating primary cilium length and flow-mediated adaptation. *Curr. Biol.* 20, 182-187.
- Boisvieux-Ulrich E, Laine MC, Sandoz D. 1990. Cytochalasin D inhibits basal body migration and ciliary elongation in quail oviduct epithelium. *Cell Tissue Res.* 259, 443-454.
- Brazelton WJ, Amundsen CD, Silflow CD, Lefebvre PA. 2001. The bld1 mutation identifies the *Chlamydomonas* osm-6 homolog as a gene required for flagellar assembly. *Curr. Biol.* 11, 1591-1594.
- Cole DG, Diener DR, Himelblau AL, Beech PL, Fuster JC, Rosenbaum JL. 1998. *Chlamydomonas* kinesin-II-dependent intraflagellar transport (IFT): IFT particles contain proteins required for ciliary assembly in *Caenorhabditis elegans* sensory neurons. *J. Cell Biol.* 141, 993-1008.
- Cole DG. 2003. The intraflagellar transport machinery of *Chlamydomonas reinhardtii*. *Traffic* 4, 435-442.
- Dawe HR, Adams M, Wheway G, Szymanska K, Logan CV, Noegel AA, Gull K, Johnson CA. 2009. Nesprin-2 interacts with meckelin and mediates ciliogenesis via remodeling of the actin cytoskeleton. *J. Cell Sci.* 112, 2716-2726.
- Dentler WL, Adams C. 1992. Flagellar microtubule dynamics in *Chlamydomonas*: cytochalasin D induces periods of microtubule shortening and elongation; and colchicine induces disassembly of the distal, but not proximal, half of the flagellum. *J. Cell Biol.* 117, 1289-1298.
- Engel BD, Lehtreck KF, Sakai T, Ikebe M, Witman GB, Marshall WF. 2009a. Total internal reflection fluorescence (TIRF) microscopy of *Chlamydomonas* flagella. *Meth. Cell Biol.* 93, 157-177.

- Engel BD, Ludington WB, Marshall WF. 2009b. Intraflagellar transport particle size scales inversely with flagellar length: revisiting the balance-point length control model. *J. Cell Biol.* 187, 81-89.
- Finst RJ, Kim PJ, Quarmby LM. 1998. Genetics of the deflagellation pathway in *Chlamydomonas*. *Genetics* 149: 927-936.
- Fliegauf M, Benzing T, Omran H. 2007. When cilia go bad: cilia defects and ciliopathies. *Nat. Rev. Mol. Cell Biol.* 8, 880-893.
- Gaudana R, Ananthula HK, Parenky A, Mitra AK. 2010. Ocular drug delivery. *AAPS J.* 12, 348-60.
- Gherman A, Davis EE, Katsanis N. 2006. The ciliary proteome database: an integrated community resource for the genetic and functional dissection of cilia. *Nat. Genet.* 38, 961-962.
- Huangfu D, Anderson KV. 2005. Cilia and hedgehog responsiveness in the mouse. *Proc. Natl. Acad. Sci. U.S.A.* 102, 11325-30.
- Hyman JM, Firestone AJ, Heine VM, Zhao Y, Ocasio CA, Han K, Sun M, Rack PG, Sinha S, Wu JJ, Solow-Cordero DE, Jiang J, Rowitch DH, Chen JK. 2009. Small-molecule inhibitors reveal multiple strategies for Hedgehog pathway blockade. *Proc. Natl. Acad. Sci. U.S.A.* 106, 14132-14137.
- Inglis PN, Borojevich KA, Leroux MR. 2006. Piecing together a ciliome. *Trends. Genet.* 22, 491-500.
- James SW, Silflow CD, Stroom P, Lefebvre PA. 1993. A mutation in the alpha 1-tubulin gene of *Chlamydomonas reinhardtii* confers resistance to anti-microtubule herbicides. *J. Cell Sci.* 106, 209-218.
- Kim J, Lee JE, Heynen-Genel S, Suyama E, Ono K, Lee K, Idekar T, Aza-Blanc P, Gleeson JG. 2010. Functional genomic screen for modulators of ciliogenesis and cilium length. *Nature* 464, 1048-1051.
- Kleinstreuer C, Zhang C, Donohue JF. 2008. Targeted drug-aerosol delivery in the human respiratory system. *Annu. Rev. Biomed. Eng.* 10, 195-220.
- Kozminski KG, Johnson KA, Forscher P, Rosenbaum JL. 1993. A motility in the eukaryotic flagellum unrelated to flagellar beating. *Proc. Natl. Acad. Sci. USA* 90, 5519-5523.
- Kozminski KG, Beech PL, Rosenbaum JL. 1995. The *Chlamydomonas* kinesin-like protein FLA10 is involved in motility associated with the flagellar membrane. *J. Cell Biol.* 131, 1517-1527.
- Lefebvre PA. 1995. Flagellar amputation and regeneration in *Chlamydomonas*. *Meth. Cell Biol.* 47, 3-7.
- Marshall, W.F., Qin, H., Rodrigo Brenni, M., and Rosenbaum, J.L. 2005. Flagellar length control system: testing a simple model based on intraflagellar transport and turnover. *Mol. Biol. Cell* 16, 270-278.
- Marshall, W.F. 2008. The cell biological basis of ciliary disease. *J. Cell Biol.* 180, 17-21.

- Marshall, W.F. 2009. Quantitative high-throughput assays for flagella-based motility in *Chlamydomonas* using plate-well image analysis and transmission correlation spectroscopy. *J. Biomol. Screening* 14, 133-141.
- Merchant S, et al. 2007. The *Chlamydomonas* genome reveals the evolution of key animal and plant functions. *Science* 318, 245-250.
- Mueller, J., Perrone, C.A., Bower, R., Cole, D.G., and Porter, M.E. 2005. The FLA3 KAP subunit is required for localization of kinesin-2 to the site of flagellar assembly and processive anterograde intraflagellar transport. *Mol. Biol. Cell* 16, 1341-1354.
- Nakamura S, Takino H, Kojima MK. 1987. Effect of lithium on flagellar length in *Chlamydomonas reinhardtii*. *Cell Struct Funct.* 12, 369-374.
- Ou Y, Ruan Y, Cheng M, Moser JJ, Rattner JB, van der Hoorn FA. 2009. Adenylate cyclase regulates elongation of mammalian primary cilia. *Exp. Cell Res.* 315, 2802-2817.
- Pan J, Wang Q, Snell WJ. 2004. An aurora kinase is essential for flagellar disassembly in *Chlamydomonas*. *Dev Cell* 6, 445-451.
- Pan J, You Y, Huang T, Brody SL. 2007. RhoA-mediated apical actin enrichment is required for ciliogenesis and promoted by Foxj1. *J. Cell Sci.* 120, 1868-1876.
- Parker JD, Quarmbly LM. 2003. *Chlamydomonas* fla mutants reveal a link between deflagellation and intraflagellar transport. *BMC Cell Biol.* 4, 11.
- Pazour GJ, Agrin N, Leszyk J, Witman GB. 2005. Proteomic analysis of a eukaryotic cilium. *J. Cell Biol.* 170, 103-113.
- Pedley TJ, Hill NA, Kessler JO. 1988. The growth of bioconvection patterns in a uniform suspension of gyrotactic micro-organisms. *J. Fluid Mech.* 195, 223-237.
- Pedersen LB, Veland IR, Schroder J, Christensen ST. 2008. Assembly of primary cilia. *Dev. Dyn.* 237, 1993-2006.
- Pedersen LB, Rosenbaum JL. 2008. Intraflagellar transport (IFT) role in ciliary assembly, resorption and signaling. *Curr. Top. Dev. Biol.* 85, 23-61.
- Peterson JR, Mitchison TJ. 2002. Small molecules, big impact: a history of chemical inhibitors and the cytoskeleton. *Chem. Biol.* 9, 1275-1285.
- Piperno G, Ramanis Z. 1991. The proximal portion of *Chlamydomonas* flagella contains a distinct set of inner dynein arms. *J. Cell Biol.* 112, 701-9.
- Pitaval A, Tseng Q, Bornens M, They M. 2010. Cell shape and contractility regulate ciliogenesis in cell cycle-arrested cells. *J. Cell Biol.* 191, 303-312.
- Porter ME, Knott JA, Gardner LC, Mitchell DR, Dutcher SK. 1994. Mutations in the SUP-PF-1 locus of *Chlamydomonas reinhardtii* identify a regulatory domain in the beta-dynein heavy chain. *J. Cell Biol.* 126, 1495-1507.
- Qin H, Wang Z, Diener D, Rosenbaum J. 2007. Intraflagellar transport protein 27 is a small G protein involved in cell-cycle control. *Curr. Biol.* 17, 193-202.

- Qin H, Burnette DT, Bae YK, Forscher P, Barr MM, Rosenbaum JL. 2005. Intraflagellar transport is required for the vectorial movement of TRPV channels in the ciliary membrane. *Curr. Biol.* 15, 1695-1699.
- Quarmany LM. 2004. Cellular deflagellation. *Int. Rev. Cytol.* 233, 47-91.
- Rodriguez OC, Schaefer AW, Mandato CA, Forscher P, Bement WM, Waterman-Storer CM. 2003. Conserved microtubule-actin interactions in cell movement and morphogenesis. *Nat. Cell Biol.* 5, 599-609.
- Rosenbaum JL, Moulder JE, Ringo DL. 1969. Flagellar elongation and shortening in *Chlamydomonas*. The use of cycloheximide and colchicine to study the synthesis and assembly of flagellar proteins. *J. Cell Biol.* 41, 600-619.
- Santos N, Reiter JF. 2008. Building it up and taking it down: the regulation of vertebrate ciliogenesis. *Dev. Dyn.* 237, 1972-81.
- Satir P, Pedersen LB, Christensen ST. 2010. The primary cilium at a glance. *J. Cell Sci.* 123, 499-503.
- Scholey JM. 2003. Intraflagellar transport. *Ann. Rev. Cell Dev. Biol.* 19, 423-443.
- Sloboda RD, Rosenbaum JL. 2007. Making sense of cilia and flagella. *J. Cell Biol.* 179, 575-582.
- Silflow CD, Lefebvre PA. 2001. Assembly and motility of eukaryotic cilia and flagella. Lessons from *Chlamydomonas reinhardtii*. *Plant. Physiol.* 127, 1500-1507.
- Sorensen US, Strobaek D, Christophersen P, Hougaard C, Jensen ML, Nielsen, EO, Peters D, Teuber L. 2008. Synthesis and Structure-Activity Relationship Studies of 2-(N-Substituted)-aminobenzimidazoles as Potent Negative Gating Modulators of Small Conductance Ca²⁺-Activated K⁺ Channels. *J Med Chem.* 51, 7625-7634.
- Tamm S, Tamm SL. 1988. Development of macrociliary cells in Beroe. I. Actin bundles and centriole migration. *J. Cell Sci.* 89, 67-80.
- Tuxhorn J, Daise T, Dentler WL. 1998. Regulation of flagellar length in *Chlamydomonas*. *Cell Motil. Cytoskeleton.* 40, 133-146.
- Wang Q, Pan J, Snell WJ. 2006. Intraflagellar transport particles participate directly in cilium-generated signaling in *Chlamydomonas*. *Cell* 125, 549-562.
- Welch MD, Mallavarapu A, Rosenblatt J, Mitchison TJ. 1997. Actin dynamics in vivo. *Curr. Opin. Cell Biol.* 9, 54-61.
- Wemmer KA, Marshall WF. 2007. Flagellar length control in *Chlamydomonas* - a paradigm for organelle size regulation. *Int. Rev. Cytol.* 260, 175-212.
- Wilson CW, Nguyen CT, Chen MH, Yang JH, Gacayan R, Huang J, Chen JN, Chuang PT. 2009. Fused has evolved divergent roles in Hedgehog signaling and ciliogenesis. *Nature* 459, 98-102.
- Wilson NF, Lefebvre PA. 2004. Regulation of flagellar assembly by glycogen synthase kinase 3 in *Chlamydomonas reinhardtii*. *Eukaryot.* 3, 1307-1319.
- Yagi T, Uematsu K, Liu Z, Kamiya R. 2009. Identification of dyneins that localize exclusively to the proximal portion of *Chlamydomonas* flagella. *J. Cell Sci.* 122, 1306-1314.

Yang P, Diener DR, Yang C, Kohno T, Pazour GJ, Deines JM, Agrin NS, King SM, Sale WS, Kamiya R, Rosenbaum JL, Witman GB. 2006. Radial spoke proteins of *Chlamydomonas* flagella. *J. Cell Sci.* 119, 1165-1174.

Yoshimura K, Matsuo Y, Kamiya R. 2003. Gravitaxis in *Chlamydomonas reinhardtii* studied with novel mutants. *Plant Cell Physiol.* 44, 1112-1118.

You Y, Richer EJ, Huang T, Brody SL. 2002. Growth and differentiation of mouse tracheal epithelial cells: selection of a proliferative population. *Am J Physiol Lung Cell Mol Physiol.* 283, L1315-1321.

Zhang JH, Chung TD, Oldenburg KR. 1999. A simple statistical parameter for use in evaluation and validation of high throughput screening assays. *J. Biomol. Screen* 4, 67-73.

Figure 3.1

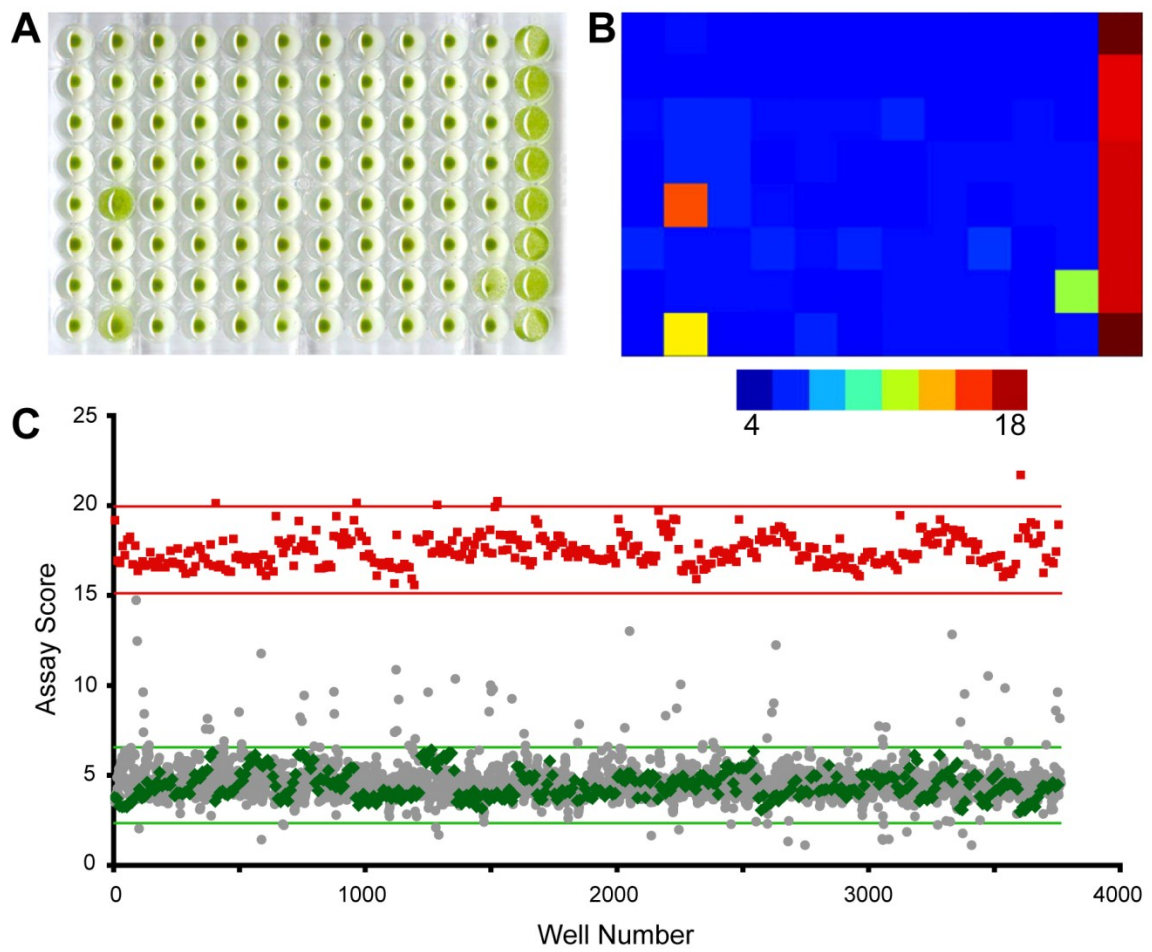
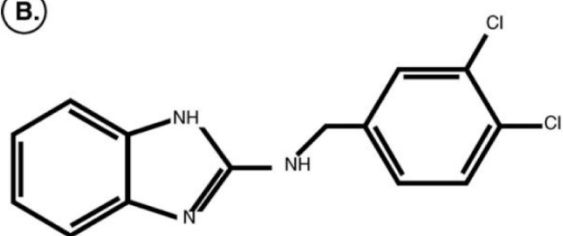
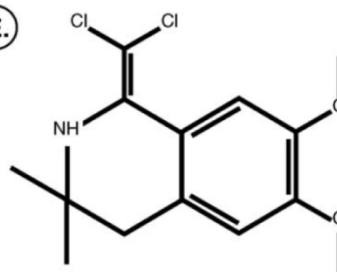


Figure 3.2

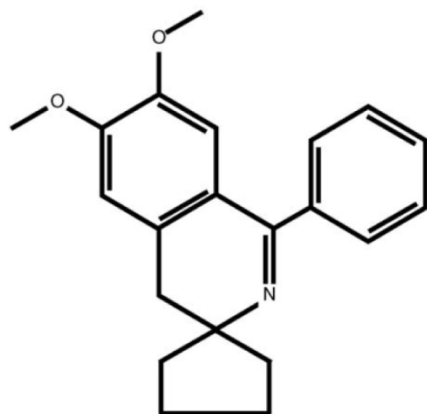
B.



E.



F.



P.

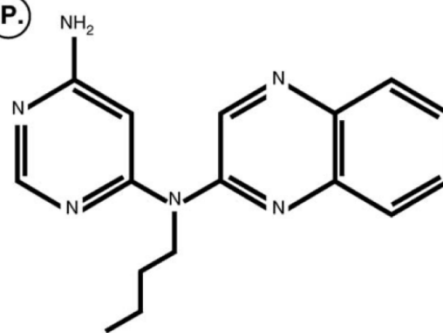


Figure 3.3

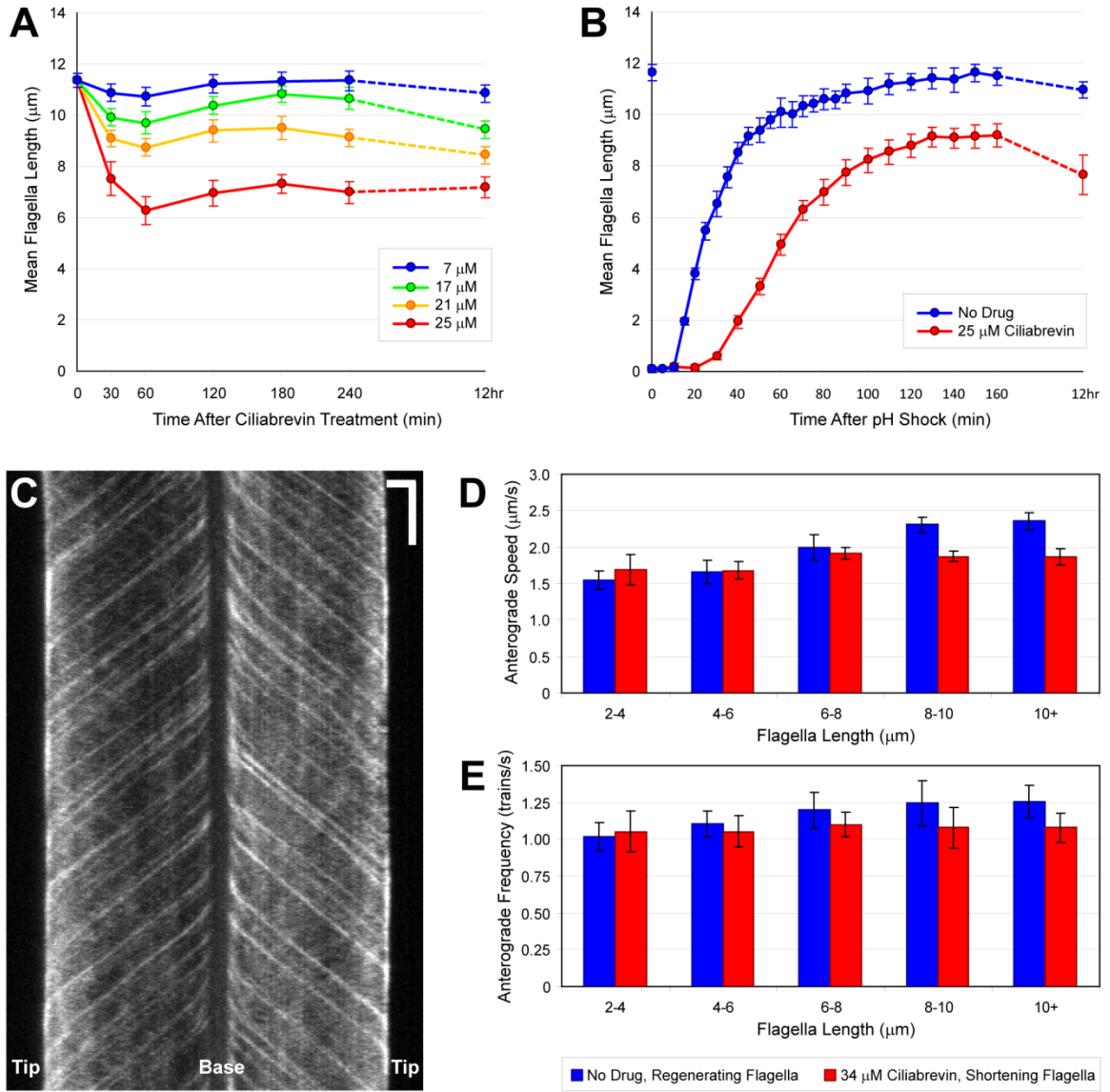


Figure 3.4

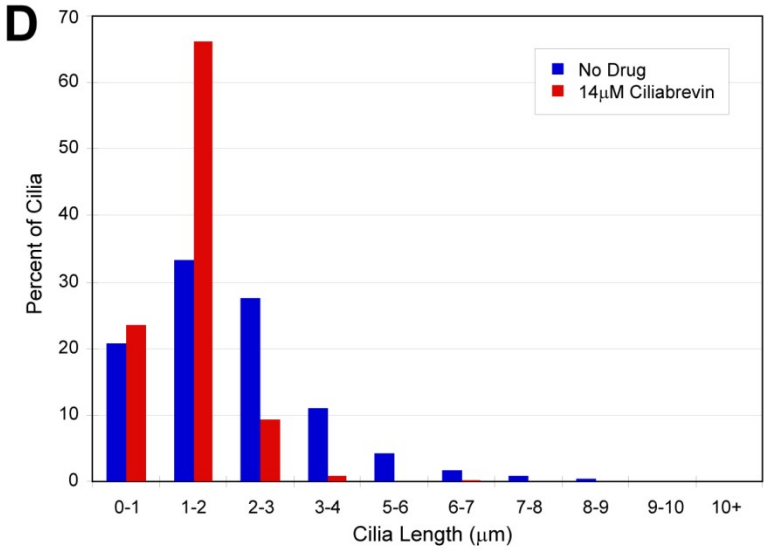
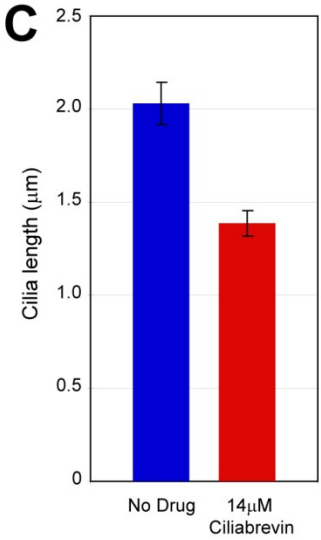
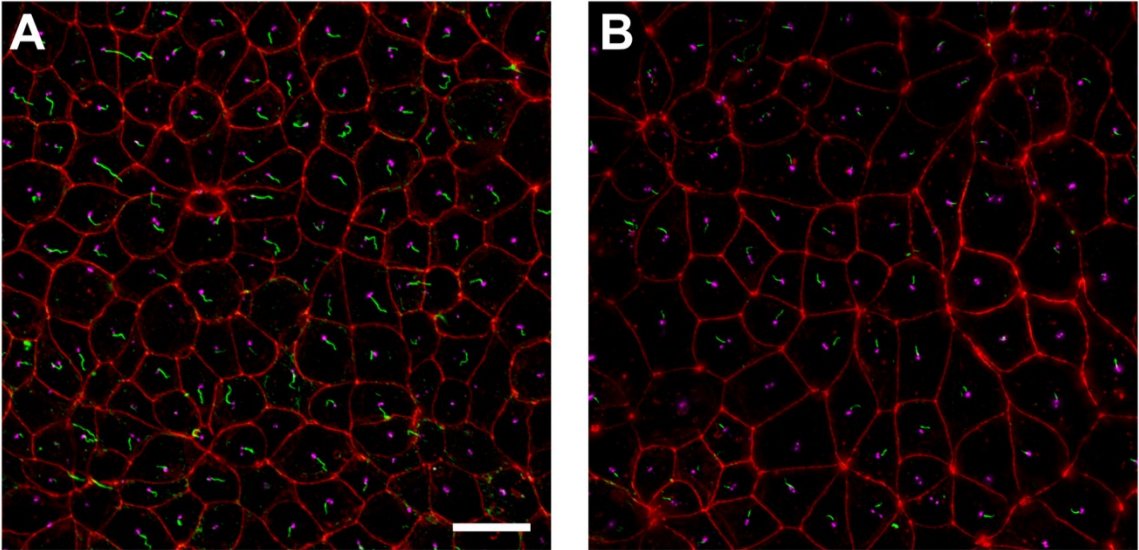


Figure 3.5

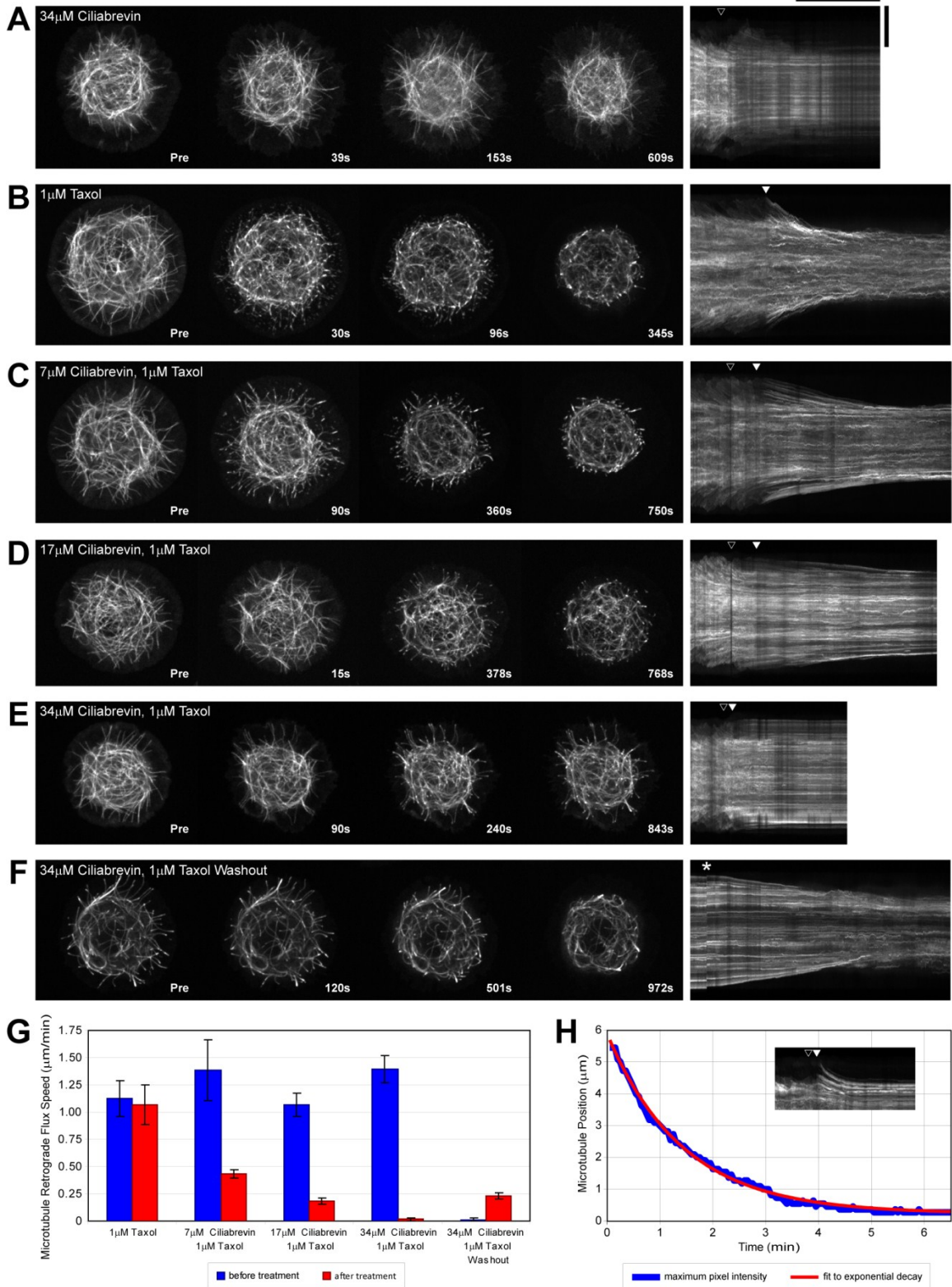


Figure 3.6

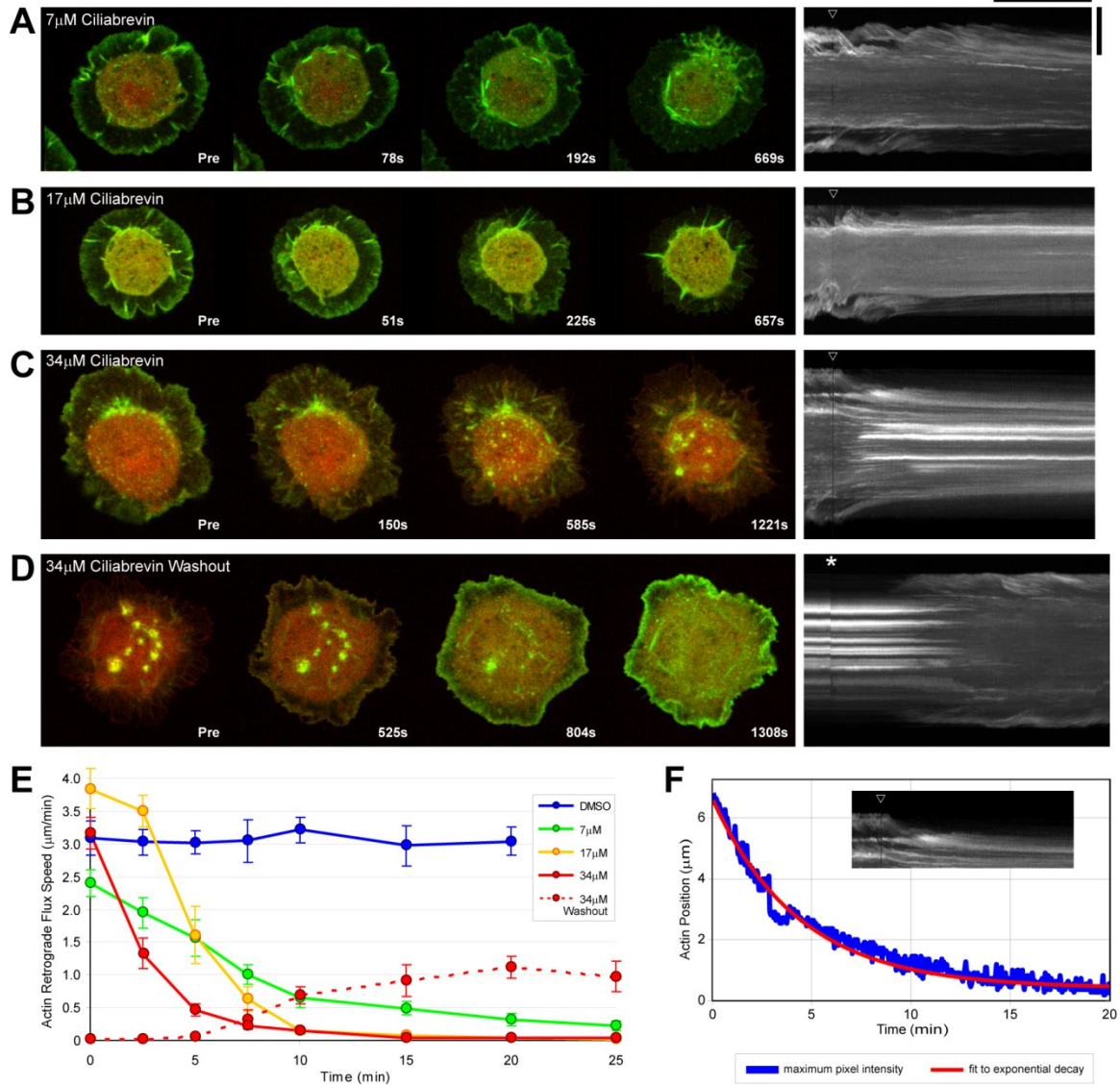
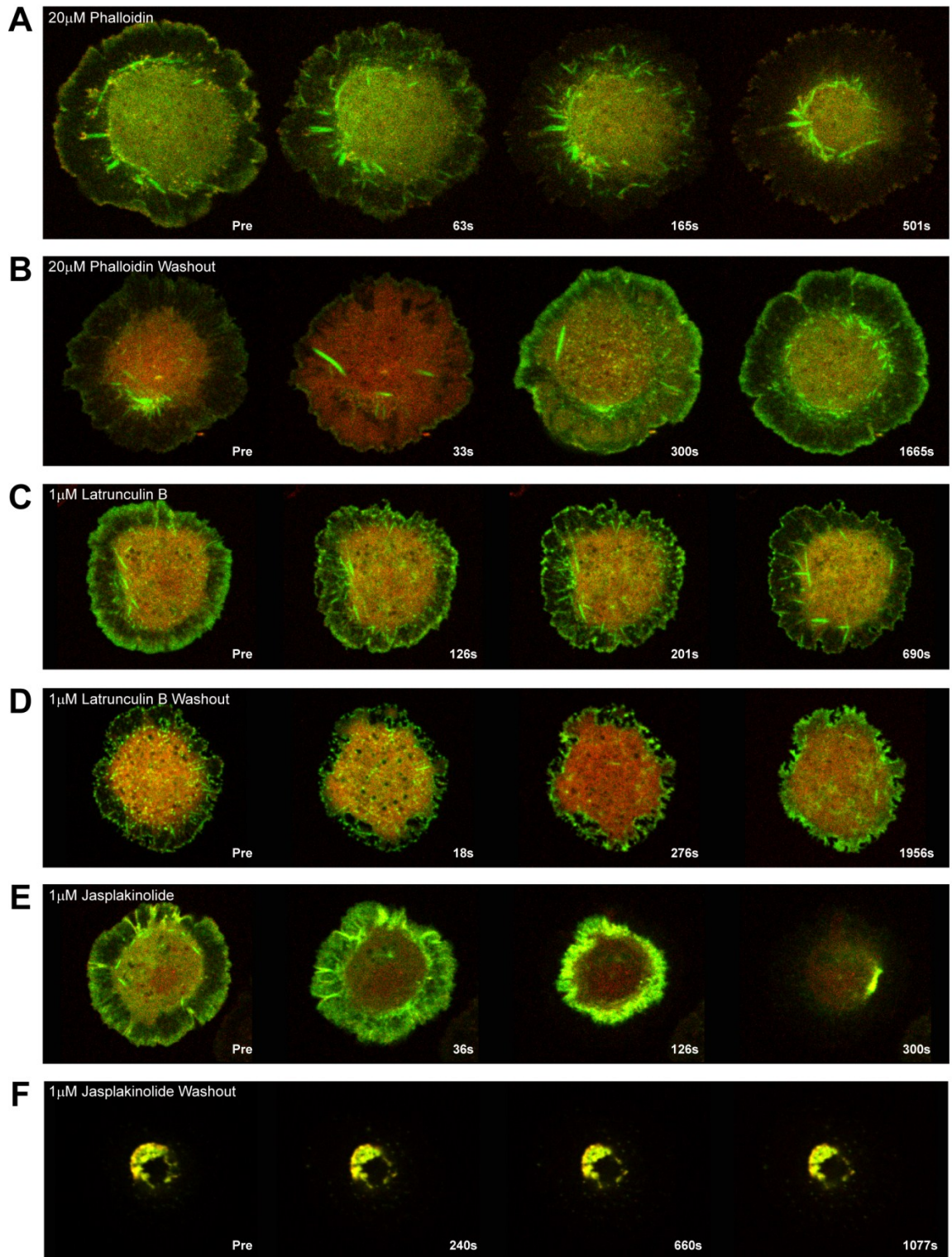


Figure 3.S1



Chapter 4

Dissecting the Roles of Retrograde Intraflagellar Transport in Flagellar Assembly and Maintenance.

Benjamin D. Engel¹, Ken-ichi Wakabayashi², Karin B. Engel³, Stefan Geimer⁴, Masafumi Hirono², Ritsu Kamiya², and Wallace F. Marshall¹

1. Dept. of Biochemistry & Biophysics, UCSF
2. Dept. of Biological Sciences, Graduate School of Science, University of Tokyo
3. Dept. Cellular and Molecular Pharmacology, UCSF
4. Dept. of Cell Biology/Electron Microscopy, University of Bayreuth, Germany

Introduction

This final chapter is distinct from the preceding sections in that it summarizes work in progress. In fact, this study includes both the oldest and newest data that I collected during my time in the Marshall lab. For my rotation project, I performed a genetic screen that yielded a single temperature-sensitive (*ts*) mutant with defects in flagellar assembly (Figure 1). While I was occupied by the studies outlined in the previous chapters of this thesis, the mutant waited patiently on my desk for years. Upon finally returning to the mutant, I was pleased to discover that it offered unique opportunities to delve further into the connection between IFT and flagellar length control.

In chapter 1, we explored the reliance of flagellar assembly and maintenance on anterograde IFT, which carries axonemal precursors such as tubulin from the cell body to their site of assembly at the flagellar tip. Retrograde IFT, which returns proteins to the flagellar base, is generally thought to also be required for assembly and maintenance of flagellar length. This conclusion is primarily based on observations of *Chlamydomonas* mutant strains with null deletions in Dhc1b (*dhc1b-1*, Pazour et al., 1999; *stf-1*, *stf-2*, Porter et al., 1999), the heavy chain of the dynein motor that powers retrograde IFT. These mutants have a typical “retrograde IFT defect”, stubby flagella swollen with IFT and axonemal proteins that have been stranded at the tip in the absence of return transport. Based on this phenotype, it was concluded that some part of the IFT system (kinesin? IFT complex A or B?) must be brought back to the flagellar base by retrograde transport in order to continue IFT-mediated flagellar assembly

and maintenance. The intrinsically coupled processes of retrograde and anterograde IFT (anterograde IFT brings retrograde proteins to the tip, retrograde IFT brings anterograde proteins to the base) must both be required for the assembly and maintenance of flagella.

However, unlike the *ts fla10* kinesin mutant that demonstrated the requirement of anterograde IFT for flagellar maintenance by dynamically shortening its flagella when the mutant was shifted to the non-permissive temperature (Kozminski et al., 2005), the swollen stubby flagella of the null Dhc1b mutants have reached an end state. It is still logical to conclude from these mutants that Dhc1b is necessary for flagellar assembly, but testing dynein's impact on flagellar maintenance would require a system where retrograde IFT could be dynamically shut off in full length flagella (a dynein version of *fla10*). As luck would have it, this is exactly the mutant that I had isolated from my screen years before (Figures 2 and 3). This mutant, which we have dubbed *dhc1b-3*, enables the inducible decoupling of retrograde IFT from anterograde transport. Surprisingly, even though anterograde IFT is strongly decreased upon temperature-shifting the *dhc1b-3* mutant (Figure 6), flagellar length is maintained for many hours until cell division, when new flagella are unable to assemble (Figure 4). This result is very different from the immediate flagellar shortening seen in *fla10*, and suggests that retrograde IFT may only be necessary for flagellar assembly but not maintenance. It will be a challenge to equate these observations with the current incarnation of the balance-point

model, which predicts that the decrease in anterograde IFT seen in the *dhc1b-3* mutant should result in flagellar shortening.

In keeping with “under construction” nature of this chapter, I will provide informal commentary on where the data needs to be improved and what additional results will be required in order to carry this story through to publication.

Comments on additional necessary work are identified by [brackets] and are included in both the results the figure legend sections.

Results and Discussion

We performed UV mutagenesis followed by a phenotypic screen for temperature-sensitive defective cell motility in *Chlamydomonas* (Figure 1A). Of the 122 punctate colonies isolated for further screening, 68 were bald, 13 had jerky swimming, 6 were paralyzed, 17 were sick, and 18 swam normally (assay false hits). Only 3 isolates had *ts*-motility defects. Two strains exhibited *ts*-paralysis and were not further studied, while a single strain showed a robust and reversible defect in flagellar assembly. At 21C, this mutant strain had full-length flagella containing a regular distribution of IFT proteins (Figure 1B) and appeared to have no defects in axoneme or basal body ultrastructure (Figure 1E). However, after a day at 34C, IFT proteins accumulated in flagella (Figures 1C and 1F) and eventually flagella became stumpy and swollen with IFT material (Figures 1D and G). These stumpy flagella persisted until cells were shifted back to 21C, at which temperature flagella regrew after several hours. The accumulation of IFT proteins in our mutant flagella at the non-permissive

temperature was typical of a retrograde IFT defect and was highly reminiscent of null mutants in Dhc1b, the heavy chain of the retrograde dynein motor (*dhc1b-1*, Pazour et al., 1999; *stf-1*, *stf-2*, Porter et al., 1999), which have stumpy swollen flagella.

We analyzed the flagellar accumulation and depletion of IFT proteins by immunofluorescence (Figures 2A and 2B) and western blots of isolated flagella (Figure 2C). Immunofluorescence showed a depletion of Dhc1b within the mutant flagella at both 21C and 34C, while the dynein light-intermediate chain D1blic was only severely depleted in the mutant at 34C. IFT complex B protein IFT81 was depleted in mutant flagella at 21C but accumulated at 34C, while IFT complex A protein IFT139 only showed accumulation in the mutant at 34C. Levels of KAP, a component of the anterograde kinesin motor, were not greatly changed in the mutant. Many of these immunofluorescence observations were confirmed in the western blots (Figure 2C). Most strikingly, Dhc1b was strongly depleted in mutant flagella at 21C and nearly absent at 34C. D1blic showed similar depletion to Dhc1b, although the reductions were slightly less severe. Taking into account the uneven tubulin loading (gels were loaded with equal protein, which did not equate to an equal number of flagella due to protein accumulation), IFT81, IFT140, and IFT122 show moderate accumulation upon temperature shifting the mutant, while KAP and BBS4 may not change. [*This experiment must be repeated with equal tubulin loading instead of equal protein loading to enable quantification of moderate IFT changes. Additional IFT antibodies including IFT139 and IFT27 should also be used*]. Interestingly, the

mutant also experienced a cytoplasmic accumulation of IFT140 and axonemal protein IC69 that was not present in wild-type cell bodies (Figure S1).

We monitored the expression of the corresponding IFT and axonemal protein genes by quantitative PCR (qPCR, Figure 2D). While the expression of many genes was unchanged, the mutant had increased levels of Dhc1b, D1blic, and IFT81 transcripts, particularly once cells were shifted to 34C. One compelling hypothesis is that the up-regulation of Dhc1b and D1blic transcription is a feedback loop attempting to compensate for loss of these proteins (seen in Figure 2A-2C), while the increase in IFT81 mRNA has been triggered by the sequestration of IFT81 protein in flagella due to defective retrograde transport.

[This qPCR experiment requires two additional replicates to be considered reliable. Materials have been paid for the Marshall lab to use the Yamamoto lab qPCR machines. I have additional validated primers for more genes of interest (see Table S1). The link between IFT defects and transcription could be a compelling research project, but it will not be covered much in this story].

We were immediately aided in linkage mapping of the mutation by the observation that the mutant phenotype is tightly linked to the mating-type locus on linkage group VI. To perform higher resolution mapping, we crossed the mutant to the S1D2 polymorphic strain and performed PCR of the tetrad progeny to check for recombination between the mutation and several genetic markers (Figure 3A). This analysis tracked the mutation to a small region at the end of linkage group VI. Among the 6 potential flagellar genes in this region was Dhc1b, our leading candidate based on depletion of the protein, accumulation of

the mRNA, and phenotypic similarities to the null *dhc1b-1* strain. Sequencing Dhc1b cDNA from the mutant revealed a single base-pair mutation at 12313bp in the coding sequence (Figure 3B). This A to T substitution results in a single amino acid switch from Isoleucine to Phenylalanine at position 4105 of the amino acid sequence. The mutation occurs in the middle of a conserved hydrophobic motif and presumably impedes protein folding, especially considering the depletion of dhc1b protein (Figure 2A-C) and accumulation of mRNA transcript (Figure 2D), both of which are exasperated by the temperature shift. In order to genetically track this mutation, which we named *dhc1b-3*, we developed an assay using PCR and restriction digestion (Figure S2).

Although several characterized mutants strains, such as *fla10*, have temperature-sensitive defects in flagellar assembly, the kinetics of flagellar loss in *dhc1b-3* are strikingly different. While *fla10* flagella begin shortening immediately at 34C and are lost within 5 hours (Figure 4E), *dhc1b-3* cells maintain full-length flagella for over a day at 34C before finally losing them (Figure 4A). Flagellar loss in *dhc1b-3* appears to be timed with cell division, both in synchronized cell cultures (Figures 4B and 4C) and in cells induced to undergo gametogenesis (Figure 4D). Thus, we concluded that while dynein-powered retrograde IFT is needed for flagellar assembly, it differs from anterograde IFT in that it is not required for the maintenance of flagellar length. *fla10/dhc1b-3* cells show the same kinetics of flagellar loss as *fla10* single mutants (Figure 4E), demonstrating that anterograde IFT defects are epistatic to retrograde IFT

defects. [*The synchronized division experiment should be repeated with measured flagellar lengths to match the rest of this figure*].

Interestingly, at 21C *dhc1b-3* flagella have the same regeneration kinetics following pH shock as wild-type flagella (Figures 5A and 5B), despite containing significantly less dynein protein (Figure 2C). In light of this observation, it is puzzling what function the extra IFT dynein serves in flagella, as it is not necessary for flagellar assembly. One conjecture is that it aids in signal transmission from the flagellum to the cell body. On the other hand, this protein may simply be surplus. When *dhc1b-3* are incubated at 34C following pH shock, they do not regenerate flagella (Figure 5C). This result is consistent with the lack of flagellar assembly following *dhc1b-3* cell division at 34C (Figure 4). It also implies that *dhc1b-3* flagellar assembly requires production of new Dhc1b protein. To investigate this hypothesis, we allowed mutant cells to regenerate flagella at 21C after increasing periods of pre-shock incubation at 34C (Figure S3). Regeneration after 6hrs and 12hrs at 34C was only delayed by 10 minutes and proceeded at a slightly slower rate. Presumably, this delay is the time it takes for mutant cells to produce new functional Dhc1b protein at 21C. After 18hrs at 34C, the regeneration delay became longer and the growth kinetics were substantially slowed. In summary, mutant *dhc1b-3* cells can only assemble new flagella at 21C, but they do so at a rate equal to wild-type cells despite reduced flagellar Dhc1b levels. [*These experiments should be repeated with flagellar length measurements. The effects of dhc1b-3 on IMBX-induced*

flagellar shortening and LiCl-induced lengthening would also be interesting additions to this figure].

Given the dramatic reductions in dynein levels and unique kinetics of flagellar loss in *dhc1b-3*, it is of key interest to measure anterograde and retrograde IFT in the mutant at 21C and 34C and correlate these measurements with the predictions of the balance-point model. At present, we have only performed preliminary experiments, but the data is intriguing. Despite possessing reduced flagellar levels of dynein protein, the mutant at 21C had the same anterograde IFT speed and frequency as wild-type cells (Figures 6A and 6B). This result is consistent with the wild-type regeneration kinetics of mutant flagella at 21C (Figure 5) and again begs the question of what function the extra dynein is performing in flagella, if not powering IFT. However, after *dhc1b-3* cells were incubated at 34C for 14hr, they showed a dramatic reduction of anterograde IFT speed and frequency. This result is potentially in conflict with the balance-point model, which predicts that reduced anterograde IFT will result in shorter flagella. Instead, *dhc1b-3* flagella are maintained at full-length at 34C, despite severe reductions in IFT. *[This experiment should be repeated with KAP-GFP dhc1b-3 cells at a range of 34C timepoint, as well as a 34C wild-type KAP-GFP control. IFT should also be measured using DIC optics, both to confirm the KAP-GFP anterograde measurements and to quantify retrograde IFT. Unlike the right panel in figure 6, future imaging of cells that were pre-incubated at 34C should be carried out at 34C and not room temperature. Completing these imaging experiments is my primary focus in the summer of 2011].*

While retrograde IFT may not be necessary for the maintenance of flagellar length, it appears to be required for the maintenance of flagellar function. When incubated at 34C, *dhc1b-3* cells swim slower (Figure 7D) and switch from mild negative phototaxis to strong positive phototaxis (Figures 7A-7C), while control cells maintain their phototactic direction and swimming speed at both 21C and 34C. Furthermore, the beat frequency of mutant flagella is decreased at both 21C and 34C (Figure 7E), a telltale sign of an axonemal outer dynein arm (ODA) defect. Because this beat frequency reduction manifests in permeabilized ATP-reactivated cell models in addition to live cells, it is likely caused by a structural defect in the axoneme (though we could not find an obvious deficiency in TEM cross-sections of mutant axonemes; data not shown). Thus, it seems quite plausible that dynein-mediated retrograde IFT helps maintain both physical and signaling flagellar functions of by removing old turnover products, enabling flagella to be refreshed with new proteins. *[This figure would benefit from scoring the efficiency of mating, another flagellar signaling function, in mutant and wild-type cells at 21C and 34C. Also, phototaxis assays should be performed with the parental wt cc125 strain from which the dhc1b-3 mutant was generated].*

Lastly, we decided to take a non-biased proteomic approach to catalog the accumulation and depletion of proteins within *dhc1b-3* flagella in the hopes of identifying new cargos and interacting partners for retrograde IFT. We isolated flagella from cc125 wild-type cells at 21C, *dhc1b-3* cells at 21C, and *dhc1b-3* cells at 34C. We then employed the services of Applied Biomics (Hayward, CA) to perform 2D-DIGE analysis, where each sample was conjugated to a different

cy-dye, all three samples were separated by mass and charge on the same 2D gel (Figure 8, top panel), and the change in abundance of individual protein spots between the samples was quantified. We picked the spots with the greatest changes for identification via mass spectrometry (Table 1). While parsing this type of data is intrinsically complicated, several distinct trends and promising candidate proteins presented themselves when the identified spots were clustered into profiles based on accumulation or depletion between the three samples (Table 1 and Figure 8, bottom panel).

FAP103 and FAP162 are repeatedly found among the top hits in the “D1” and “D2” profiles (proteins that are depleted from *dhc1b-3* flagella at 34C and at both 21C and 34C, respectively). Particularly since these two proteins are exclusively found in the “membrane + matrix” fraction, I would predict that FAP103 and FAP162 both interact with dynein in order to enter flagella. They could be uncharacterized components of the dynein motor, IFT proteins, or obligate cargo of the retrograde machinery. FAP55, FAP127, FAP189/FAP58, and FAP166 are all axonemal proteins with very similar “D1” profiles, so chances are that at least some of these structural proteins preassemble together into a larger complex before being carried into flagella by IFT.

The “D3” profile (depleted at 21C but not 34C) is home to the IFT complex B proteins IFT81, IFT80, and IFT27. The increase in IFT81 abundance when mutant flagella are shifted to 34C agrees with our immunofluorescence and western blot measurements in Figure 2. Other proteins that group tightly into this profile may interact with IFT complex B as obligate cargos. Of particular interest

is elongation factor 1A1 (EF1A1), a protein that interacts with the cytoskeleton to regulate translation efficiency (Zhang et al., 2009). Although EF1A1 has a predicted molecular weight of 50 kDa, the spot is at 100 kDa and was also identified as a perfect hit for alpha-tubulin (50kDa). There is a possibility that an EF1A1-tubulin dimer (that is so stable that it is not separated by SDS-PAGE) traffics in flagella along with IFT complex B. If this is true, one could envision several fanciful models where the cell could couple the abundance of EF1A1 in the cytoplasm, directly affected by sequestration of EF1A1-tubulin in the flagellum, to the translation efficiency of flagellar components such as tubulin. In addition to EF1A1, CAH6 and the protofilament ribbon protein Rib43a are strong candidates for IFT complex B cargos in the “D3” profile.

IFT122B (also known as IFTA-1) is a well-characterized cargo adaptor component of IFT complex A. It is found in the “A1” profile, which is only accumulated in mutant flagella at 34C. This is consistent with the accumulation of IFT complex A protein IFT139 that we measured in Figure 2, as well as the idea that the depletion of dynein at 34C is stranding IFT proteins and the turnover products that they carry in the flagellum. IFT122B also has the opposite accumulation profile as calmodulin, which is found in “D1”. This may provide some hint about how calmodulin is transported in flagella. Other proteins in the “A1” and “A2” profiles (accumulated in *dhc1b-3* flagella at 34C and at both 21C and 34C, respectively) are likely proteins that are ordinarily trafficked by retrograde IFT out of the flagella. These proteins include axonemal components such as ODA1, ODA9, KLP1, FAK1, RSP16, RSP3, FAP7, FAP219, as well as

the “membrane + matrix” proteins CAH6 and AGG3. The accumulation of ODA proteins may be indicative of defects in the outer dynein arms that could underlie the observed reduction in flagellar beat frequency (Figure 7E). The accumulation of AGG3 is interesting as it may explain the change in phototaxis direction (Figure 7A-C). AGG3 RNAi induces the same phenotype as the *agg1* mutant, where cells swim away from light (Iomini et al., 2006). Thus, it is logical to hypothesize that the flagellar accumulation of AGG3 that occurs in *dhc1b-3* could cause a switch to positive phototaxis.

Profile “A3” is a group of proteins that were accumulated in mutant flagella at 21C but not 34C. This profile has the opposite abundance as the IFT complex B proteins in “D3”. Most of the “A3” proteins are uncharacterized (FAP12, FAP215, FAP31, FAP43, FAP203, BUG13, FAP57, FAP252/BUG10, FAP18) and many are in the “membrane + matrix” fraction. One well-characterized protein in the group is EB1, a +TIP protein that stabilizes the plus ends of microtubules. More EB1 at the flagellar tips could help compensate for reduced IFT complex B transport by increasing axoneme stability (hence, the inverse accumulation from profile “D3”). There is a poorly understood structure at the tip of the flagellum known as the “flagellar cap complex” that presumably regulates the incorporation and removal of proteins from the axoneme. EB1 is one of the flagellar cap’s only identified components, so it would be of great interest if any of the uncharacterized proteins in the “A3” profile were also part of this mysterious structure.

The final profile, “NC”, is a group of proteins that did not change in abundance between the three samples. Since sample loading was normalized for equal tubulin, unsurprisingly many of the “NC” proteins were axoneme structural components. The two spots that changed the least were flagellar actin (IDA5). As a loading control, the relative accumulation or depletion of every other protein spot was normalized to the average of the two IDA5 spots. Less expected were the unchanging levels for IFT88 and IFT81. While IFT88 was only found in the “NC” profile, additional IFT81 spots were found in the “D3” profile with other IFT complex B proteins. This separation between multiple spots of the same protein is both a strength and challenge of 2D gel proteomics. While this resolution can provide the opportunity to monitor changes in modified sub-populations of proteins, it can be difficult to tell how the total abundance of a given protein changes (all the spots combined) without independent western blot assays requiring specific antibodies. For example, while two different spots for the protofilament ribbon protein Rib43a are found in “NC”, another spot is in the “D3” profile along with the IFT complex B proteins. The “NC” spots are far more abundant than the “D3” spot (Figure 8) and they have acidic shifts of -0.3pH and -0.6pH that are likely the result of phosphorylation. I predict that the “D3” Rib43a spot is an unphosphorylated IFT cargo, and that once this cargo is incorporated into the axoneme (and becomes an “NC” spot) it acquires modifications such as phosphorylation. If true, phosphorylation of Rib43a would provide a tractable mark for distinguishing between an axonemal cargo that is being carried to the tip by anterograde IFT and protein that has been already been incorporated into the

axoneme (similar to the difference between the intermediate 12S and mature 20S radial spoke complexes; Qin et al., 2004). It may in fact be a more general feature of the axoneme that proteins are phosphorylated after they are assembled into the structure. Of course, each of the predictions proposed in this discussion would have to be checked with secondary experiments. [*The levels of protein accumulation in the 2D-DIGE need to be verified by western blot. To this end, we have recently acquired antibodies to ODA1, IDA5, RSP1, RSP3, Rib43a, AGG2, AGG3, EB1, and IFT27*].

The burning question that remains is why *dhc1b-3* flagella are maintained, despite severe reductions in IFT. At first glance this result conflicts with the balance-point model. Perhaps modifications can be made to full-length flagella that “lock down” flagellar dynamics, effectively dropping the assembly and disassembly rates to zero, regardless of IFT. If this is the case, IFT measurements (such as those in chapter 1) are only a useful metric to predict flagellar length outcomes in regenerating flagella. This hypothesis does not agree with the *fla10* mutant’s flagellar shortening and loss, but perhaps something is happening in the *fla10* strain that prevents the normal stabilization of full-length flagella. Another possibility that may mesh with the balance-point model is that in the absence of retrograde IFT, axonemal components that come off the flagellar tip might immediately reassemble since they are not removed, thus maintaining a high local concentration of axonemal precursors at the site of assembly. The key to unraveling this mystery will likely be found in the differences between *dhc1b-3* and *fla10*, specifically at the tips of their flagella.

Although both mutant strains experience reduced IFT at the non-permissive temperature, only *fla10* loses its flagella. Something different must be occurring at the tips of *dhc1b-3* axonemes to enable their retention in the absence of IFT.

Figure Legends

Figure 1. *Genetic screening strategy and temperature-sensitive*

“retrograde IFT” phenotype of isolated mutant strain. (A) Genetic screen for temperature-sensitive motility mutants in *Chlamydomonas*. Liquid cultures were exposed to UV light at a dose sufficient to kill 90% of cells (8 minutes using our tissue culture hood setup). The cultures were then diluted into low concentration agar (.35%) and grown for one week in fluorescent light at 34C (the non-permissive temperature), resulting in embedded clonal colonies. While motile colonies became diffuse, colonies with motility defects remained punctate. Punctate colonies were picked out of the soft agar, grown in 96-well plates at 34C, and then replica plated to additional 96-well plates at both 34C and 21C and examined by microscopy for temperature-sensitive motility phenotypes. (B-D) Immunofluorescence and (E-G) transmission electron microscopy (TEM) of the *ts*-flagellar assembly mutant. Green= IFT139, red= IFT172, blue= DNA. At 21C, the mutant appeared to have a regular distribution of IFT particles along the flagella (B) and showed no discernable defects in axoneme or basal body ultrastructure (E). After 24 hours at 34C, flagella were either long (C) or stumpy (D) and in both cases showed a strong accumulation of IFT protein. This accumulation of IFT protein at 34C was also apparent by TEM (F, G) as a buildup of electron-dense material between the axoneme and the flagellar membrane.

Figure 2. mRNA and flagellar protein accumulation and depletion in the *ts-flagellar assembly mutant*. (A) Immunofluorescence staining for Dhc1b, D1blic, KAP, IFT81, and IFT139 in wild-type cells at 21C and mutant cells at 21C and 34C, as indicated in the figure. (B) Quantification of flagellar fluorescence in the mutant at 21C and 34C relative to wild-type at 21C, normalized for background intensity of the images. Dhc1b fluorescence was depleted in the mutant strain at both 21C and 34C, while D1blic was only depleted at 34C. IFT81 was depleted in the mutant at 21C but accumulated at 34C. IFT139 had wild-type intensity in the mutant at 21C but was greatly accumulated at 34C. KAP fluorescence remained relatively unchanged between the wild-type and mutant strains. (C) Western blots of isolated flagella from wild-type 21C, mutant 21C, and mutant cells incubated for increasing time at 34C. IC69, alpha-tubulin, and acetylated tubulin are axonemal proteins that serve as loading controls. Gels were loaded with equal total protein, but due to protein accumulation in mutant flagella at 34C, the loading controls are uneven. Dhc1b and D1blic were greatly depleted in the mutant, especially at 34C. Taking in consideration the unequal axoneme loading, IFT81, IFT140, IFT122 appeared to show moderate accumulation upon temperature shifting the mutant. [*This experiment must be repeated with a wt 34C sample, equal tubulin loading, and additional IFT antibodies*]. (D) Quantitative PCR (qPCR) of cDNA from wild-type and mutant strains at 21C and 34S. The data was normalized to the rubisco housekeeping genes RbcL and RbcS2A and plotted as fold change relative to the wild-type 21C sample. Dhc1b, D1blic, and IFT81 expression were up-regulated, while other IFT and axonemal

genes were not greatly changed. [*This experiment requires two additional rounds of qPCR to generate error bars and confirm reproducibility. Primers for additional genes have been designed and validated for qPCR (see Table S1)*].

Figure 3. Linkage mapping of *ts*-flagellar assembly mutant and sequencing

of a single base-pair mutation in *Dhc1b*. (A) The mutant phenotype was mapped to the end of linkage group VI by mating the mutant to polymorphic strain S1D2, performing tetrad dissection, and scoring the recombination frequency of the progeny by PCR. Genes listed in blue produce proteins that localize to flagella (Pazour et al., 2005). This analysis also yielded a mating-type minus (*mt*-) mutant strain that can be used to produce a diploid strain with the *dhc1b-1* null dynein mutant (Pazour et al., 1999). (B) The entire *Dhc1b* cDNA was sequenced including parts of the 3' and 5' UTRs (see primers in Table S2), revealing a single base pair substitution at 12313bp in the coding sequence. This A to T mutation occurs at the first base pair in the codon, substituting a single amino acid (Isoleucine to Phenylalanine at residue 4105). The mutation occurs in the middle of a conserved hydrophobic motif and presumably impedes protein folding. We named the *ts* mutant "*dhc1b-3*". [*Producing and phenotyping a *dhc1b-3/dhc1b-1* diploid strain is required to show non-complementation between the conditional and null alleles. This figure should also include a diagram of *Dhc1b* protein domains and a sequence alignment of exon 42 with important species such as *c. elegans* and humans and showing the *Ile* to *Phe**

switch at amino acid 4105 of the 4333AA sequence. The mutation occurs downstream (further C-terminal) from the six AAATPase motifs].

Figure 4. Kinetics of *dhc1b-3* flagellar loss in vegetative cells, synchronized dividing cells, during gametogenesis, and in *fla10/dhc1b-3* double mutants. Bar graphs depict the percentage of deflagellated cells, while line graphs show the average flagellar length of flagellated cells (error bars= standard deviation). (A) Vegetative wild-type and *dhc1b-3* cell grown for two days at 21C and then shifted to 34C. Mutant cells lose flagella at 36hrs at 34C (In previous experiments flagellar loss was observed beginning at 24hr 34C. This may depend on the growth phase of the culture). (B-C) Cells were synchronized by G1 growth arrest in M1 media in the dark for 12hr and then released into TAP media in the light. (B) At 21C, both wild-type and mutant cultures went through a semi-synchronized cell division at 24-30hr (~50% deflagellated and clumpy cells). Following cell division, cells in both cultures regrew flagella. (C) At 34C, wild-type cells regrew flagella following cell division, but mutant cells were deflagellated. This implies that the *dch1b-3* mutant can maintain old flagella at 21C and 34C, but can only assemble new flagella at 21C. (D) Vegetative cells were grown in TAP media at 21C for one day, incubated for increasing periods of time at 34C, and then induced to divide synchronously into gametes by resuspending the cells in M-N media at 34C for 18hrs. Pre-incubation for 4-8hr at 34C inhibited flagellar assembly in *dhc1b-3* gametes, again suggesting that this mutant strain cannot assemble new flagella at 34C. (E) *fla10* and

fla10/dhc1b-3 double mutants had the same kinetics of flagellar shortening and loss. Thus, inhibiting anterograde IFT is epistatic to inhibiting retrograde IFT. The *fla10* flagellar loss kinetics were much quicker than the kinetics of *dhc1b-3* in panel A because anterograde transport is required for the maintenance of flagellar length in addition to flagellar assembly. [The cell synchronization should be repeated with flagellar length measurements in addition to the %bald metric. For efficient synchronization, keep cultures dilute and in log growth phase during dark arrest and after shifting to light. The experiments in panels A, B, & C can also be repeated with the *mt-* mutant strain for robustness].

Figure 5. Kinetics of flagellar regeneration following pH shock in wild-type and *dhc1b-3* at 21C and 34C. At 21C, mutant cells regenerated their flagella at the same rate as wild-type cells (top and middle panels). This is particularly striking given the decreased abundance of Dhc1b protein in mutant flagella (Figure 2). However, mutant flagella are unable to regenerate at 34C (bottom panel), implying that production of new Dhc1b protein is required for assembly of mutant flagella. This result is consistent with mutant cells not regrowing flagella following cell division at 34C (Figure 4C). In this experiment, flagellar length was judged and binned visually as “deflagellated”, “stumpy” (~1-3 μ m), “short” (~3-7 μ m), and “full length” (> ~7 μ m). [This experiment should be repeated with flagellar length measurements and with an additional wt 34C control. Effects of the *dhc1b-3* mutation on LiCl-induced lengthening and IBMX-induced shortening could also be added to this figure].

Figure 6. Intraflagellar transport in wild-type and *dhc1b-3* at 21C and 34C.

(A) Kymographs and (B) quantification of TIRF imaging of *dhc1b-3*/KAP-GFP cells at 21C and after 14hrs at 34C, as well as a wild-type KAP-GFP 21C control. Despite the low abundance of Dhc1b protein (Fig 2), the speed and frequency of anterograde IFT in the mutant at 21C was the same as wild-type. However, after 14hr at 34C, there was a significant reduction in anterograde IFT in the mutant. This observation is difficult to equate with the balance-point model, as flagellar length remains unchanged (Figure 4). This imaging was performed at room-temperature, so it is possible that IFT in the mutant at 34C should actually be further reduced and that this experiment is instead observing the restoration of IFT upon shifting cells back to the permissive temperature. Note the “squiggly back and forth” motion of the retrograde KAP-GFP traces in the mutant 34C kymograph. This is the first time such motion has been observed, as KAP-GFP normally has bright background fluorescence and very few retrograde traces. *[This experiment requires a wider range of KAP-GFP mutant 34C timepoints and a wt 34C control. It also requires high resolution DIC imaging at the same timepoints to complement the TIRF and to visualize retrograde IFT. Unlike the data currently presented in this figure, future imaging of cells that have been incubated at 34C should also be performed at 34C to prevent the relatively rapid recovery of Dhc1b protein production. However, as evidenced by the mutant 34C kymograph in this figure, visualizing the initial events in IFT recovery could be quite informative, particularly in observing the retrograde motion of KAP-GFP].*

Figure 7. Phototaxis, swimming speed, and flagellar beat frequency in wild-type and *dhc1b-3* at 21C and 34C. (A-C) Dish assays and single cell tracking of phototactic direction (sign) in response to a green light source (from the right). Left panels show dish assays, where bulk phototaxis can be ascertained by non-uniform changes in culture density (greenness). Right panels show compass plots of the percent of cells with given phototactic directions, measured by video microscopy and hand-tracing of single-cell trajectories. “wt 137c”= positive phototaxis control, “wt cc124”= *agg1* negative phototaxis control, “*bbs4* null”= control for an IFT defect that inhibits phototaxis (Lechtreck et al., 2009), “mutant”= *dhc1b-3*. The *dhc1b-3* strain shows a reversal in sign from mild negative to strong positive phototaxis upon incubation at 34C. Cells were “primed” for 15 minutes in uniform red light prior to directional green light illumination. (D) Incubation of the *dhc1b-3* mutant at 34C for 12hrs severely decreases cell swimming speed (measured by video microscopy), indicating a potential flagellar defect. (E) Flagellar beat frequency is reduced *dhc1b-3* at both 21C and 34C (method, described in Kamiya and Hasegawa, 1987, involves measuring the fast Fourier transform of a dark-field microscopy signal). The beat frequency is reduced in both live cells and ATP-reactivated permeabilized cells (reactivated cell models), indicating that the reduced frequency is likely due to a structural defect in the axoneme, perhaps in the outer dynein arms (ODAs). [The data in this figure was contributed by Ken-ichi Wakabayashi and may be

final. However, there is some concern that there is no phototaxis control for the wt cc125 parental background strain from which the dhc1b-3 mutant was made].

Figure 8. 2D-DIGE proteomic analysis of flagellar protein accumulation and depletion in wild-type 21C vs. mutant 21C vs. mutant 34C. 100-200 μ g of isolated flagella from each sample, with adjusted concentrations for equal alpha-tubulin loading (tested by LI-COR quantification of western blots), were sent to Applied Biomics (Hayward, CA) for 2D-DIGE, where they were conjugated to different cy-dyes and separated on a 2D gel, enabling simultaneous comparison of protein abundance between three samples. Spots were picked for mass spectrometry identification based on high relative accumulation or depletion between the three samples. Images of the 2D gel, with indicated green/red comparisons of the samples, are shown in the top panel. The large yellow spot is tubulin. Spot numbers (blue= accumulated, red= depleted) and their corresponding protein IDs are overlaid on the left and middle gel pictures, respectively. In the bottom panel, the spots were manually clustered by relative abundance of mut21C/wt21C (blue bars), mut34C/wt21C (red bars), and mut34C/mut21C (green bars). The spots fit into distinct profiles of proteins that were depleted in *dhc1b-3* flagella at 21C (D3), depleted at 34C (D1) or both (D2), or accumulated in *dhc1b-3* flagella at 21C (A3), accumulated at 21C (A1) or both (A2). Proteins that group together in the same profile may share similar functions (for example, IFT complex B proteins all cluster into profile D3). Additional proteins not displayed on the chart showed no change (NC), including two

flagellar actin (IDA5) spots that were used to as a control to normalize the abundance of all of the other proteins on the gel. Comprehensive information about each spot is listed in Table 1, grouped by accumulation/depletion profile. Cut-off for classification as “NC”: $|\text{mut34C} / \text{mut21C}| < 0.5$, or $|\text{mut21C} / \text{wt21C} - \text{mut34C} / \text{wt21C}| < 0.5$. On the chart y-axis, 0= no change between samples, 1 and -1= 2-fold change, 2 and -2= 3-fold change, etc. *[An additional figure is needed using western blots to verify the accumulation profiles of several of the proteins identified by 2D-DIGE. In preparation for this experiment, which will require new isolated flagella, we have recently acquired antibodies to ODA1, IDA5, RSP1, RSP3, Rib43a, AGG2, AGG3, EB1, and IFT27]*

Figure S1. Accumulation of IFT and axonemal proteins in *dhc1b-3* cell bodies. Western blots of wild-type and mutant cell body fractions after flagella were removed for purification. While IFT81 (complex B) levels are unchanged, IFT140 (complex A) and IC69 (cargo) show an unexpected accumulation in mutant cell bodies, with IC69 accumulation becoming more pronounced as mutant cell were incubated for greater periods of time at 34C. *[Many antibodies that worked for isolated flagella did not detect anything in cell body lysate, where the flagellar proteins are much more dilute. Regardless, it would be interesting to see if other proteins show accumulation similar to IC69 and IFT140].*

Figure S2. PCR scheme for rapid verification of *dhc1b-3* point mutation.

(A) The forward primer is ~100bp upstream of the mutation while the reverse primer starts immediately following the mutation (in red). The reverse primer has a single mismatch (in green) that creates a *Clal* restriction cut site in PCR products from wild-type (A, in blue) but not mutant (T, in red) genotypes.

Because the reverse primer is 40bp long, cutting the 155bp PCR product produces a significant band shift when the samples are run on an agarose gel.

(B) Using this scheme, raw cell lysates from progeny (in this case, from the *dhc1b-3* x *fla10* mating) are readily screened for the *dhc1b-3* mutation. The plus symbols indicate the presence of the *dhc1b-3* temperature-sensitive flagellar assembly phenotype, which correlates in each progeny with an undigested PCR product.

Figure S3. Kinetics of flagellar regeneration in *dhc1b-3* at 21C following

increasing pre-incubation times at 34C. Mutant cells were incubated for increasing periods of time (0hr, 6hr, 12hr, 18hr, 24hr) at 34C, pH shocked, and then allowed to recover at 21C. Cells that spent longer at 34C showed delayed onset of regeneration and slower kinetics of flagellar growth. In this experiment, flagellar length was judged and binned visually as “deflagellated”, “stumpy” (~1-3 μ m), “short” (~3-7 μ m), and “full length” (~ >7 μ m). [All the data could be elegantly combined into one graph if this experiment was repeated again with flagellar length measurements, in the style of figure 4].

Table 1. Proteins identified by 2D-DIGE, clustered by accumulation profile (accompanies Fig 8). Color key: "Spot" blue= over 3-fold change; "Protein" red= unidentified or low confidence hit, orange= high confidence hit hypothetical protein, green= protein present in more than one profile; "Predicted MW" and "Predicted PI" blue= good match (<20MW under, <1PI), red= bad match; "Flagellar Proteome?" bold= major fraction, green= major fraction is in the membrane+matrix, red= not found in proteome (Pazour et al., 2005) . "Spot Shift" is the distance from an additional spot with the same ID.

Identification

<u>Spot</u>	<u>Protein</u>	<u>Counts</u>	<u>MW</u>	<u>PI</u>	<u>Spot Shift</u>
D1.1	CAM1, calmodulin	8	18	4.3	
D1.2	FAP103, nucleoside diphosphate kinase-like protein	3	15.5	5.9	-1.9 pH
D1.3	unidentified (U3)	-	33	6.9	-0.4 pH
D1.4	FAP55 or TUB2, beta tubulin 2	22, 18	115	5.4	
D1.5	FAP127	11	70	6.1	
D1.6	FAP189 or FAP58	12, 11	100	7.8	
D1.7	FAP166	9	32	6.1	
D1.8	KLP1, kinesin-like protein 1	22	90	7.8	-0.3 pH
D1.9	PP2C1c, protein phosphatase 2C catalytic subunit isoform 1	15	37	5.8	

Validation

<u>Spot</u>	<u>Predicted MW</u>	<u>Predicted PI</u>	<u>Flagellar Proteome? (counts, fraction)</u>	<u>Notes</u>
D1.1	18	4.3	Yes (9, MM, Ax, KCl, T)	
D1.2	17	6.2	Yes (9, MM), -	glutathiolation target
D1.3	-	-	-	
D1.4	112, 50	5.1, 4.8	Yes (27, Ax, T), Yes (27, KCl, MM, Ax, T)	
D1.5	51	5.3	Yes (11, Ax, T)	
D1.6	102, 101	6.8, 6.6	Yes (6, Ax, KCl), Yes (26, Ax, T, KCl)	
D1.7	24	5.5	Yes (7, Ax, T)	
D1.8	83	6.5	Yes (31, KCl, MM)	
D1.9	29	5.6	Yes? (14, T)	

Identification

Spot	Protein	Counts	MW	PI	Spot Shift
D2A.1	FAP103 or fgenesh2_pg:C_scaffold_81000021	5, 3	16	6.6	-1.2 pH, +1 KDa
D2A.2	estExt_fgenesh2_kg:C_300011 (U5)	5	30	5.9	
D2A.3	FAP162 or SKP1, ubiquitin ligase	8, 2	23	4.7	+1 KDa
D2A.4	CAH9, carbonic anhydrase 9	2	21	5.8	
D2A.5	MSD1, superoxide dismutase [Mn], mitochondrial	8	30	6.2	
D2A.6	FAP102 or TUA2, alpha tubulin 2	5, 12	140	5.5	
D2A.7	RSP10	6	32	5.4	+2 KDa
D2A.8	FAP103 or fgenesh2_pg:C_scaffold_81000021	5	15	6.6	-1.2 pH
D2A.9	IDH3, isocitrate dehydrogenase, NADP-dependent, mitochondrial	18	47	8.2	

Validation

Spot	Predicted MW	Predicted PI	Flagellar Proteome? (counts, fraction)	Notes
D2A.1	17, 16	6.2, 6.2	Yes (9, MM), -	glutathiolation target
D2A.2	22	6.5	-	
D2A.3	19, 18	4.5, 4.6	Yes (8, MM)	
D2A.4	13	6.4	No (there is CAH1)	
D2A.5	24	5.9	No	
D2A.6	82, 50	8.7, 5.0	Yes (13, Ax, KCI), Yes (35, Ax, KCI, T, MM)	contaminant? flagellar redox? redox sensitive
D2A.7	24	5.0	Yes (9, T, Ax)	
D2A.8	17, 16	6.2, 6.2	Yes (9, MM), -	glutathiolation target
D2A.9	54	9.0	No (there is ICL1)	contaminant? flagellar redox?

Identification

Spot	Protein	Counts	MW	pI	Spot Shift
D2B.1	FAP162	12	22	4.7	
D2B.2	unidentified (U2)	-	10	5.2	
D2B.3	FKB12, peptidyl-prolyl cis-trans isomerase, FKBP-type (U2)	4	10	6.5	
D2B.4	e_gwH.2.411.1 {CYB5_3} (U3)	5	31	7.9	
D2B.5	Chire2_kg.scaffold_13000122 (P1)	6	27	6.3	
D2B.6	TUA2 or TUB2 or SHMT2, serine hydroxymethyltransferase 2	10, 14, 10	58	8.0	

Validation

Spot	Predicted MW	Predicted pI	Flagellar Proteome? (counts, fraction)	Notes
D2B.1	19	4.5	Yes (8, MM)	
D2B.2	-	-	-	
D2B.3	12	6.0	No (there is Cyclophilin 1)	
D2B.4	12	9.0	-	
D2B.5	20	6.0	-	
D2B.6	50, 50, 52	5.0, 4.8, 6.3	Yes (35, Ax, KCl, T, MM)	

Identification

Spot	Protein	Counts	MW	pI	Spot Shift
D2C.1	unidentified (U1)	-	17	5.4	
D2C.2	unidentified (U3)	-	33	7.4	
D2C.3	TUB2, beta tubulin 2	11	38	5.7	
D2C.4	FAP147, similar to myc-binding	16	105	8.9	
D2C.5	FAP103 or fgneszh2_pg.C_scaffold_81000021	5	15.5	7.6	
D2C.6	fgneszh2_kg.C_scaffold_45000028, glutathione S-transferase (P2)	4	29	6.7	
D2C.7	RAN1, Ran-like small GTPase	3	32	7.6	
D2C.8	unidentified (U6)	-	48	6.9	
D2C.9	PF17, radial spoke protein 9	10	34	5.6	-0.2 pH

Validation

Spot	Predicted MW	Predicted pI	Flagellar Proteome? (counts, fraction)	Notes
D2C.1	-	-	-	
D2C.2	50	4.8	Yes (27, KCl, MM, Ax, T)	MW too low for tubulin
D2C.3	97	6.7	Yes (9, KCl)	unmodified?
D2C.4	17, 16	6.2, 6.2	Yes (9, MM), - Maybe?	
D2C.5	24	5.5	Yes (3, MM)	GTP bound?
D2C.6	25	6.2	-	
D2C.7	-	-	-	
D2C.8	30	5.0	Yes (17, T, Ax, KCl, MM)	-0.4 pH form has no change
D2C.9				

Identification

Spot	Protein	Counts	MW	PI	Spot Shift
D3.1	EF1A1 and TUA1	17, 12	100	7.0	
D3.2	CAH6, carbonic anhydrase 6	12	30	7.9	-0.5 pH, +1 KDa
D3.3	IFT81 or IFT80 (FAP167), IFT-B	16, 11	84	8.7	
D3.4	RIB43a, protofilament ribbons of flagellar microtubules	17	48	7.5	
D3.5	IFT81, IFT-B	34	86	7.9	
D3.6	estExt_fggenesh2_pg_C_200113 (P3)	15	50	7.5	
D3.7	IFT27 (FAP156, RabL4, small Rab-reated GTPase), IFT-C	5	30	6.0	
D3.8	IFT27 (FAP156, RabL4, small Rab-reated GTPase), IFT-C	8	30	5.6	-0.4 pH
D3.9	PF17, radial spoke protein 9	12	34	5.8	
D3.10	FAP252 (BUG10)	15	42	6.9	
D3.11	FAP144	7	15	8.1	
D3.12	FLA8, Kinesin-2 anterograde motor or KLP1	5, 8	95	8.0	

Validation

Spot	Predicted MW	Predicted PI	Flagellar Proteome? (counts, fraction)	Notes
D3.1	51, 50	8.7, 5.0	Yes (28, MM, KCl, T, Ax), Yes (31, Ax, KCl, MM, T)	covalent dimer?
D3.2	28	7.0	No (there is CAH1)	
D3.3	77, 84	6.3, 6.6	Yes (26, MM), Yes (7, MM)	
D3.4	43	6.0	Yes (33, Ax, T)	
D3.5	77	6.3	Yes (26, MM)	
D3.6	44	6.0	-	new IFT protein or cargo?
D3.7	23	5.3	Yes (8, MM)	GDP bound?
D3.8	23	5.3	Yes (8, MM)	GTP bound?
D3.9	30	5.0	Yes (17, T, Ax, KCl, MM)	
D3.10	39	5.7	Yes (29, T, Ax, KCl, MM)	
D3.11	16	7.0	Yes (9, Ax, T)	
D3.12	86, 83	6.6, 6.5	Yes (19, MM, KCl, T), Yes (31, KCl, MM)	likeley FLA8

Identification

<u>Spot</u>	<u>Protein</u>	<u>Counts</u>	<u>MW</u>	<u>pI</u>	<u>Spot Shift</u>
A1.1	IFT122B (IFTA-1, FAP118 / FBB1), cargo adaptor, IFT-A	25	120	7.2	
A1.2	unidentified (U4)	-	28	6.8	
A1.3	CAH6, carbonic anhydrase 6	9	29	8.0	-0.4 pH
A1.4	ODA1, flagellar outer dynein arm-docking complex protein 2 (ODA-DC2)	35	75	6.9	
A1.5	CAH6, carbonic anhydrase 6	8	29.5	8.4	
A1.6	estExt_fggenesh2_pg_C_10745 or estExt_gwp_1W.C_510064 (P4)	8, 11	120	8.2	
A1.7	FAP59, conserved	10	105	6.8	
A1.8	ODA9, flagellar outer dynein arm intermediate chain 1 (ODA-IC1)	6	200	7.0	
A1.9	RSP16, radial spoke protein 16	16	44	8.4	
A1.10	FAP191, similar to quinone reductase or AGG3	1, 5	26	8.4	

Validation

<u>Spot</u>	<u>Predicted MW</u>	<u>Predicted pI</u>	<u>Flagellar Proteome? (counts, fraction)</u>	<u>Notes</u>
A1.1	136, 132	6.0, 6.3	Yes (11, MM, KCl)	
A1.2	-	-	No (there is CAH1)	more modified form is D3.2
A1.3	28	7.0	Yes (18, T)	
A1.4	62	5.8	No (there is CAH1)	
A1.5	28	7.0	-	
A1.6	85, 137	9.0, 6.6	Yes (26, Ax, T, KCl)	
A1.7	101	6.0	Yes (14, T)	
A1.8	76	5.9	Yes (26, T, Ax, KCl, MM)	
A1.9	39	6.7	Yes (6, MM), Yes (9, MM)	
A1.10	28, 21	7.1, 6.3		same MW as AGG3, +1.1 pH

Identification

<u>Spot</u>	<u>Protein</u>	<u>Counts</u>	<u>MW</u>	<u>PI</u>	<u>Spot Shift</u>
A2A/B.1	KLP1, kinesin-like protein 1	35	90	8.1	
A2A/B.2	FAK1, ODA5-associated flagellar adenylate kinase	8	145	7.5	
A2A/B.3	FAP7	21	68	8.4	
A2A/B.4	AGG3 (FAP142), flavodoxin similar to quinone reductase	6	26	7.3	
A2A/B.5	FAP172 or Dhc1b	24, 33	105	6.3	
A2A/B.6	FAP115	8	32	6.7	
A2A/B.7	Rib72, pf rib of flag MT, nucleoside-diphosphokinase regulatory subunit p72	22	77	8.6	

Validation

<u>Spot</u>	<u>Predicted MW</u>	<u>Predicted PI</u>	<u>Flagellar Proteome? (counts, fraction)</u>	<u>Notes</u>
A2A/B.1	83	6.5	Yes (31, KCl, MM)	unmodified?
A2A/B.2	71	6.6	Yes (25, T, KCl, MM, Ax)	
A2A/B.3	55	6.7	Yes (20, Ax, T, KCl, MM)	
A2A/B.4	21	6.3	Yes (9, MM)	
A2A/B.5	64, 481	5.5, 6.1	Yes (7, Ax, T), Yes (88, MM, KCl, Ax)	
A2A/B.6	27	5.8	Yes (11, Ax, T, KCl, MM)	
A2A/B.7	72	7.2	Yes (44, Ax, T, KCl, MM))	

Identification

Spot	Protein	Counts	MW	pI	Spot Shift
A2C.1	ODA1, flagellar outer dynein arm-docking complex protein 2	23	75	6.7	-0.1 pH
A2C.2	FAP7	21	68	8.1	-0.3 pH
A2C.3	FAP219	11	38	6.9	
A2C.4	unidentified (U7)	-	80	7.1	
A2C.5	PF14, radial spoke protein 3	20	80	5.3	
A2C.6	ODA1, flagellar outer dynein arm-docking complex protein 2	17	75	6.6	-0.3 pH
A2C.7	fgenesH2_pg_C_scaffold_721000001 (P5)	15	90	6.2	
A2C.8	ODA9 (ODA-IC1), or ChIre2_kg:scaffold_620000038	28	85	6.8	
A2C.9	PF2, component of dynein regulatory complex (DRC)	9	62	8.2	
A2C.10	FAP252 (BUG10)	20	44	6.1	

Validation

Spot	Predicted MW	Predicted pI	Flagellar Proteome? (counts, fraction)	Notes
A2C.1	62	5.8	Yes (18, T)	
A2C.2	55	6.7	Yes (20, Ax, T, KCl, MM)	
A2C.3	21	9.7	Yes (5, Ax, T)	
A2C.4	-	-	-	
A2C.5	57	4.9	Yes (27, Ax, T, KCl)	
A2C.6	62	5.8	Yes (18, T)	
A2C.7	72	11.7	-	
A2C.8	76, 30	5.9, 10.1	Yes (14, T), -	
A2C.9	55	8.4	Yes (16, Ax, T, KCl)	
A2C.10	39	5.7	Yes (29, Ax, T, KCl, MM)	

Identification

<u>Spot</u>	<u>Protein</u>	<u>Counts</u>	<u>MW</u>	<u>PI</u>	<u>Spot Shift</u>
A3.1	FAP12, lipase domain	7	38	8.7	+1 KDa
A3.2	FAP215, conserved	8	73	6.0	
A3.3	unidentified (U8)	-	200	5.1	
A3.4	ODA6, flagellar outer dynein arm intermediate chain 2 (ODA-IC2)	12	80	5.9	-0.3 pH
A3.5	FAP31, conserved TPR repeat, <i>or</i> FAP197	18, 6	95	5.4	
A3.6	FAP43, conserved	16	200	7.3	
A3.7	PGM1b, phosphoglycerate mutase, <i>or</i> PGM1a <i>or</i> ODA1	13, 13, 11	75	6.3	
A3.8	FAP12, lipase domain	5	37	8.4	
A3.9	FAP203, weakly similar to HSP70	8	48	8.4	
A3.10	BUG13, basal body protein of unknown function	10	35	8.9	
A3.11	EB1	12	35	6.6	
A3.12	unidentified (U1)	-	18	4.7	
A3.13	e_gww.1.241.1 (P6)	13	49	5.8	
A3.14	FAP57, conserved	10	150	5.8	
A3.15	IDA4, flagellar inner arm dynein light chain p28	18	33	8.0	
A3.16	FAP252 (BUG10)	19	44	5.8	
A3.17	FAP18, high E/VP content protein	15	90	4.7	

Validation

<u>Spot</u>	<u>Predicted MW</u>	<u>Predicted PI</u>	<u>Flagellar Proteome? (counts, fraction)</u>	<u>Notes</u>
A3.1	54	5.7	Yes (25, T, MM, KCl, Ax)	cleaved FAP12?
A3.2	52	5.0	Yes (6, MM)	
A3.3	-	-	Yes (9, T)	
A3.4	63	5.4	Yes (9, MM), Yes (6, KCl)	
A3.5	74, 33	6.5, 6.0	Yes (54, KCl, Ax, T)	
A3.6	178	8.5	Maybe?	
A3.7	61, 67, 62	5.6, 5.6, 5.8	Yes (25, T, MM, KCl, Ax)	cleaved FAP12?
A3.8	54	5.7	Yes (6, Ax, KCl, MM)	dimer?
A3.9	19	7.2		

A3.10	28	8.6	No?
A3.11	31	5.7	Yes (2, MM)
A3.12	-	-	-
A3.13	31	5.3	-
A3.14	120	6.2	Yes (26, Ax, KCl, T)
A3.15	29	6.7	Yes (21, KCl, T, Ax, MM)
A3.16	39	5.7	Yes (29, Ax, T, KCl, MM)
A3.17	55	4.4	Yes (17, KCl, MM, T, Ax)

Identification

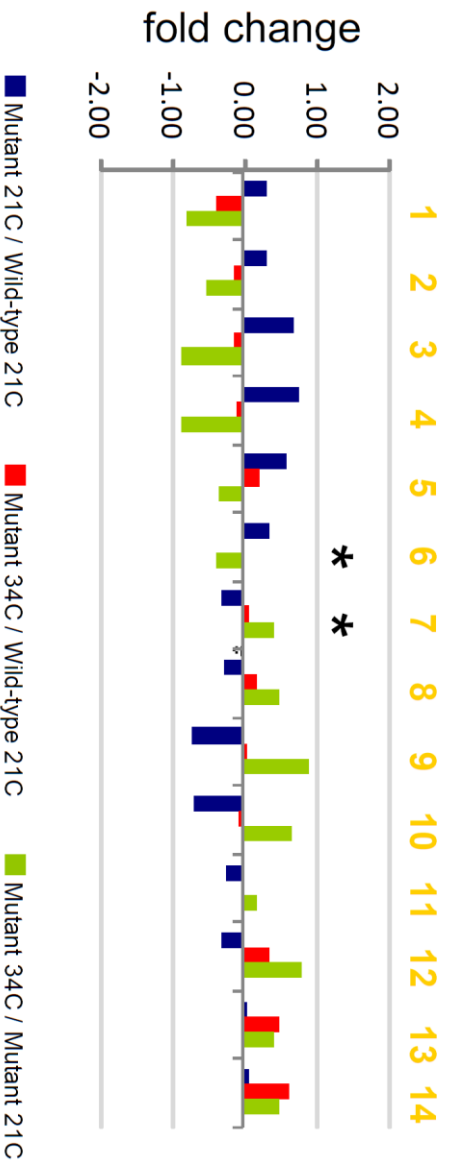
Spot	Protein	Counts	MW	PI	Spot shift
NC.1	RSP10	6	30	5.4	
NC.2	RIB43a , protofilament ribbons of flagellar microtubules	24	48	6.9	-0.6 pH
NC.3	FAP164	12	47	6.0	
NC.4	ICL1, isocitrate lyase, or RIB43a	14, 12	48	6.7	
NC.5	ODA13, flagellar outer dynein arm light chain 6 (ODA-LC6)	6	14	6.9	
NC.6	IDA5, actin (normalization control)	21	48	5.7	-0.1 pH
NC.7	IDA5, actin (normalization control)	16	48	5.8	
NC.8	IFT81 , IFT-B	21	86	7.3	-0.6 pH
NC.9	FAP161	12	54	6.6	
NC.10	RIB43a , protofilament ribbons of flagellar microtubules	23	48	7.2	-0.3 pH
NC.11	IFT88, IFT-B or METE Vit B12 (cobalamin) Independent methionine synthase	20, 16	94	7.0	
NC.12	IFT88, IFT-B	15	94	6.8	-0.2 pH
NC.13	FAP52	19	80	7.0	
NC.14	FAP52	30	80	6.7	-0.3 pH

Validation

Spot	Predicted MW	Predicted PI	Flagellar Proteome? (counts, fraction)	Notes
NC.1	24	5.0	Yes (9, T, Ax)	
NC.2	43	6.0	Yes (33, Ax, T)	
NC.3	48	5.9	Yes (8, MM)	
NC.4	46, 43	5.9, 6.0	Yes (3, MM), Yes (33, Ax, T) Yes (6, T)	
NC.5	14	6.3	Yes (22, KCl, Ax, T, MM)	
NC.6	42	5.3	Yes (22, KCl, Ax, T, MM)	
NC.7	42	5.3	Yes (22, KCl, Ax, T, MM)	
NC.8	77	6.3	Yes (26, MM)	
NC.9	43	5.6	Yes (8, Ax, KCl)	
NC.10	43	6.0	Yes (33, Ax, T)	
NC.11	86, 87	5.9, 6.0	Yes (14, MM)	
NC.12	86	5.9	Yes (14, MM)	

NC.13	67	5.8	Yes (30, Ax, T, KCl)
NC.14	67	5.8	Yes (30, Ax, T, KCl)

NC



Accumulation and depletion of spots binned into the “no change” profile. The two IDA5 actin spots (marked with asterisks) have the smallest changes between the three samples and were used as controls to normalize the abundance of all of the other spots on the gel. For quantification of the other accumulation/depletion profiles, see Figure 8.

Table S1. Primers used for quantitative PCR.

	Forward Primer	Reverse Primer
Housekeeping		
RbcL	TTCAATGCCAGGTGTTATGCC	ACCGAACTGAAGACATGCGTC
RbcS2A	GACCTTCTCCTACCTGCC	TCCGACTCAGCGAACTCC
Alt. Housekeeping		
CBLP	GGCGAGTGCAAGTACACCA	GGTTCCAGACCTTGACCATC
EEF1	TGGAGAAGCTGAAGGAGGAG	GCGTCGATGATGGTGTAGTG
CAH3	CACTACCCTGGCTCGCTTAC	TGGTGGCGTATGTCTTGTTG
Anterograde Motor		
FLA10	GACCTGTGCGAGTTTGTGTG	CGATGGTGATGGTGAAGATG
KAP1	GTTAGCACGCAGTCAGATGG	CGATGGGTGAATGAGCTTG
Retrograde Motor		
Dhc1b	GCGTTCATCACCTACCTGC	CCCTCAGCCTTCCACTTG
D1blic	CAAGAACCAGGACCCAGAG	GACAGGTAGCACAGGAAGG
IFT Complex B		
IFT81	CAACAACGCCATCAACCAGC	GCGGTCTTCTTCTCCAGG
IFT172	CAAGCGCAACAAGATGTACG	CCTCCACAAAGTGCTTCTCC
IFT88	CCTGGTCATGTGCAACTACG	GTCGTCGTCATCGTCATCC
IFT27	GTAGCAGTAGTCGGCGAAGC	CACTCGTCATCGCATAGTCC
IFT20	GCGGAAACGTAAACAAAAGG	GCCCTTCACCTTGATCAGC
IFT Complex A		
IFT140	CTACGACGACCGCTACAACC	ACTTGGCGAAATCCAGAACC
IFT139	GCCCTGGTCCATTACTATGC	CACGCCAGAATGTGAGTACG

IFT122B	AACCAGCAAGGATGTGAAGG	AGTGGTGAGCTTCTGGAACG
BBS4	GCCTTCGAGTACCTCACCAC	AGAGCCACGTCCATGTCAG
Axoneme Components		
TUA1	TGCATGATCTCCAACAGCAC	ACCCTCCTCCATACCCTCAC
IC69	CGACCCCATCTACGACTTTG	TGTTCTCCACGCACTCATTC

Table S2. Primers used for sequencing *Dhc1b* cDNA, including UTRs.

	Forward Primer	Reverse Primer
-93 – 430bp (5' UTR)	AAGCCCTGTGAACTTTGACG	CCAGCAGCTCAGACAAACG
364 – 990bp	CCGCTTATCAAGTCACAGACC	CCAGTCCTCCACCAGAGC
973 – 1481bp	GCTCTGGTGGAGGACTGG	AGGGTCTCCTTCTCACTCTGC
1399 – 2020bp	GTGTTTGCGGAGATCAAGC	GTTTCAGCACCATACCGTACC
1866 – 2504bp	GAACAGCCACGTGAAGACG	CGAAACACCATCTTGACTTCC
2405 – 3062bp	GGGACTTCCAGCTGTACAAGG	ATGTCCTCCACGGTGTTAGC
2875 – 3504bp	CGCATCGAGTGCTACAAGG	TGGCACGTCAATCTTAAACG
3408 – 3982bp	GGCCAAGATCCAGGAGTACG	TAAGCTCAGTCAGCGCCTTG
3863 – 4520bp	TCACGCTCACGCATTTCC	GCTTGGCCCAGAATCTCC
4363 – 5009bp	GCTGATATCCCTGGCATCC	TCCTTGGCCAGGTACTION
4868 – 5506bp	AGCTGGTGACCGAGATGC	CCACCTCCACAGTCTTGTCC
5427 – 6031bp	CCAGCAGATTCAGACCATCC	GCGTCAGCTCCATCTTGC
5893 – 6569bp	CTCACCTTTGACGACAACCTCC	GTGGCTTGCACCTTGAGC

6383 – 7061bp	ACCGCCTGCTGACTATGC	ACACCCATGATGCGCTTG
6924 – 7593bp	GGTTACACCCGAGGTGACG	GTAGTGCGGGTAGTCGTTGG
7411 – 8095bp	ATCGTCACCATGGGCTACC	CCATGTTGTGCATGTACGC
7897 – 8450bp	GAGCTAGTGGCGGAAAAGC	CGGAACATCTCGTTTGAGG
8369 – 9055bp	ACTCGTACGCCTTCTTCAGC	TCTCAGCGATGTTATCCTTCTTG
8934 – 9511bp	CGAGGAGGTGGAGATGAAGG	CCTCGCTGGTCTTCTTGC
9398 – 10001bp	AGAGCAGTCTGGAGGAGAGC	TCCAGTGTGGTGGTGAAGC
9859 – 10539bp	ATCCTCAACTCCACCTCTCG	GGGTCGGTACACCTCACG
10436 – 11057bp	AGCTGAACGAGACCAAGACG	AGCTGCTGGAAGGGGTTTC
10822 – 11377bp	CAGTGGGCCTTCTTCCTG	TCTTGAGCACCAGCCAGTC
10822 – 11432bp	CAGTGGGCCTTCTTCCTG	AGCATCAGCAGCTCCTTCTC
10829 – 11452bp	CCTTCTTCCTGGGCAAGC	GGAAGTTGTCGTGCTTCTGC
11363 – 11987bp	GGCTGGTGCTCAAGAACG	GCCGAGATGATGGACACG
11845 – 12699bp (spans mutation)	CAAGTGCTGCTGACCTTCC	CTTGAGCTTGGCGGTTTC
12399 – 12968bp	GCTGGCGGACGTTATTCC	ACCCAGCCATCCATCTCC
12835 – 13349bp (3' UTR)	TGGCTGCACAAGGACTCG	TGTCAGAAATCAAACATCAGTCG

References

- Iomini C., Li L., Mo W., Dutcher S. K., and Piperno G. 2006. Two flagellar genes, AGG2 and AGG3, mediate orientation to light in *Chlamydomonas*. *Curr. Biol.* 16:1147-1153.
- Kamiya, R. and Hasegawa, E. 1987. Intrinsic difference in beat frequency between the two flagella of *Chlamydomonas reinhardtii*. *Exp. Cell Res.* 173:299-304.
- Kozminski, K. G., P. L. Beech, and J. L. Rosenbaum. 1995. The *Chlamydomonas* kinesin-like protein FLA10 is involved in motility associated with the flagellar membrane. *J. Cell Biol.* 131:1517-1527.
- Lechtreck, K. F., Johnson, E. C., Sakai, T., Ikebe, M., and Witman, G. B. 2009. The *Chlamydomonas* BBSome is transported by a subset of IFT particles and *bbs* mutants abnormally accumulate flagellar signaling proteins. *J. Cell Biol.* 187:1117-1132.
- Pazour G. J., Agrin N., Leszyk J., Witman G. B. 2005. Proteomic analysis of a eukaryotic cilium. *J. Cell Biol.* 170:103-113.
- Pazour, G. J., B. L. Dickert, and G. B. Witman. 1999. The DHC1b (DHC2) isoform of cytoplasmic dynein is required for flagellar assembly. *J. Cell Biol.* 144:473-481.
- Porter M. E., Bower R., Knott J. A., Byrd P., and Dentler W. 1999. Cytoplasmic dynein heavy chain 1b is required for flagellar assembly in *Chlamydomonas*. *Mol. Biol. Cell.* 10:693-712.
- Qin H., Diener D. R., Geimer S., Cole D. G., and Rosenbaum J. L. 2004. Intraflagellar transport (IFT) cargo: IFT transports flagellar precursors to the tip and turnover products to the cell body. *J. Cell Biol.* 164:255-266.
- Zhang J., Guo H., Mi Z., Gao C., Bhattacharya S., Li J., and Kuo P. C. 2009. EF1A1-actin interactions alter mRNA stability to determine differential osteopontin expression in HepG2 and Hep3B cells. *Exp. Cell Res.* 315:304-312.

Figure 4.1

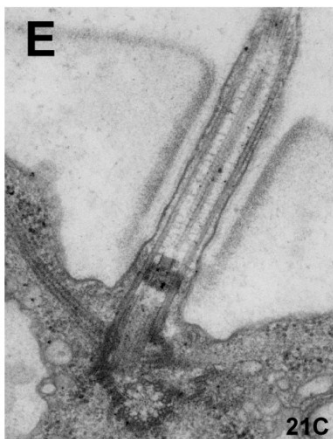
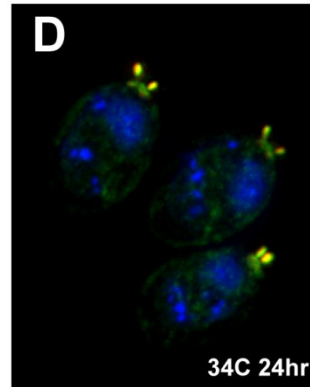
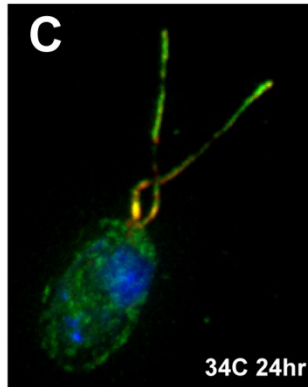
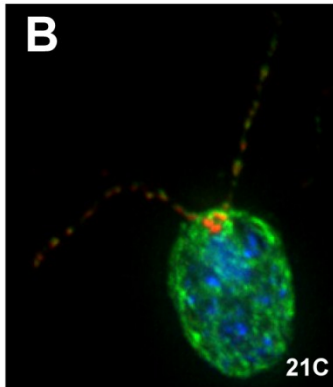
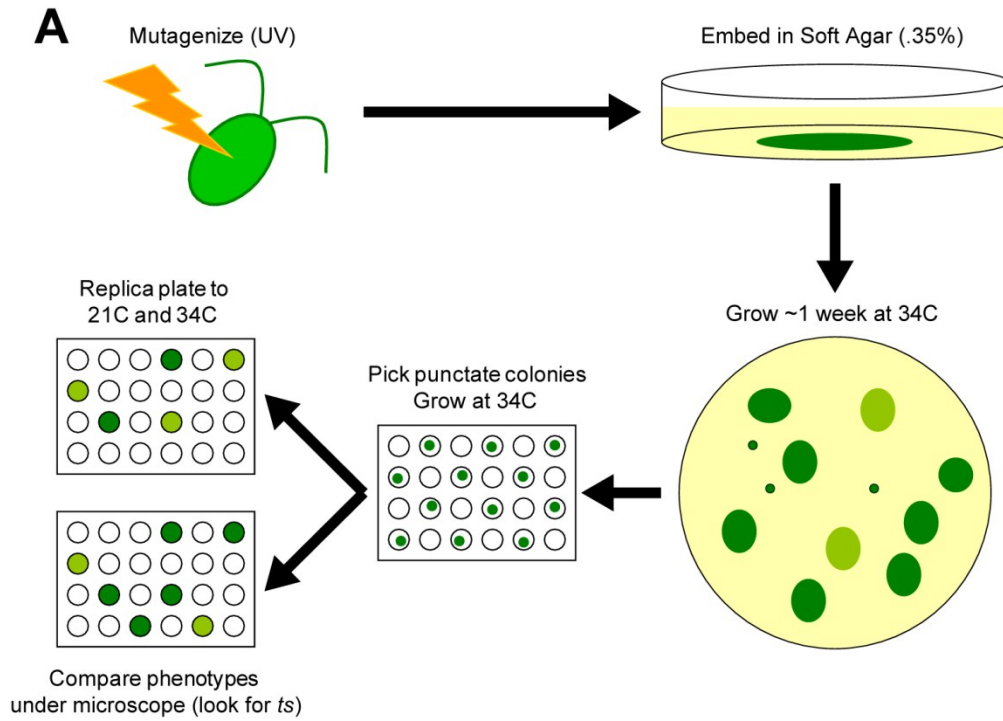


Figure 4.2

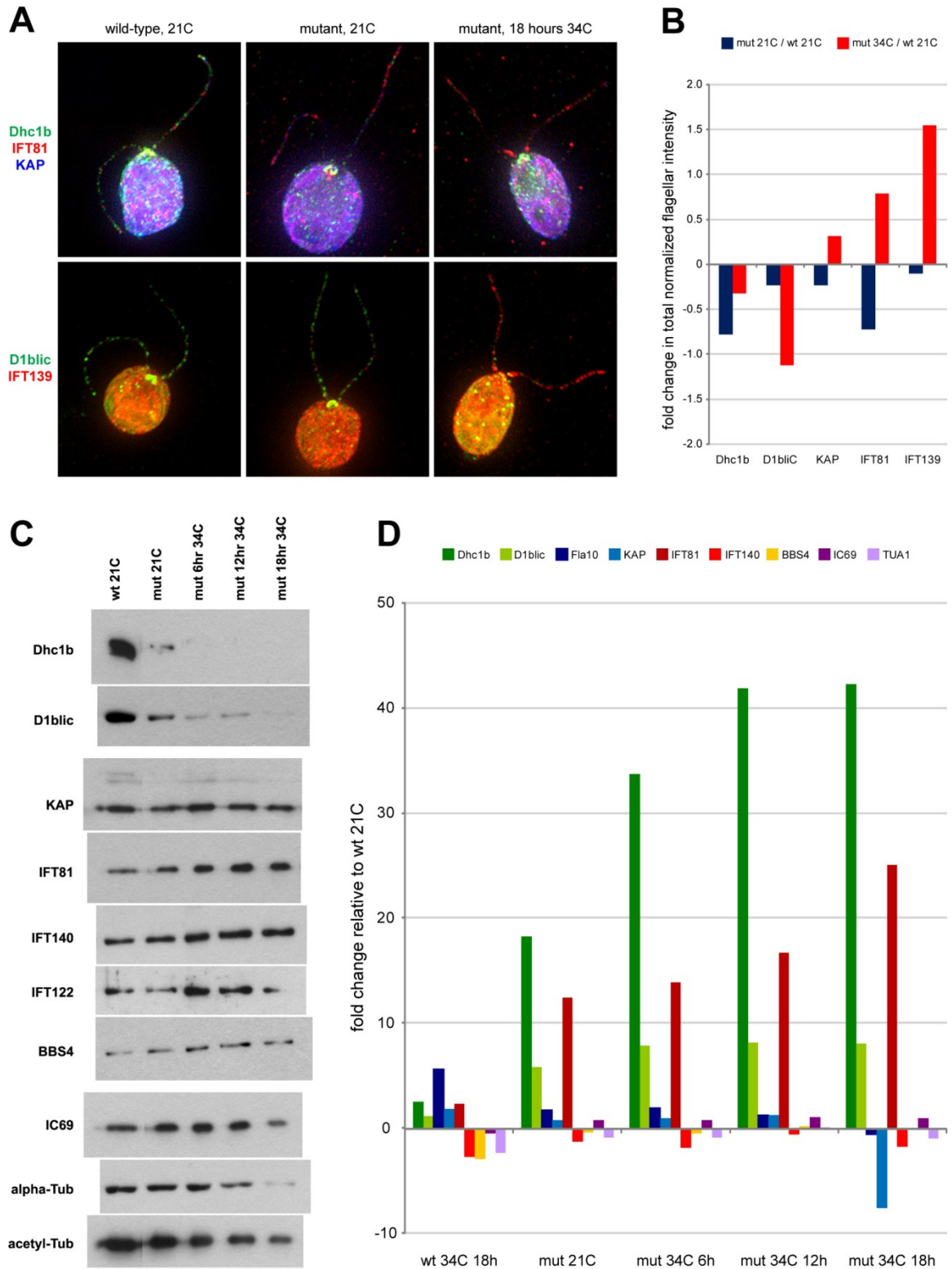
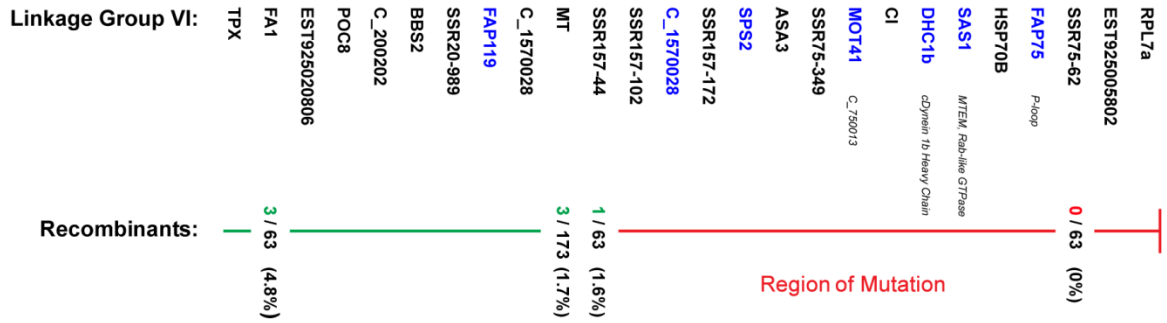


Figure 4.3

A



B

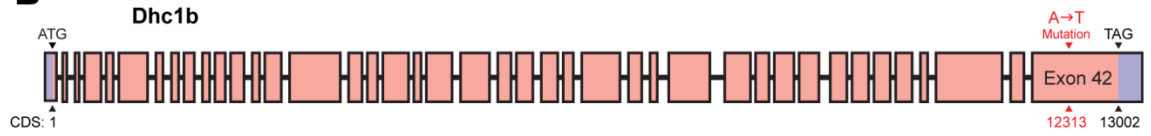


Figure 4.4

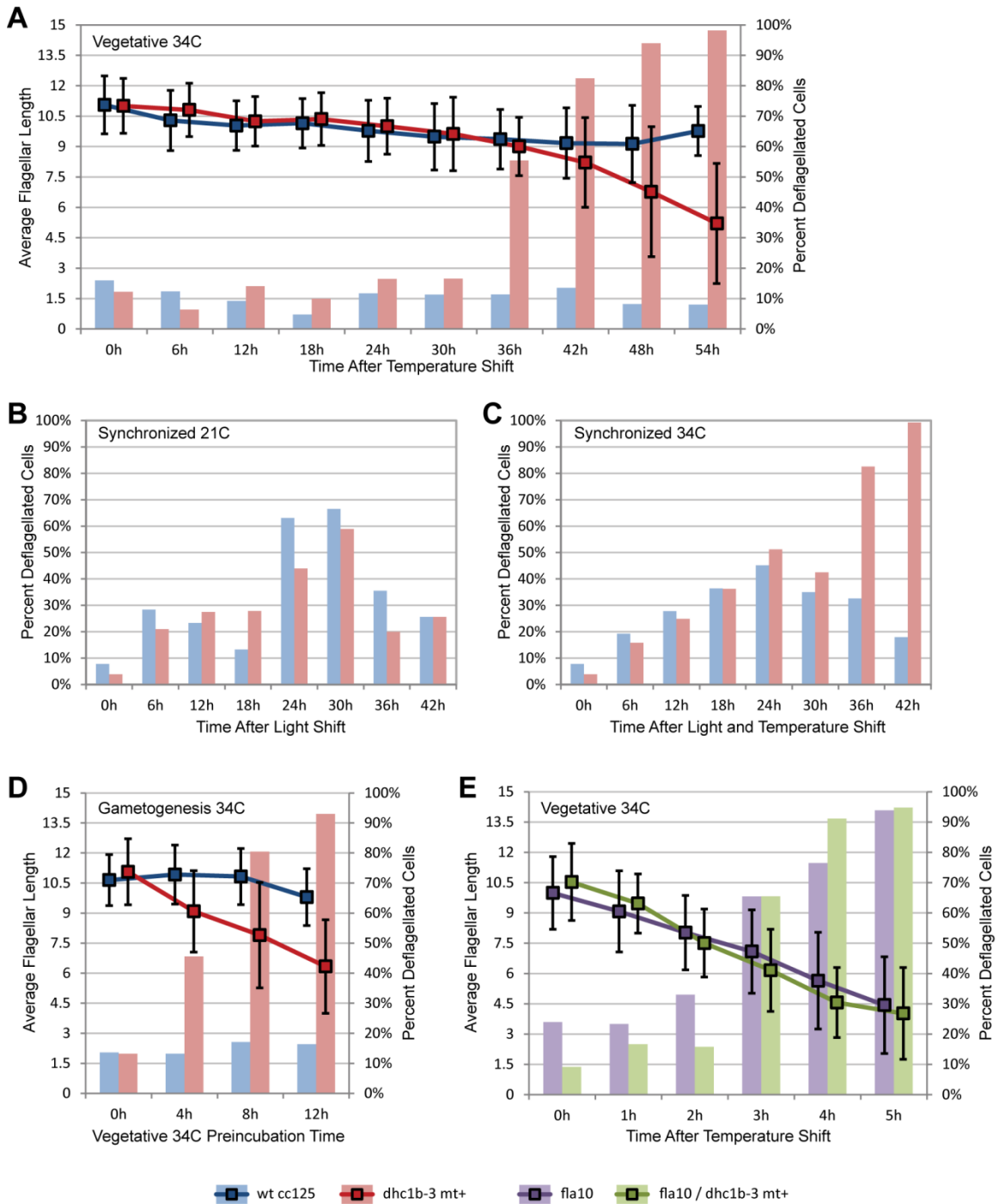
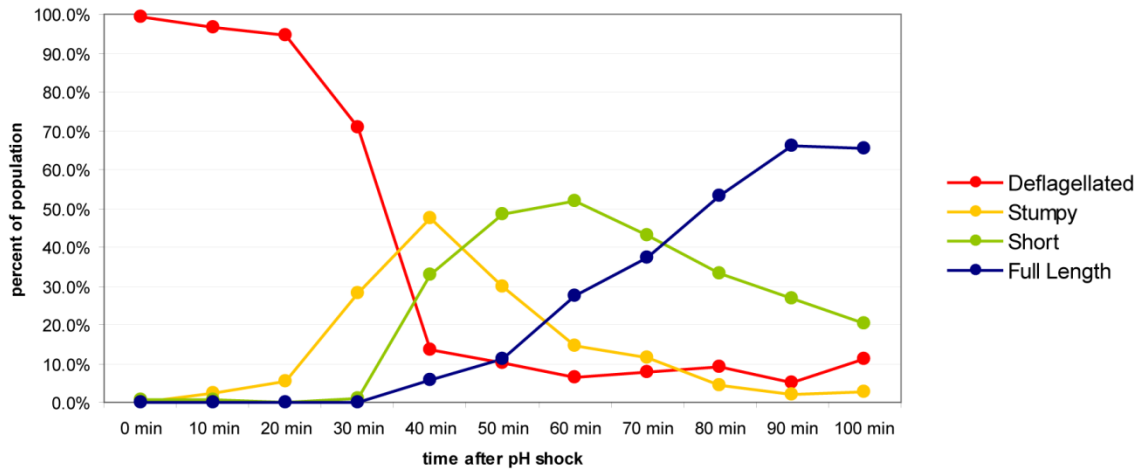
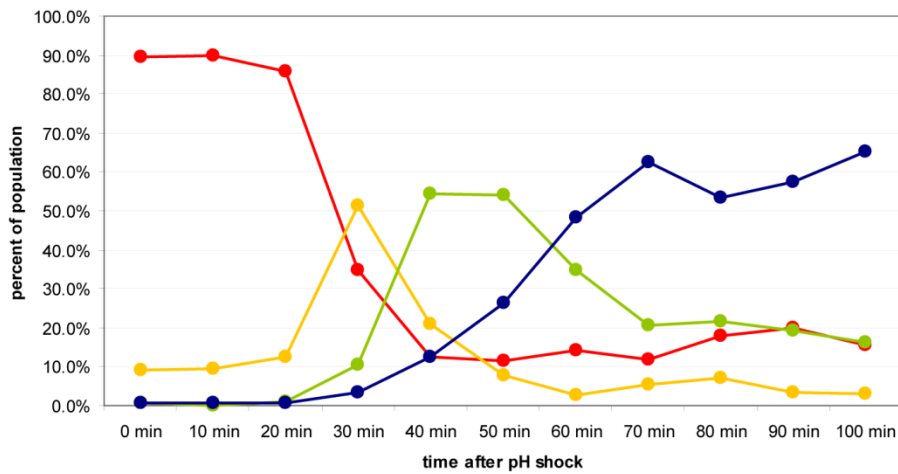


Figure 4.5

Wild-type 21C, recovery at 21C



Mutant 21C, recovery at 21C



Mutant 21C, recovery at 34C for two hours, then shift to recovery at 21C

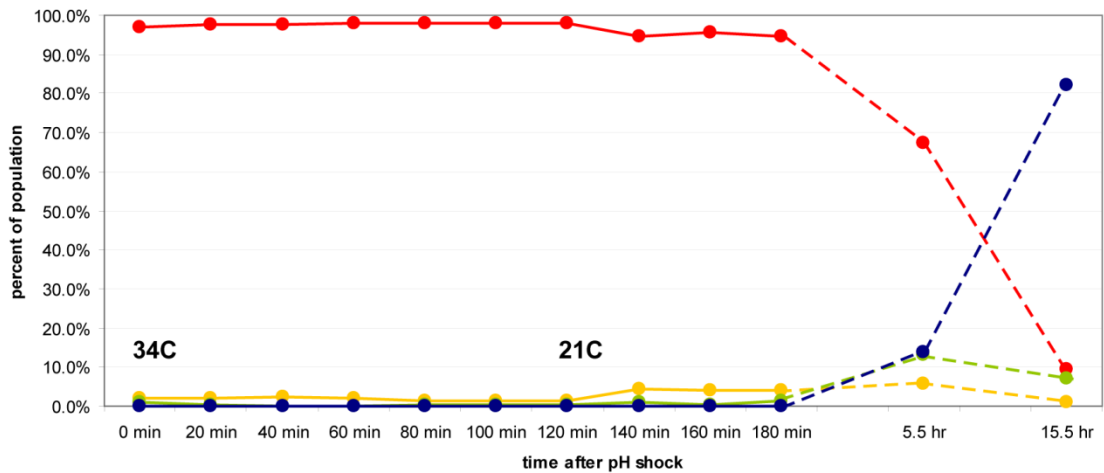


Figure 4.6

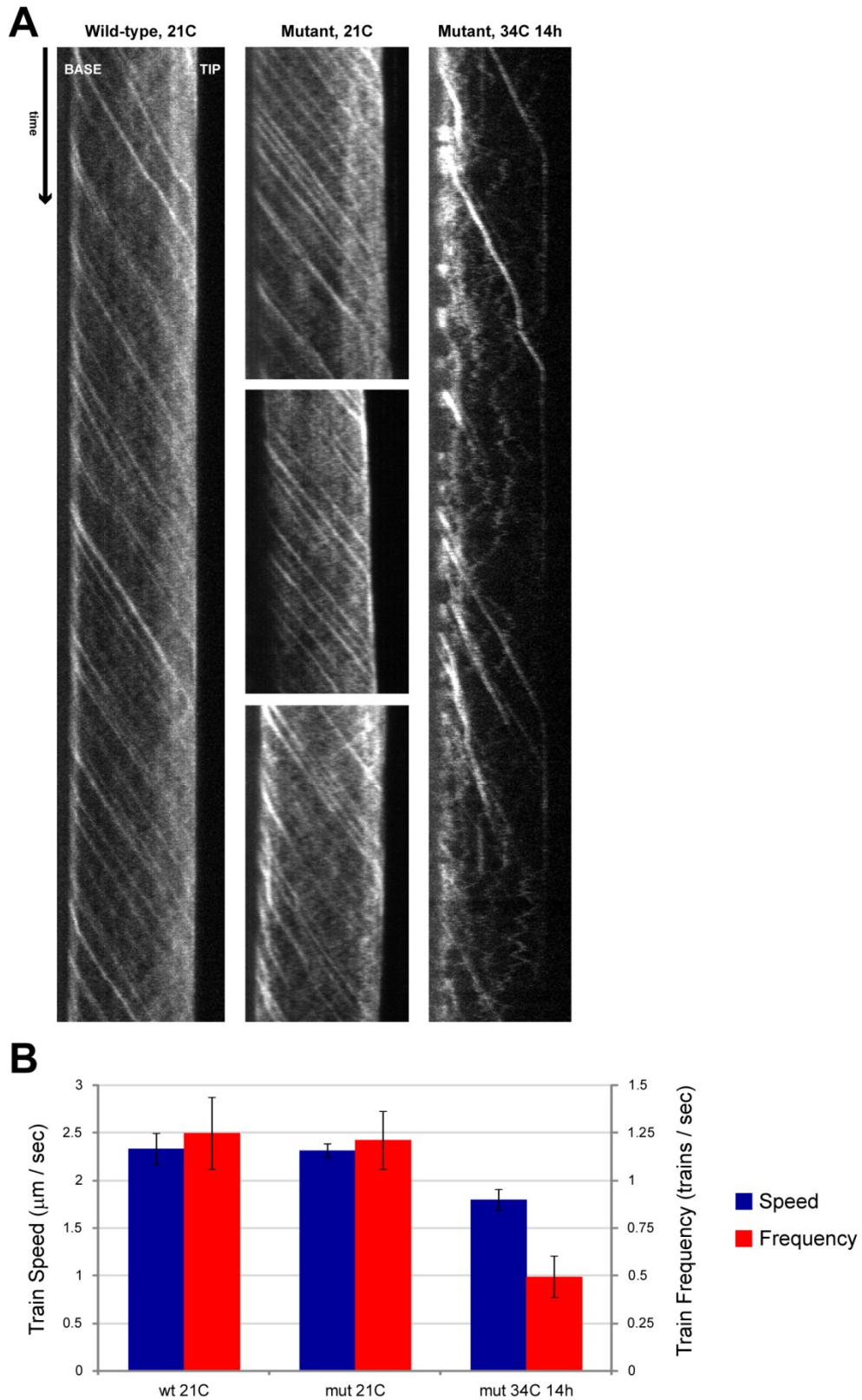


Figure 4.7

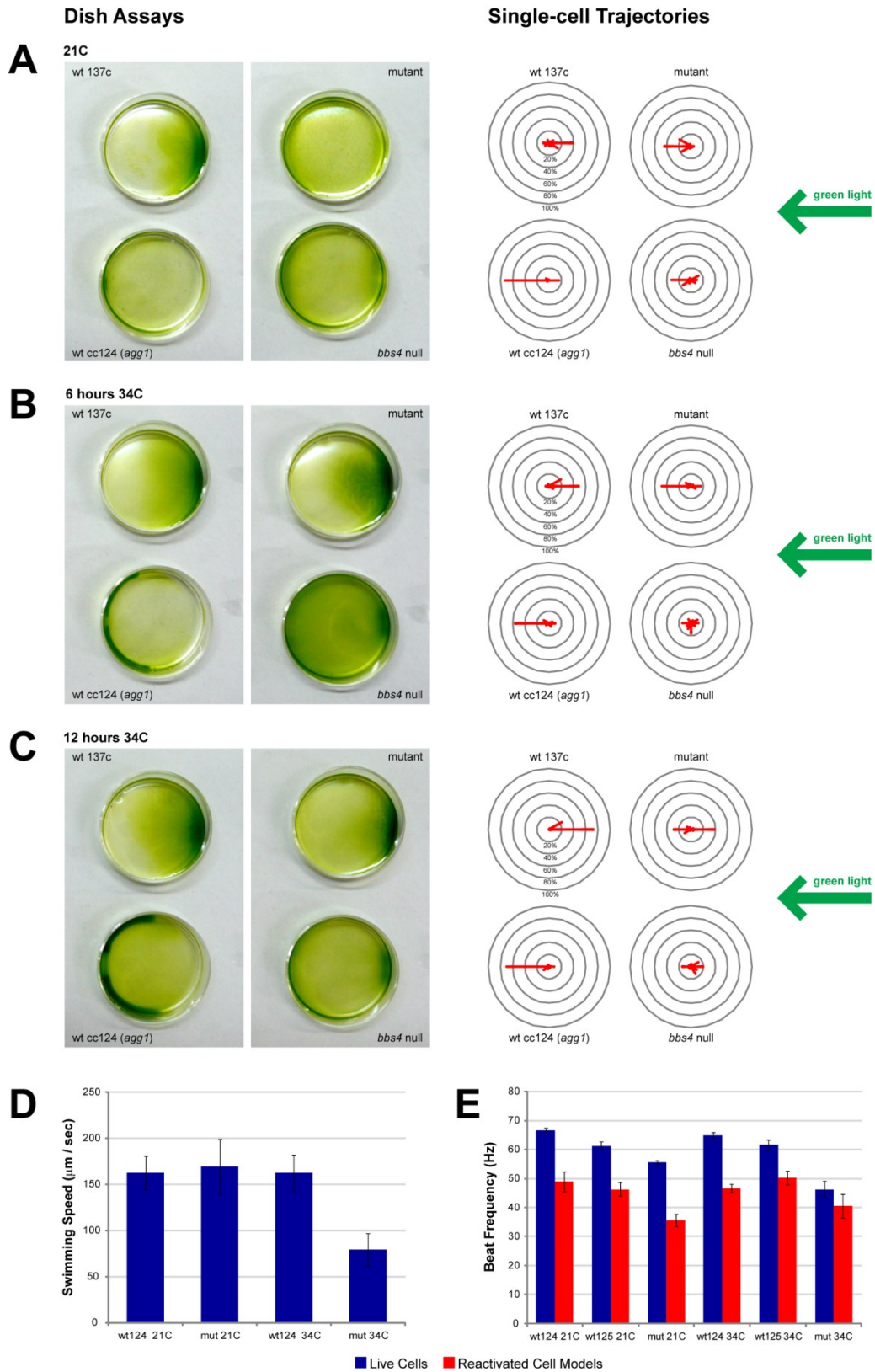


Figure 4.8

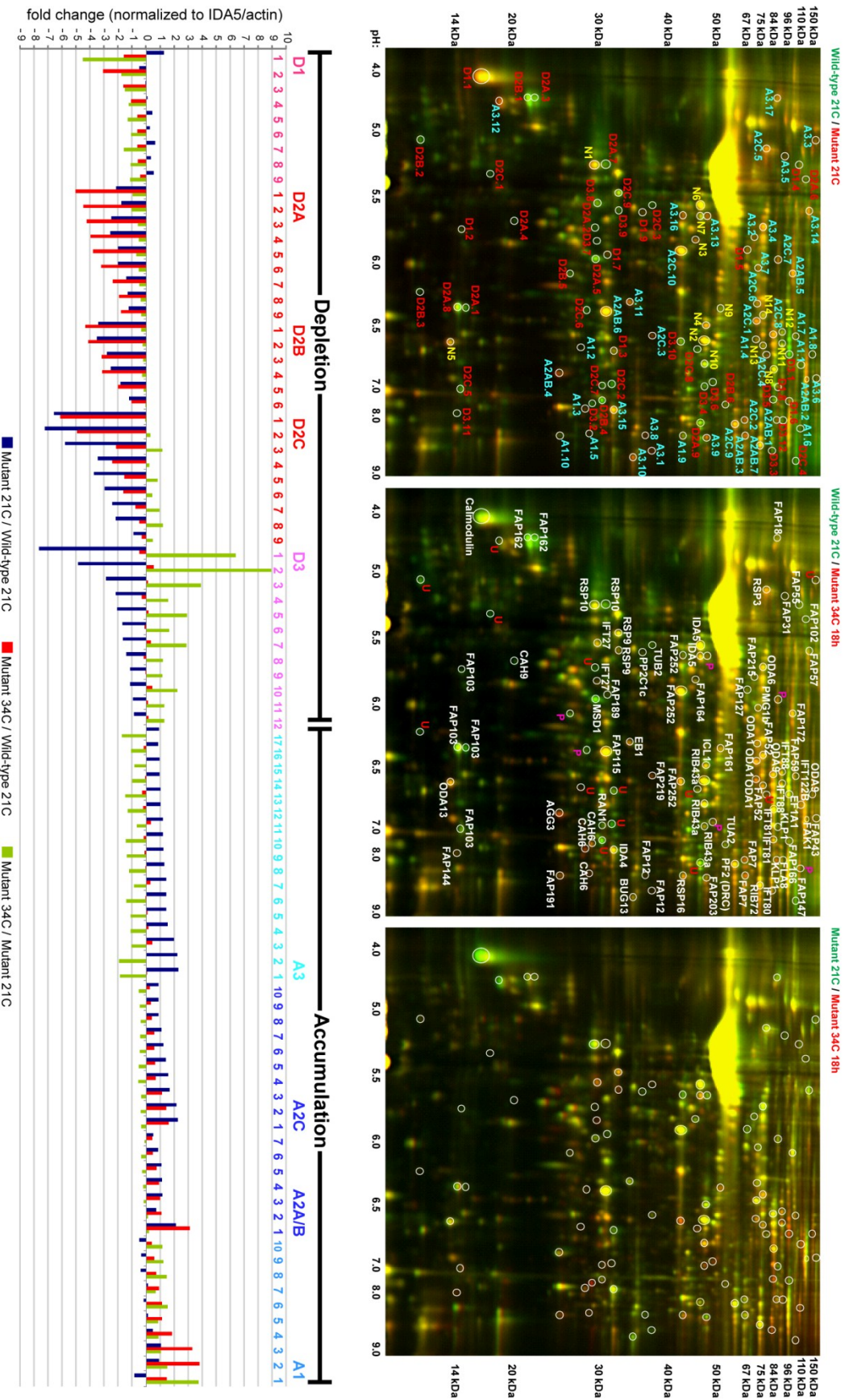


Figure 4.S1

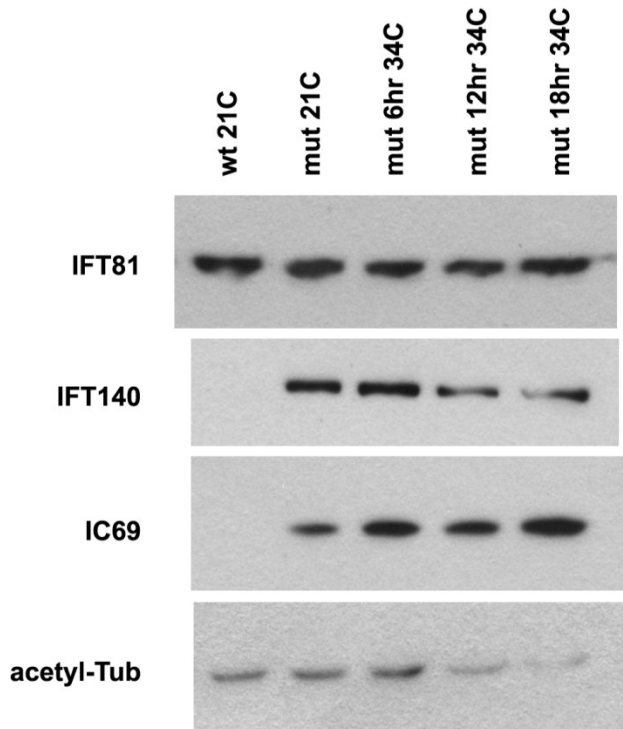


Figure 4.S2

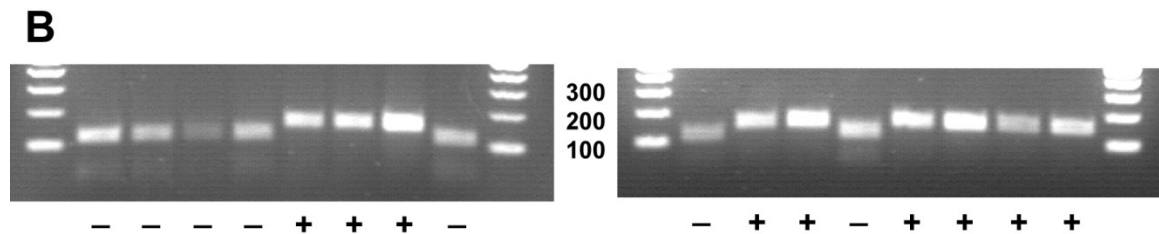
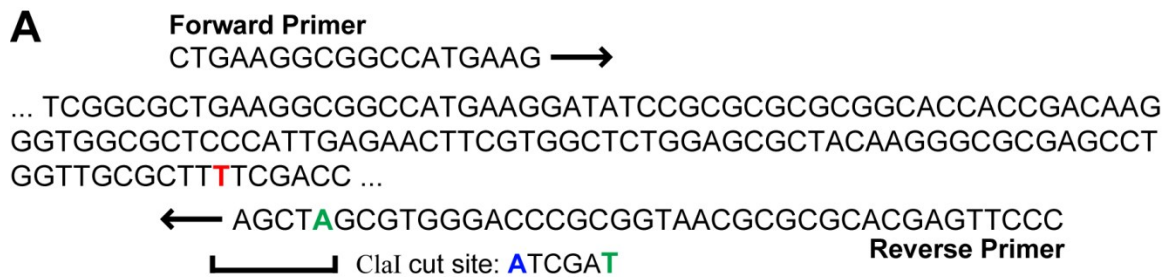
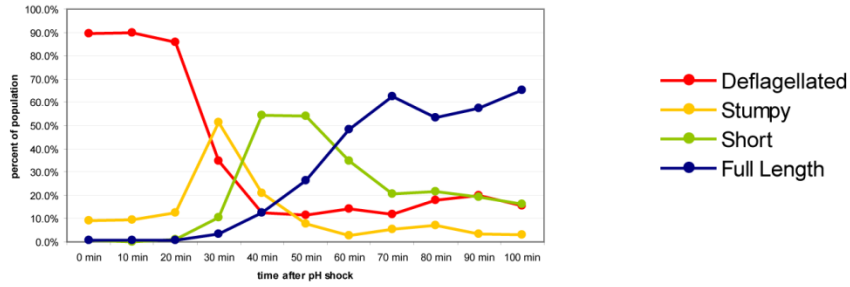
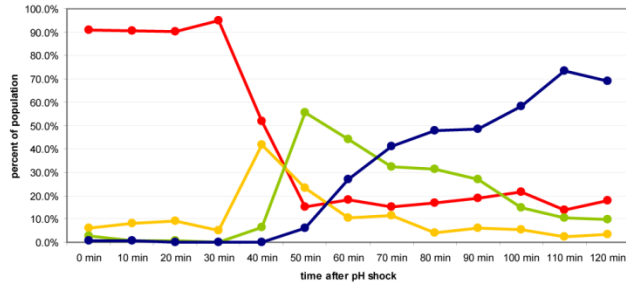


Figure 4.S3

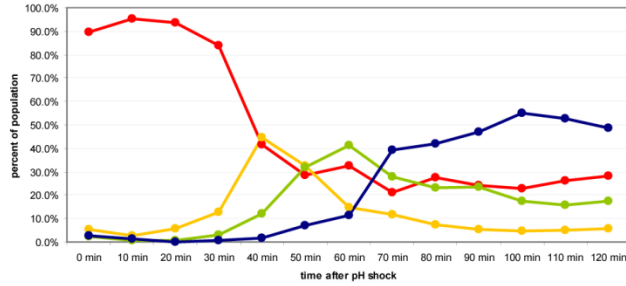
Mutant 21C, recovery at 21C



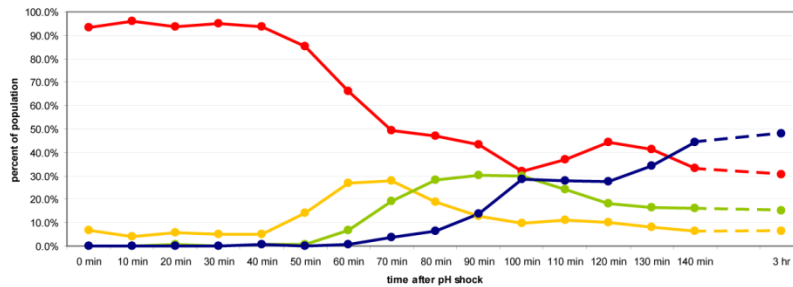
Mutant 6 hours 34C, recovery at 21C



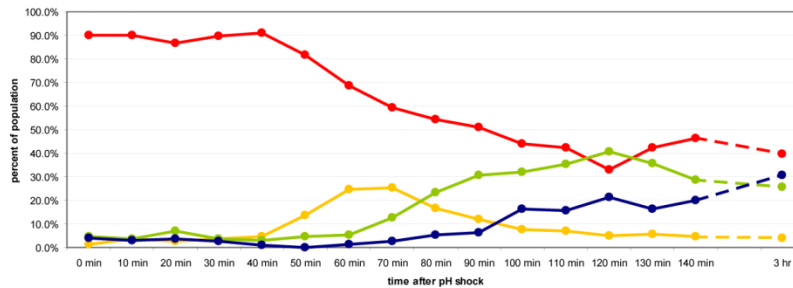
Mutant 12 hours 34C, recovery at 21C



Mutant 18 hours 34C, recovery at 21C



Mutant 24 hours 34C, recovery at 21C



Appendix

Contributions to “The Intraflagellar Transport Particle Sub-complex 25/27 Regulates IFT Particle Stability and Composition”

Zhen-Chuan Fan¹, Zhaohui Wang¹, Benjamin D. Engel², Stefan Geimer³,
Wallace F. Marshall², and Hongmin Qin¹

1. Dept. of Biology, Texas A&M University
2. Dept. of Biochemistry and Biophysics, UCSF
3. Dept. of Cell Biology/Electron Microscopy, University of Bayreuth, Germany

In review for *The Journal of Cell Biology*, May, 2011.

Results

The nucleotide state of IFT27 may regulate IFT particle composition

Purification of IFT27[S79L]::HA::6×His and IFT27[S30N]::HA::6×His from flagellar extracts revealed that the IFT-B main complex was pulled down by each of the IFT27 mutants. However, IFT-A was only enriched within IFT27[S79L]::HA::6×His-associated protein complexes (Figs. 8A and 8B), similar to purification from whole cell extracts (Figs. 7C and 7D). This result indicates that two classes of IFT particles, IFT-A-B and IFT-B, can both enter flagella. We next examined the movement of IFT trains in IFT25::HA::GFP, IFT27::GFP, IFT27[S30N]::GFP, and IFT27[S79L]::GFP strains with total internal reflection fluorescence (TIRF) microscopy followed by kymograph analysis (Engel et al., 2009a; Engel et al., 2009b; Lechtreck et al., 2009). Both mutant IFT27::GFP-fusion proteins underwent robust bi-directional IFT with similar anterograde and retrograde speeds as wild-type GFP-tagged IFT27 and IFT25 (Figs. 8C-8H; Movies S1-S4). Thus, both IFT-A-B and IFT-B are likely capable of bi-directional IFT.

Close examination revealed that the movement of IFT27[S30N]::GFP trains appeared more jerky and stalling (Fig. 8E), while IFT27[S79L]::GFP trains looked more processive (Fig. 8F). While the speed distributions of wild-type IFT27::GFP and IFT25::HA::GFP trains had peak anterograde speeds of 2.3-2.4 $\mu\text{m}/\text{sec}$, IFT27[S30N]::GFP trains showed a small 0.1 $\mu\text{m}/\text{sec}$ peak speed decrease, and IFT27[S79L]::GFP trains experienced a 0.2 $\mu\text{m}/\text{sec}$ increase over wild-type (Fig. 8G). IFT27[S79L]::GFP trains also exhibited slightly increased

retrograde speeds (Fig. 8H). Thus, the nucleotide state of IFT27 may regulate the speed and processivity of IFT trains, perhaps by modulating train composition, tuning the ratio of IFT-A-B to IFT-B particles within each train. As the mutant IFT27 proteins were expressed in wild-type backgrounds, stronger effects on IFT speed might have been observed in the absence of wild-type IFT27 protein.

Discussion

IFT particles in *C. reinhardtii* consist of two complexes, IFT-A and IFT-B. In this study, we showed that IFT25 and the small Rab-like G-protein IFT27 form a biochemically separable sub-complex of IFT-B, 25/27. 25/27 readily dissociates from the IFT-B main complex without apparent disruption of the IFT-B main complex, indicating that 25/27 and the IFT-B main complex are relatively independently structured within IFT-B. IFT25 is an obligate binding partner of IFT27 and its main function appears to be protecting IFT27 from aggregation. Two regulatory functions of 25/27 have been presented in this study: stabilizing both IFT-A and the IFT-B main complex from degradation, and regulating the binding interaction between IFT-A and IFT-B. The integration of 25/27 into the IFT-B main complex is not affected by the nucleotide state of IFT27, but the adhesion of IFT-A to IFT-B is controlled by IFT27 acting on an unknown effector within IFT-A. Thus, the nucleotide state of IFT27 regulates the formation of two classes of IFT particles, IFT-A-B and IFT-B, which both serve as building units for IFT train assembly. The stability of IFT-A and the IFT-B main complex are

independent of each other and neither complex affects the stability of 25/27. In contrast, 25/27 stabilizes both IFT-A and the IFT-B main complex, acting upstream in the assembly pathway to modulate the quantity of IFT particles available for flagellar entry. Thus, 25/27 plays a key role in regulating the hierarchical order of IFT particle assembly, controlling both IFT particle abundance and composition (Fig. 9).

Figure Legends

Figure 8. Two classes of IFT particles enter flagella and undergo bi-directional IFT. **(A, B)** Western blots of IFT27 mutant-associated proteins purified from flagellar extracts of transgenic strains expressing IFT27[S79L>::HA::6×His **(A)** and IFT27[S30N>::HA::6×His **(B)** and probed with the antibodies shown. **(C, D, E, F)** Single frames and kymographs from TIRF microscopy video imaging of IFT25::HA::GFP, IFT27::GFP, IFT27[S30N>::GFP, and IFT27[S79L>::GFP strains (Movies S1-S4, ~30 fps). Trains in IFT27[S30N>::GFP experienced the most speed changes and pausing (jerky kymograph lines), while IFT27[S79L>::GFP trains traveled at a more constant velocity. **(G, H)** Distributions of anterograde **(G)** and retrograde **(H)** IFT speeds in the four strains. Anterograde IFT27[S30N>::GFP speed ($2.20 \pm 0.06 \mu\text{m}/\text{sec}$) showed a small significant decrease from IFT27::GFP ($2.29 \pm 0.07 \mu\text{m}/\text{sec}$) ($P = 0.058$), while IFT27[S79L>::GFP ($2.39 \pm 0.06 \mu\text{m}/\text{sec}$) experienced a small significant increase from IFT27::GFP ($P = 0.031$). IFT27[S79L>::GFP retrograde speed ($3.93 \pm 0.17 \mu\text{m}/\text{sec}$) also showed a small speed increase from IFT27::GFP (3.75 ± 0.17

$\mu\text{m}/\text{sec}$) ($P = 0.159$) and IFT27[S30N]::GFP ($3.69 \pm 0.16 \mu\text{m}/\text{sec}$) ($P = 0.051$), while the difference between IFT27::GFP and IFT27[S30N]::GFP retrograde speeds was not statistically significant ($P = 0.610$). Speeds in parenthesis are mean values \pm 95% confidence interval and P -values were calculated from a student's t -test. $N = 2471$ anterograde trains and 2208 retrograde trains from 112 cells (four strains combined). It should be noted that since IFT speeds were measured as the average slopes of traces on the kymographs, the variation in speeds between the strains is most likely a reflection of train processivity and not necessarily the top instantaneous speeds of individual trains.

Figure 9. Hypothetical model of 25/27-regulated IFT particle assembly in *C. reinhardtii*. In the cell body, IFT25 binds the small G-protein IFT27, forming a heterodimer that stabilizes IFT27 from degradation. The association between IFT25 and IFT27 is not mediated by the nucleotide state of IFT27. IFT-B constitutively binds IFT25/27 independent of IFT27 nucleotide state, stabilizing IFT-B from degradation. “?” indicates that the nucleotide state of IFT27 during these steps in IFT particle assembly is potentially variable. When IFT27 is bound to GTP, IFT-A associates with IFT-B, stabilizing IFT-A from degradation. It should be noted that the interaction between IFT-A to IFT-B could also be subject to regulation by other factors including additional small GTPases (Cevik et al., 2010; Li et al., 2010). Two distinct classes of IFT particles, IFT-A-B and IFT-B, bind additional components including the BBSome, the heterodimeric kinesin-2 anterograde motor, and the cytoplasmic dynein-1b retrograde motor. The

mechanisms of these additional interactions remain unknown. The particles then stack together to form IFT trains, which propel themselves into the flagellum and along the axoneme.

Supplementary Videos

Video S1. TIRF imaging of IFT25::HA::GFP movement in flagella of *C.*

reinhardtii. A frame from this movie and kymograph are shown in Figure 8C. Play speed is real-time (30 fps).

Video S2. TIRF imaging of IFT27::GFP movement in flagella of *C. reinhardtii*. A

frame from this movie and kymograph are shown in Figure 8D. Play speed is real-time (30 fps).

Video S3. TIRF imaging of IFT27[S30N]::GFP movement in flagella of *C.*

reinhardtii. A frame from this movie and kymograph are shown in Figure 8E. Play speed is real-time (30 fps).

Video S4. TIRF imaging of IFT27[S79L]::GFP movement in flagella of *C.*

reinhardtii. A frame from this movie and kymograph are shown in Figure 8F. Play speed is real-time (30 fps).

References

Cevik, S., Y. Hori, O.I. Kaplan, K. Kida, T. Toivenon, C. Foley-Fisher, D. Cottell, T. Katada, K. Kontani, and O.E. Blacque. 2010. Joubert syndrome Arl13b functions at ciliary membranes and stabilizes protein transport in *Caenorhabditis elegans*. *J. Cell Biol.* 188:953-69.

Engel BD, Lehtreck KF, Sakai T, Ikebe M, Witman GB, Marshall WF. 2009a. Total internal reflection fluorescence (TIRF) microscopy of *Chlamydomonas* flagella. *Meth. Cell Biol.* 93:157-177.

Engel BD, Ludington WB, Marshall WF. 2009b. Intraflagellar transport particle size scales inversely with flagellar length: revisiting the balance-point length control model. *J. Cell Biol.* 187:81-89.

Lehtreck, K. F., Johnson, E. C., Sakai, T., Ikebe, M., and Witman, G. B. 2009. The *Chlamydomonas* BBSome is transported by a subset of IFT particles and *bbs* mutants abnormally accumulate flagellar signaling proteins. *J. Cell Biol.* 187:1117-1132.

Li, Y., Q. Wei, Y. Zhang, K. Ling, and J. Hu. 2010. The small GTPases ARL-13 and ARL-3 coordinate intraflagellar transport and ciliogenesis. *J. Cell Biol.* 189:1039-51.

Figure A.8

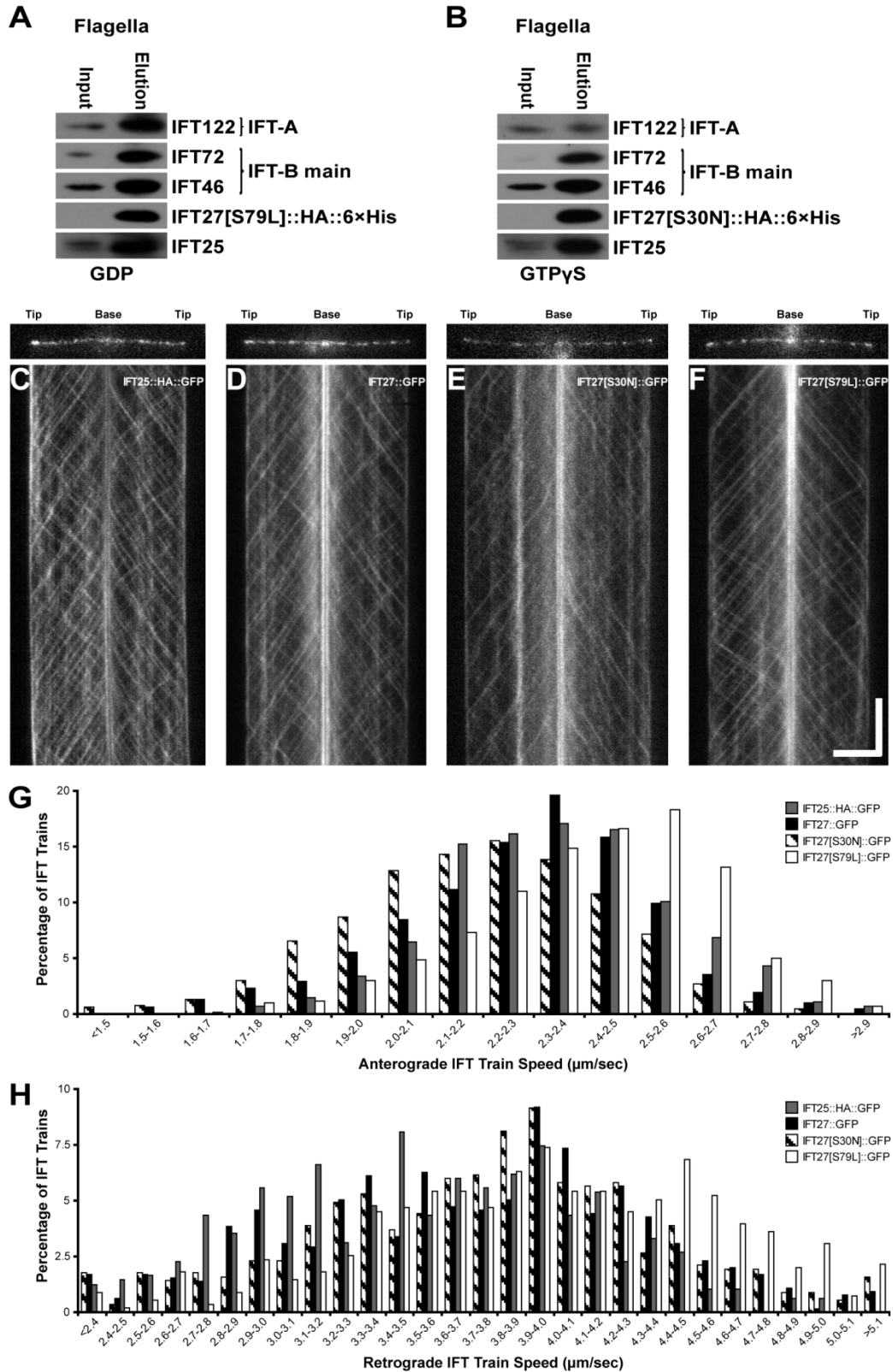
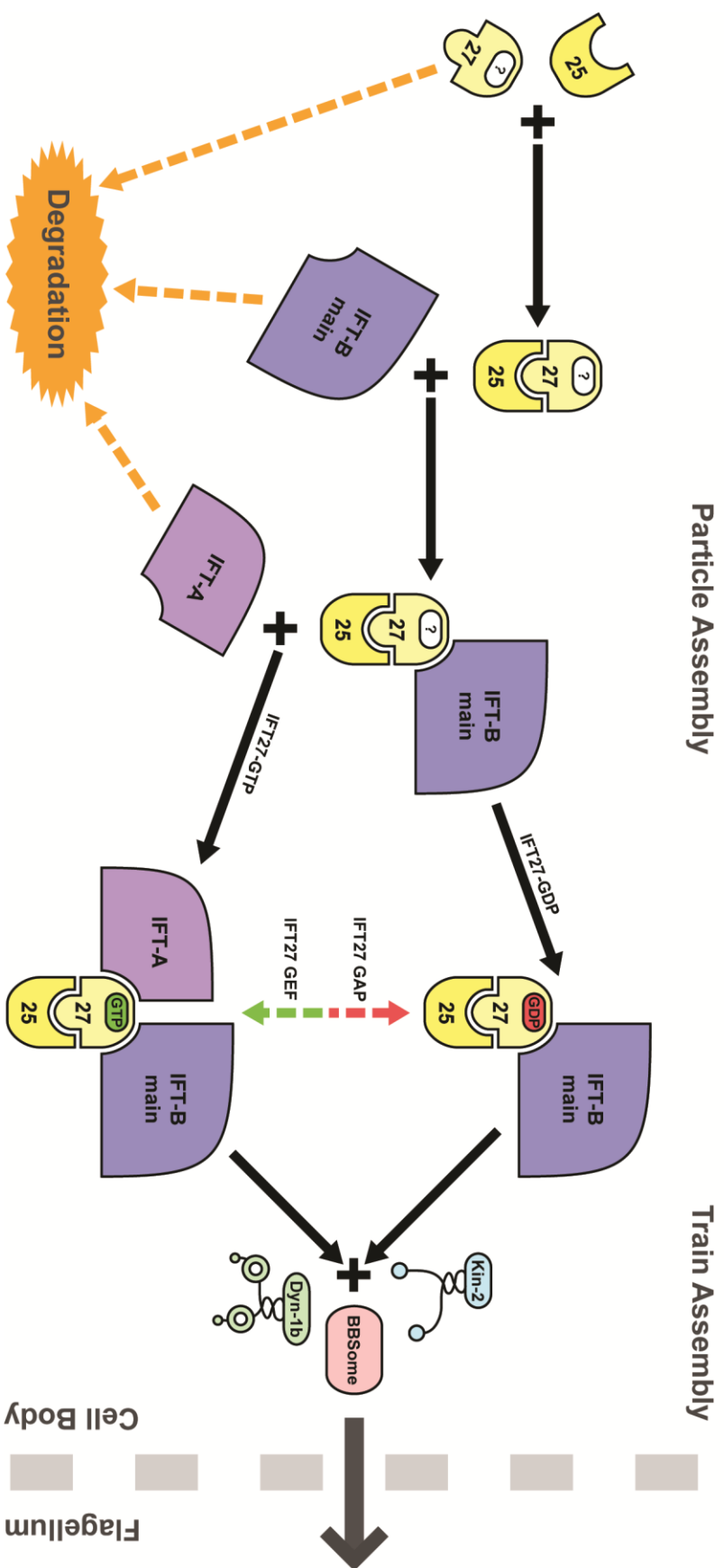



Figure A.9

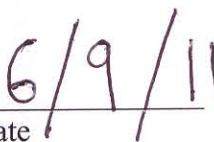


Publishing Agreement

It is the policy of the University to encourage the distribution of all theses and dissertations. Copies of all UCSF theses and dissertations will be routed to the library via the Graduate Division. The library will make all theses and dissertations accessible to the public and will preserve these to the best of their abilities, in perpetuity.

I hereby grant permission to the Graduate Division of the University of California, San Francisco to release copies of my thesis or dissertation to the Campus Library to provide access and preservation, in whole or in part, in perpetuity.


Author Signature


Date